Computational Study on Ion-Bernstein Wave Heating(Dissertation_全文)

AUTHOR(S):

Okada, Hidetoshi

Computational Study on

Ion-Bernstein Wave Heating

Hidetoshi Okada

Kyoto University

1988

Contents

Chapter I

Introduction

In the investigation on thermonuclear fusion, additional heating has been one of the most important problems to achieve the Lawson criterion [1] in the magnetically confined plasmas. In order to heat magnetically confined plasmas, it is a simple way to adopt ohmic heating. The heating efficiency of ohmic heating, however, deteriorates as plasma temperature rises, because the plasma resistivity is proportional to $T_e^{-3/2}$ (T_e:Electron temperature). In addition, energy loss from plasma mainly due to the bremsstrahlung is proportional to $T_e^{\frac{1}{2}}$. An increase of plasma temperature leads to the decline of the efficiency of ohmic heating and an increase of energy loss from plasma. Actually, attainable plasma temperature is predicted to be about 3Kev due to ohmic heating alone under consideration of the limitation of plasma current by the MHD stability criterion. It is difficult to achieve nuclear fusion in magnetically confined plasmas due to ohmic heating alone, therefore, additional heatings should be required.

As methods for supplementary heating, neutral beam injection (NBI) and waves in radio-frequencies (RF) have been adopted. NBI-method has an advantage that the physical process of energy deposition into plasmas is simple; it is collisions between injected neutral particles and charged particles in plasmas. RF-method, on the other hand, has a

merit that oscillators which excite RF waves can be set far from fusion plasmas. This fact might be thought as an advantage of RF-heating from this point of view that oscillators could be protected against high energy neutrons produced from fusion plasmas, and that they could be repaired with ease. Both methods have their own merits and demerits.

With regard to RF-heating, many waves have been adopted as energy carriers; for instance, the electron-cyclotron waves, the lower-hybrid wave, the ion-cyclotron-range of frequency (ICRF) waves, and the Alfven wave, etc. These waves are so-called cold waves whose phase velocities are much faster than the thermal velocities of plasma particles. On the other hand, a new heating scheme called the ion-Bernstein wave (IBW) heating has been proposed by M. Ono [2] which utilizes waveguide to launch fusion plasmas. It might be an advantage of the IBW heating to be able to excite waves into fusion plasmas without antennas or coils which might have complex structures, because such complicated structures set near fusion plasma might produce impurity ions, and they might not be suitable for maintenance. In addition to the above-mentioned technical merits, the ion-Bernstein wave has physical characteristics as follows. Since it has relatively large finite Larmor radius $k_\perp \rho_i$, we can utilize higher cyclotron harmonic frequencies, which means that we can employ considerably smaller waveguides. Moreover, the phase velocity of the ion-Bernstein wave perpendicular to the immersed magnetic field, $\omega/k_\perp$ is generally equal to that of the ion thermal

velocity v_{Ti}. Therefore, ion bulk heating is expected, due to the ion-Bernstein wave, which might be a merit for particle confinement. In the conventional ICRF-heating [3], on the other hand, high-energy tail is produced. It is not easy to confine particles which belong to high-energy tail.

In the scheme of the IBW heating proposed by M. Ono, the ion-Bernstein wave is excited through the mode-transformation process from externally launched electron-plasma wave [2] . In the excitation process, ion-thermal effect plays on important role, as well as in propagation process of the ion-Bernstein wave. Wave energy is carried mainly due to ion-thermal motion, instead of Poynting flux in case of cold waves. The successful excitation and propagation of the ion-Bernstein wave were performed with a toroidal device ACT-1 for the first time [2].

Continuously, heating experiments due to the ion-Bernstein wave was also made with the ACT-1 device [4] , and relatively high heating efficiency was obtained. As a next step of the ion-Bernstein wave heating experiment, the IBW was launched to plasmas composed of D-like and H-like ions whose specific charges were equal to those of D and H with a medium-sized tokamak, the JIPPT-II-U device [5]. In these experiments, it was observed that the ions which had no cyclotron resonance layers in the system were accelerated (We call these ions the non-resonant ions.), and that the heating efficiency did not remarkably depend on the concentrations of the non-resonant ion. In order to explain these phenomena, a complex process through which wave energy was deposited into non-resonant ions was proposed.

According to this hypothesis, the non-resonant ions are heated due to thermal relaxation from the impurity ions which provide their cyclotron resonance layer in the system, and of course, they always existed in the system. However, it is not easy to confirm the above-mentioned hypothesis by means of experimental methods alone, because it is difficult in the experiments in the JIPPT-II-U device to measure all the physical quantities which should be required in order to confirm the hypothesis.

As a supplementary method, particle simulation was employed [6-8], in which almost all the physical quantities were easy to be measured. In particular, it is not difficult in particle simulation to obtain informations on all species of particle in phase-space, which might be necessary to analyze the above-mentioned heating process. The results obtained in the simulation suggested that there was a mechanism of direct energy deposition into the non-resonant ions [6-8]. This heating mechanism was called cyclotron subharmonic resonance [6].

In such processes as both wave propagation in plasmas and acceleration of charged particle, nonlinearity and self-consistency are essential in many cases. In order to analyze these processes, methods utilizing computer have played important roles together with experimental methods as the calculational ability of computer has improved. Among these methods, computer simulation, in particular, has been adopted as a complementary method for experimental and analytic-calculational methods, because this method can naturally include both nonlinearity and self-consistency.

In researches on plasma physics, computer simulation is divided broadly into two categories: magnetohydrodynamic (MHD) simulation and particle simulation. MHD simulation can treat macroscopic phenomena in plasmas whose characteristic length in space is an order of machine size. On the other hand, particle simulation is adopted mainly for microscopic phenomena such as wave-particle interactions. Particle simulation is suitable particularly for analysis in absorption of wave energy into charged particles.

In order to simulate physical process in a torus machine, the following point is essential for wave propagation and absorption. One point is that wave propagates in a torus which is surrounded by grounded conducting walls. Actually, torus is a three-dimensional body in space. However, available computer memory size restricts on the spatial dimensions which can be adopted in the simulation. We, therefore, adopt a two-dimensional slab model, where one axis is perpendicular to the major axis of torus, another is parallel to that axis. In order to simulate phenomena in a slab model of torus, it is necessary to apply the different boundary conditions in each direction. To a direction corresponding to the small radius direction in a torus, it is reasonable to apply the perfectly conducting walls whose electrostatic potentials are forced to be zero. To a direction corresponding to the minor axis of a torus, the periodic boundary condition is suitable. The application of two different boundary conditions to a two dimensional system was proposed by H. Abe [9], and its property was already confirmed. As an another important point to

simulate in a model of torus, there is a difference in spatial length between to the minor axis and to the small radius of tours. It is necessary to adopt a two-dimensional system whose spatial length to one dimension is much longer than that to another dimension. A new method which could treat the above-mentioned system was proposed by H. Abe, *et, al* [10]. In this method, stretched grid, *i.e.* rectangular grid is adopted instead of square grid. This method was applied to the investigation on the lower-hybrid wave heating so as to simulate the behavior of the resonance cone completely [10].

The purpose of this paper is to investigate the excitation, propagation, and plasma heating process due to the ion-Bernstein wave by means of particle simulation. In order to apply the ion-Bernstein wave heating in fusion plasmas, it is practical to adopt the $3\Omega_D$ heating and the $5\Omega_D$ heating in consideration of machine size and perpendicular wavelength of the ion-Bernstein wave to the immersed magnetic field excited in plasmas. These two process, therefore, will be investigated in this paper.

In addition, the electromagnetic effect is essential in the excitation of the ion-Bernstein wave utilizing waveguide, because it is necessary to treat waves radiated from waveguide, into the vacuum. In particle simulation, it was not possible to treat the full Maxwell equations in a two-and-one-half dimensional system because of the restrictions on computer memory and CPU-time. Recently, the improvement in computer ability has released these restrictions, and it has been able to perform simulation

with the full Maxwell equations. In order to treat the propagation and heating process due to the ion-Bernstein wave in a plasma, it is sufficient to adopt the electrostatic simulation, because this wave is essentially electrostatic. To simulate the excitation process utilizing waveguide, it is necessary to adopt electromagnetic code. Recently, the two-and-one-half dimensional electromagnetic code named PS-CODE has been developed by H. Abe, *et al.* [11]. The numerical properties of PS-CODE has been confirmed [11,12], and this code has been applied to the investigation on free-electron laser [13]. We will adopt PS-CODE in the investigation on the excitation and propagation of the waveguide-launched ion-Bernstein wave.

The plan for this paper is as follows. In Chapter II, the property of the ion-Bernstein wave and the excitation through the mode-transformation process proposed by M. Ono are reviewed. In addition, the simulation model used in this paper is explained.

In Chapter III, the cyclotron subharmonic heating process is introduced analytically and computationally. This process plays an important role in the $3\Omega_D$ and $5\Omega_D$ heating process which are discussed in Chapter V and VI.

In Chapter IV, the excitation and propagation of the ion-Bernstein wave are investigated in a single-component-ion-plasma. The computational results are presented, and are compared with the experimental results with the ACT-1 device.

In Chapter V and VI, the computational results on the $3\Omega_D$ heating and the $5\Omega_D$ heating in a two-component-ion-

plasma are presented, respectively. In both chapters, discussion are concentrated on propagation of wave and energy depositions into both ions.

In Chapter VII, excitation and propagation are treated including the electromagnetic effects. Simulations are performed using the electromagnetic code, named PS-CODE.

In Chapter VIII, this thesis is concluded with a summary and discussions.

REFERENCE

[1] J. D. Lawson: Proc. Phys. Soc. (London) B70 6(1957).

[2] M. Ono, K. L. Wong, and G. A. Wurden: Phys. Fluids 26,298(1983).

[3] M. Matsumoto, H. Kimura, k. Odajima, K. Hoshino, S. Kasai, T. Kawakami, H. Kawashima, S. Konoshima, M. Maeno, T. Matoba, T. Matsuda, Y. Miura, H. Nakamura, M. Mori, K. Ohasa, H. Ohtsuka, H. Ogawa, T. Ogawa, S. Sengoku, T. Shoji, T. Sugie, N. Suzuki, H. Takeuchi, Y. Uesugi, T. Yamauchi, S. Yamamoto, and T. Yamamoto: Nuclear Fusion 24,283(1984).

[4] M. Ono, G. A. Wurden, and K. L. Wong: Phys. Rev. Lett. 52,37(1984).

[5] M. Ono, T. Watari, R. Ando, J. Fujita, Y. Hirokura, K. Ida, E. Kako, K. Kawahata, Y. Kawasumi, K. Matsuoka, A. Nishizawa, N. Noda, I. Ogawa, K. Ohkubo, M. Okamoto, K. Sato, S. Tanahashi, Y. Taniguchi, T. Tetsuka, K. Toi, and K. Yamazaki: Phys. Rev. Lett. 54,2339(1985).

[6] H. Abe, H. Okada, R. Itatani, M. Ono, and H. Okuda: Phys. Rev. Lett. 53,1153(1984).

[7] H. Okada, H. Abe, R. Itatani, and M. Ono: Phys. Fluids 23,2417(1986)

[8] H. Okada, H. Abe, R. Itatani, and M. Ono: Plasma Physics. 29,743(1987).

[9] H. Abe, S. Hagihara, and R. Itatani : Proc. of the 9th Conference on Numerical Simulations on Plasmas (Northwestern Univ. Illinois, USA, July, 1980) OD-5.

[10] N. Nakajima, H. Abe, and R. Itatani: Phys. Fluids 25,2234 (1982).

[11] H. Abe and S. Nakajima: J. Phys. Soc. Jpn. 56, (1987).

[12] S. Nakajima and H. Abe: to be published in Phys. Lett. A.

[13] H. Abe, N. Sakairi, S. Nakajima, and R. Itatani: Kakuyugo Kenkyu 53,461 (1985) (in Japanese).

Chapter II

Reviews of the Ion-Bernstein Wave Heating and Simulation Model

2.1 Introduction

In this chapter, we will review the characteristics of the ion-Bernstein wave and the theory of the ion-Bernstein wave heating. In addition, we will explain the simulation model adopted in this thesis briefly.

The dispersion relation of the ion-Bernstein was introduced by I. B. Bernstein in the first place [1]. Employing the full set of Maxwell equations and Vlasov equation, it is shown that there are gaps in the spectrum of allowed frequencies at multiples of the ion-cyclotron frequency for longitudinal ion oscillations. It is natural that these oscillations cannot be introduced without including particle thermal dynamics. Using this dispersion relation, spatial wave damping rate due to cyclotron harmonic resonances will be calculated.

A new supplementary heating method adopting ion-Bernstein wave has been proposed by M. Ono [2]. In this scheme, the ion-Bernstein wave is excited through mode-transformation process in which ion thermal motion plays an important role. We will show the excitation process of the ion-Bernstein wave through mode-transformation, using the dispersion relation derived in this chapter.

In sec. 2.2, we will derive the dispersion relation of the ion-Bernstein wave and calculate the linear wave damping rate due to cyclotron harmonic resonances. In sec 2.3, the mode-

transformation process will be explained. We will present the simulation model in Sec. 2.4.

2.2 The dispersion relation of the ion-Bernstein wave

We will review the derivation of the dispersion relation of the ion-Bernstein wave adopting Vlasov equation and full set of Maxwell equations. In a collisionless plasma, the distribution function for a given kind of particle in the phase-space (r,v) satisfies the Vlasov equation

$$\frac{\partial f_\sigma(\mathbf{r},\mathbf{v},t)}{\partial t}+\mathbf{v}\cdot\nabla f_\sigma(\mathbf{r},\mathbf{v},t)+\frac{e_\sigma}{m_\sigma}(\mathbf{E}+\mathbf{v}\times\mathbf{B})\cdot\frac{\partial f_\sigma(\mathbf{r},\mathbf{v},t)}{\partial \mathbf{v}}=0, \tag{2.1}$$

where σ denotes species of charged particle. The electromagnetic fields are described with the Maxwell equations

$$\nabla\cdot\mathbf{E}=-\frac{\rho}{\varepsilon_0}, \tag{2.2}$$

$$\nabla\cdot\mathbf{B}=0, \tag{2.3}$$

$$\nabla\times\mathbf{E}=-\frac{\partial\mathbf{B}}{\partial t}, \tag{2.4}$$

$$\nabla\times\mathbf{B}=\mu_0\mathbf{J}+\frac{1}{c}\frac{\partial\mathbf{E}}{\partial t}, \tag{2.5}$$

where the charge density ρ and current density **J** are given by

$$\rho(\mathbf{r},t)=\sum_{\sigma} e_{\sigma}\int d\mathbf{v} f_{\sigma}(\mathbf{r},\mathbf{v},t), \tag{2.6}$$

$$\mathbf{J}(\mathbf{r},t)=\sum_{\sigma} e_{\sigma}\int d\mathbf{v} f_{\sigma}(\mathbf{r},\mathbf{v},t)\mathbf{v}. \tag{2.7}$$

The summations are extended over all species of charged particles present.

We consider systems which depart only slightly from thermal equilibrium in a uniform static magnetic field $\mathbf{B}_0$. Then we can write

$$f_{\sigma}(\mathbf{r},\mathbf{v},t)=f_{\sigma 0}(v)+f_{\sigma 1}(\mathbf{r},\mathbf{v},t), \tag{2.8}$$

$$\mathbf{B}(\mathbf{r},t)=\mathbf{B}_0+\mathbf{B}_1(\mathbf{r},t), \tag{2.9}$$

$$\mathbf{E}(\mathbf{r},t)=0+\mathbf{E}_1(\mathbf{r},t), \tag{2.10}$$

where $f_{\sigma 0}$ is the Maxwell distribution

$$f_{\sigma 0}(v)=N\left(\frac{m_{\sigma}}{2\pi T_{\sigma}}\right)\exp\left(-\frac{m_{\sigma}v^2}{2T_{\sigma}}\right), \tag{2.11}$$

N the particle density, T_{σ} temperature in energy units, and the subscript 1 refers to a small perturbation of the associated quantity.

We make a Fourier analysis in space, and take Laplace transform in time.

We can thus obtain the well-known dispersion relation for electromagnetic wave in a hot plasma. The definite form of dispersion relation is expressed in Ref3. Here, we consider a

special case in which electric field can be defined as a gradient of a scalar function Ψ, *i. e*,

$$\mathbf{E}(\mathbf{r},t) = -\nabla\psi(\mathbf{r},t). \tag{2.12}$$

considering the relationship in Eq. (2.12), we can obtain the dispersion relation for electrostatic wave:

$$\sum_{\alpha}\frac{2\omega_{p\sigma}{}^{2}}{k^{2}v_{T\sigma}}\sum_{n=-\infty}^{+\infty}e^{-\lambda_{\sigma}}I_{n}(\lambda_{\sigma})\left\{1+i\sqrt{\pi}Z_{0}W(Z_{\sigma})\right\}=0, \tag{2.13}$$

where $Z_{\sigma}=(\omega-n\Omega_{\sigma})/k_{//}v_{T\sigma}$. In Eq. (2.13), the natations adopted have been conformed to the standard usages. I_n and W denotes modified Bessel function of n-th order and plasma dispersion function, respectively. Z_0 denotes $\omega/(k_{//}v_{T\sigma//})$, and $\omega_{p\sigma}$ demotes plasma frequency of σ-th species.

From the linear dispersion relation given in Eq. (2.13), spatial-wave-damping rate is obtained as

$$Imk_{\perp}=\frac{\pi^{1/2}\ \omega_{pi}{}^{2}n^{2}}{\partial\varepsilon_{xx}/\partial k_{\perp}\omega k_{//}v_{Ti}}\Lambda_{n}(\lambda_{i})\ exp\left[-\left(\frac{\omega-n\Omega_{i}}{k_{//}v_{Ti}}\right)^{2}\right], \tag{2.14}$$

where n denotes cyclotron-harmonic number.

In Eq.(2.14), ε_{xx} is a component of plasma dielectric tensor. From Eq.(2.14), strong wave-damping is predicted when the condition $\omega-n\Omega_i-k_{//}v_{Ti}=0$ is satisfied.

2.3 Ion-Bernstein wave excitation through the mode-transformation process

Ion thermal effects are important in the excitation and propagation of the ion-Bernstein wave. These effects play an essential role in the mode-transformation [2] which permits the electron-plasma wave excited at the plasma surface to transform to the ion-Bernstein wave near the cold lower-hybrid resonance region.

Here, this process is briefly reviewed as made in Ref [2]. The electrostatic linear dispersion relation is [3]

$$\varepsilon(k,\omega)=1+\sum_{\sigma}\frac{k_{\sigma}^2}{k^2}\left\{1+\sum_{n}\frac{\omega}{\omega-n\Omega_{\sigma}}\left[W\left(\frac{\omega-n\Omega_{\sigma}}{k_{//}(T_{\sigma}/m_{\sigma})^{1/2}}\right)-1\right]\Lambda_n(\lambda_{\sigma})\right\}, \tag{2.15}$$

where $k_{\sigma}^2=(n_{\sigma}e^2)/(\varepsilon_0 T_{e//})$, $\lambda_{\sigma}=(k_{\perp}^2 T_{\sigma\perp})/(\Omega_{\sigma}^2 m_{\sigma})$, $\Lambda_n(x)=e^{-x}I_n(x)$, σ indicates the particle species, $W(x)$ is the plasma dispersion function and $I_n(x)$ is the modified Bessel function. The frequency of the externally excited wave is nearly equal to the ion-cyclotron harmonic frequency. Therefore, we approximate Eq. (2.15) for $\omega=O(\Omega_i)$ as [4]

$$k_{\perp}^2\varepsilon_{xx}+k_{//}^2\varepsilon_{zz}=0, \tag{2.16}$$

$$\varepsilon_{xx}=1+\sum_{\sigma}\omega_{p\sigma}^2\frac{e^{-\lambda_{\sigma}}}{\lambda_{\sigma}}\sum_{n=1}^{\infty}\frac{I_n(\lambda_{\sigma})2n^2}{n^2\Omega_{\sigma}^2-\omega^2}, \tag{2.17}$$

$$\varepsilon_{zz}=-\frac{\omega_{pe}^2}{\omega^2}, \tag{2.18}$$

where the electron is assumed to be cold ($\omega/k_{//}\gg v_{T_e}$).

To show the physical outline of mode-transformation process, it is convenient to write Eq. (2.16) as

$$1-\frac{\omega_{pe}^{2}k_{//}^{2}}{\omega^{2}k^{2}}+\frac{\omega_{pi}^{2}exp(-\lambda_{i})}{\lambda_{i}}\sum_{n=m}^{n=\infty}\frac{I_{n}(\lambda_{i})2n^{2}}{n^{2}\Omega_{i}^{2}-\omega^{2}}$$

$$-\frac{\omega_{pi}^{2}exp(-\lambda_{i})2n^{2}}{\lambda_{i}}\sum_{n=1}^{m-1}\frac{I_{n}(\lambda_{i})2n^{2}}{\omega^{2}-n^{2}\Omega_{i}^{2}}=0, \qquad (2.19)$$

where $(m\text{-}1)\Omega_i<\omega<m\Omega_i$, and single-component-ion-plasma has been assumed. In Eq. (2.19), the first two terms express the dispersion relation of the electron-plasma wave, and the 1st two terms. Equation (2.19) shows clearly that the ion-thermal effect plays a dominant role in the mode-transformation process. To occur the mode-transformation process for higher-order finite-ion-Larmor-radius terms are required.

For example, we will explain the mode-transformation process for case of m=2 and m=3, which are correspond to the cases of $3\Omega_D$ and $5\Omega_D$ heating presented in chapters V and VI, respectively.

Equations (2.19) is reduced for $\Omega_i<\omega<2\Omega_i$,

$$ak_{\perp}^{4}+bk_{\perp}^{2}+c=0, \qquad (2.18)$$

$$a=\sum_{i}\frac{3\omega_{pi}^{2}(T_i/m_i)}{(4\Omega_{i}^{2}-\omega^{2})(\omega^{2}-\Omega_{i}^{2})} \qquad (2.21)$$

$$b=1-\sum_{i}\frac{\omega_{pi}^{2}}{(\omega^{2}-\Omega_{i}^{2})}, \qquad (2.22)$$

$$c = -k_{//}^2 \frac{\omega_{pe}^2}{\omega^2}. \tag{2.23}$$

In order to reduce Eqs. (2.19) the modified Bessel function is expanded with its argument λ_i and retained to the first order.

In the region where the plasma density is sufficiently low, *i.e.*, near the antenna position, Eq. (2.20) is the same as the dispersion relation for electron-plasma wave, because the ion thermal motion can be neglected:

$$k_\perp^2 = k_{//}^2 \frac{\omega_{pe}^2}{\omega^2}. \tag{2.24}$$

The excited wave propagates toward the higher-density region and reaches the neighborhood of the cold lower-hybrid resonance layer. Then Eq. (2.20) is approximated as

$$k_\perp^2 = \left(\frac{m_i k_\perp^2 (4\Omega_i^2 - \omega^2)(\omega^2 - \Omega_i^2)}{m_e k_{//}^2 3\omega^2 k_\perp^2 T_i / m_i} \right)^{1/2}. \tag{2.25}$$

From Eq. (2.25), it is found that $k_\perp$ remains finite even near the cold lower-hybrid resonance layer because of the ion thermal effect. This shows that $k_\perp$ does not diverge near the cold lower-hybrid resonance region if λ_i is finite.

The wave propagates as the ion-Bernstein wave beyond the cold lower-hybrid resonance layer to the higher-density region. In this region, Eq. (2.20) is approximated as

$$k_\perp^2 = \sum_i \frac{\omega_{pi}^2}{\omega^2 - \Omega_i^2} \Big/ \sum_i \frac{3\omega_{pi}^2 (T_i / m_i)}{(4\Omega_i^2 - \omega^2)(\omega^2 - \Omega_i^2)}. \tag{2.26}$$

through Eqs. (2.24)-(2.26), we have shown the feasibility of excitation of the ion-Bernstein wave through the mode-transformation process by the ion thermal effects from electron-plasma wave which is excited near the plasma surface. If the ion thermal effects are negligibly small even around the cold lower-hybrid resonance region, the wave dispersion relation is expressed as Eq. (2.24), and the wave cannot propagate beyond the cold lower-hybrid resonance.

Using Eq. (2.26), an important property of the ion-Bernstein wave is shown. For $\Omega_i < \omega < 2\Omega_i$,

$$\lambda_\perp = v_{Ti}\frac{2\pi}{\omega}\left(\frac{3}{4(\Omega_i/\omega)^2-1}\right)^{1/2}. \tag{2.27}$$

This shows that the perpendicular wavelength of ion-Bernstein wave is mainly determined by the local ion temperature and magnitude of the local magnetic field.

For $2\Omega_i<\omega<3\Omega_i$, we expand Eq. (2.15) to an order of $0(\lambda_i^2)$ and obtain

$$dk_\perp^6 + ak_\perp^4 + bk_\perp^2 - c = 0, \tag{2.28}$$

where

$$d = \frac{\omega_{pi}^2(T_i/m_i)^2}{\Omega_i^4}\left[\frac{3}{8}\frac{1}{9\Omega_i^2-\omega^2} + \frac{1}{\omega^2-4\Omega_i^2} - \frac{5}{8(\omega^2-\Omega_i^2)}\right], \tag{2.29}$$

and a, b, and c are given Eqs. (2.21)-(2.23).

As well as the above-mentioned case for $\Omega_i<\omega<2\Omega_i$, we can show the occurrence of mode-transformation. In the low-density region, ion-thermal effect can be negligible and the wave is an electron-plasma wave. Near the cold lower-hybrid resonance region, we can approximate Eq. (2.28) as

$$k_\perp^2=\frac{b}{a}. \tag{2.30}$$

As the wave penetrates further, the effects of cold-electron terms are neglected and we obtain

$$k_\perp^2=\frac{1}{2d}\left[a+(a^2-4bd)^{1/2}\right]. \tag{2.31}$$

Eq. (2.31) is the dispersion relation of ion-Bernstein wave for $2\Omega_i<\omega<3\Omega_i$. One can easily show that it is required $\lambda_i=m-1$ to occur the mode-transformation for $(m-1)\Omega_i<\omega<m\Omega_i$.

2.4 Simulation Model

As shown in Sec. 2.2, the ion-Bernstein wave is essentially an electrostatic wave. Therefore, we have adopted the 2.5D (x,z,v_x,v_y,v_z) electrostatic model in which the simulated system is intended to be representative of the laboratory experiments devices in the most simplified way.

In the electrostatic model, Poisson's equation for electric potential and equation of motion for charged particles are adopted:

$$\left(\frac{\partial^2}{\partial x^2}+\frac{\partial^2}{\partial z^2}\right)\Psi(x.z.t)=-\sum_{\sigma}\frac{e_{\sigma}\delta(\mathbf{r}-\mathbf{r}_{\sigma}(t))}{\varepsilon_0}, \tag{2.32}$$

$$\mathbf{E}(\mathbf{r},\ t)=-\nabla\psi(\mathbf{r},\ t), \tag{2.33}$$

$$m_{\sigma}\frac{d^2\mathbf{r}_{\sigma}(t)}{dt^2}=q_{\sigma}\left[\mathbf{E}(\mathbf{r},t)+\mathbf{v}_{\sigma}(t)\times\mathbf{B}_0(x)\right], \tag{2.34}$$

$$\mathbf{v}_{\sigma}(t)=\frac{d\mathbf{r}_{\sigma}(t)}{dt}, \tag{2.35}$$

where Ψ electrostatic potential, ρ charge density, $\mathbf{E}$ electric field, $\mathbf{B}_0$ external magnetic field, $\mathbf{v}_{\sigma}$ velocity of particle, $\mathbf{r}_{\sigma}$ position of particle, and σ denotes species of charged particle, respectively. In particle simulation, Eqs. (2.32), (2.33), (2.34), and (2.35) are solved with a self-consistent manner. This system is immersed in a z directional static magnetic field $\mathbf{B}_0=B(x)\mathbf{z}$, which is increased with x. The function $B(x)$ is given by

$$B(x)=(x-x_0)^n, \tag{2.36}$$

where $n=1$ or $n=-1$ is used for each run. The density is also slowly increased with x proportionally to $\exp(x/\ell_c)$, where ℓ_c is a characteristic length.

In the x direction, this system is bounded by a pair of the conducting walls where the electrostatic potentials are forced to be zero. In the z direction, the system is assumed to be periodic, so that the wave propagates through it. In the inner

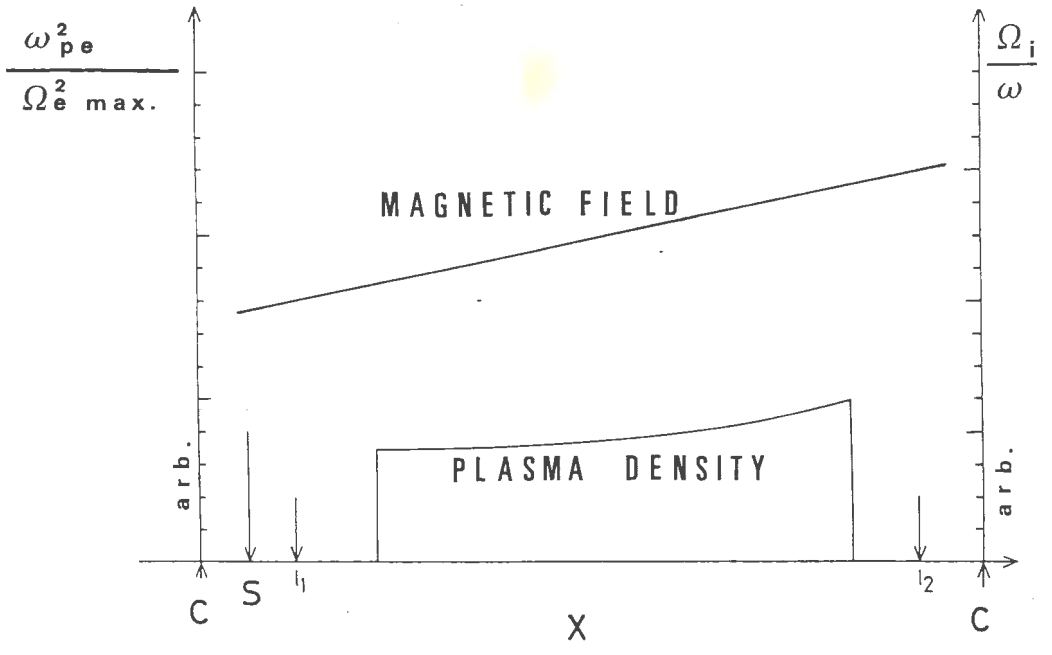

Fig. 2.1. A schematic illustration of the simulation model.The symbols C, S, l_1 and l_2 denote the positions of the conducting wall, the wave source, and limiters, respectively.

side of the conducting walls, a pair of limiters near the conducting walls is assumed to reflect the particle. The particle reaching left wall is reflected into the system with random velocities whose standard deviation is the initial surface temperature, and those reaching right limiters are reflected such that no macroscopic current is generated [5].

Although we treated the complex antenna configurations close to the actual one in Ref. 5, we have returned to the original single mode exciter representing the constant external current used in Ref. 6, in order to study the fundamental physics of the ion-Bernstein wave at first. This antenna is located between the left conducting wall and the left limiter. This situation corresponds to the lower field side excitation in the experiments [7].

Macroscopic quantities such as kinetic energy of the plasma are measured in each of 12 region of equal area, into which the system is divided along the x direction between the limiters. These are averaged both in time and space in each region which is specified by numbering from 1 to 12 beginning from the left, *i.e.*, the antenna side. The velocity distributions are measured in groups of three-successive regions, denoted as region 1-3, 4-6, 7-9, and 9-12, in order to reduce the fluctuations. In Fig.2.1, the schematic illustration of the system is presented.

In the text and figures, time is normalized by a period of the wave externally externally excited, $T=2\pi/\omega$, where ω is the wave frequency. Distance is scaled by a grid spacing of the x direction.

Although the square grids have been used for calculating the self-consistent electric field and the forces acting on the particle in the usual particle model, in this case it is desirable to use the stretched grids in the z direction. The reason is that the ion-Bernstein wave has a much longer parallel wavelength compared with perpendicular wave length, as shown in Sec. 2.3. Similar attempts have been made in Ref. 5, where the lower-hybrid wave propagation, heating, and current generation are treated and the whole resonance cone from the antenna to the lower-hybrid layer is for the first time succeeded to shown by particle simulation.

Because we have chosen the perpendicular grid spacing $\triangle_x$ as approximately one Debye length λ_D, we encounter the situation of the parallel grid size $\triangle_z \gg \lambda_D$. When we use linear (first-order spline) spatial interpolation, we have trouble of grown of numerical instability. In the previous work, we suppressed this numerical instability by using the quadratic (second-order spline) spatial interpolation. When the second-order spline is used, the stretching rate $\triangle_z/\triangle_x$ may be limited to about 10. In the case of the ion-Bernstein wave, the larger ratio was often required. Therefore, we have improved the particle model by using the fourth-order spline spatial interpolation. Their details is published in Ref 8.

REFERENCES

[1] I.B. Bernstein: Phys. Rev. 109, 10(1958).

[2] M. Ono, K. L. Wong, and G. A. Wurden: Phys. Fluids 26,298 (1983).

[3] S. Ichimaru: Basic Principles of Plasma Physics (Benjamin, New York, 1973), pp. 144-145.

[4] T.H. Stix: *Theory of Plasma Waves* (McGraw-Hill, New York, 1962), pp.226.

[5] N. Nakajima, H. Abe, and R. Itatani: Phys. Fluids 25, 2234 (1982).

[6] H. Abe, R. Itatani, and H. Momota: Phys. Fluids 22, 1533 (1979).

[7] M.Ono, T. Watari, R. Ando, J. Fujita, Y. Hirokura, K. Ida, E. Kako, K. Kawahata, Y. Kawasumi, K. Matuoka, A. Nishizawa, N. Noda, I. Ogawa, K. Ohkubo, M. Okamoto, K. Sato, S. Tanahashi, Y. Taniguchi, T. Tetuka, K. Toi, and K. Yamazaki: Phys. Rev.Let. 54, 2339 (1985).

[8] H.Abe, N. Sakairi, R. Itatani, and H. Okuda: J. Computational Phys. 63, 247(1986).

Chapter III

Numerical and Theoretical Study on the Cyclotron Subharmonic Heating

3.1 Introduction

In the ion-Bernstein wave heating process, the cyclotron subharmonic resonance acceleration is one of the most important mechanisms to deposit wave energy into plasmas [1-3]. Through this mechanism, wave energy is directly absorbed into ions which provide their cyclotron subharmonic resonance region in the system. This absorption of wave energy through cyclotron subharmonic heating occurs where wave frequency satisfies the resonance condition $\omega=m/2\Omega_H(m=1,3,5...)$. In the ion-Bernstein wave heating scheme, we encounter such cases as cyclotron subharmonic resonance region is provided in the system: in the $3\Omega_D$ heating presented in chapter V, $3/2\Omega_H$ resonance region is placed in the system. As well as the $3\Omega_D$ heating scheme, $5\Omega_D$ heating shown in chapter VI encounters $5/2\Omega_D$ resonance.

In this chapter, the cyclotron subharmonic resonance process is explained numerically by means of self-consistent and single-particle simulation, and is analytically shown through the multiple-time-expansion method, respectively. Comparing the results obtained in the single-particle simulation with those in the self-consistent simulation, we can find that this process is approximately described by means of a single-particle motion in an external electric and magnetic field. As a rough approximation , it is not required to treat

the process in a self-consistent manner. Considering the simulation results, the equation to describe cyclotron subharmonic heating process was proposed [1]. This equation was subsequently analyzed by means of multiple-time-expansion method [4] .

In Sec. 3.2, we will show simulation results obtained in both self-consistent and single-particle simulation, which suggest the existence of cyclotron subharmonic resonance. In Sec. 3.3, the acceleration process will be treated analytically by means of the multiple-time-expansion method. In Sec. 3.4, we conclude with a discussion.

3.2 Numerical results on the cyclotron subharmonic resonance

In the first place, the numerical results of the self-consistent simulation are shown. Simulation parameters in this run are presented in Table III-I.

Table III-I Simulation parameters

$\lambda_{//}$	512	System length X-direction	256
$q\Psi_{max.} / T_{e,max.}$	3.0	System length Z-direction	512
$(\omega/\Omega_H)_{max.}$	1.9		
$(\omega/\Omega_H)_{min.}$	0.99	$v_{phase} / v_{Te//}$ max.	10.6
		$v_{phase} / v_{Te//}$ min.	5.38
ω_{pe}^2 max. $/\Omega_{e,max.}^2$	0.3		
ω_{pe}^2 min. $/\Omega_{e,max.}^2$	0.1	Number of Electron	179163
m_H / m_e	15	Number of H	179163
$T_{e,max.}$	1.0	Stretching Factor	16
$T_{e,min.}$	0.25		
$T_{H.max.}$	1.0		
$T_{H,min.}$	0.25		

The ion-Bernstein wave is excited by the single mode antenna near the left wall at $\omega=1.9\Omega_H$ in a pure hydrogen(H) plasma which is composed of hydrogens and electrons. The ambient magnetic field increases with x so that the wave encounters $\omega=3/2\Omega_H$ resonance around the center of the system, x=100 (Fig. 3.1). This situation corresponds to the lower-field excitation in a tokamak experiment [5]. In this simulation, however, most of wave energy passes through this region, because the system size employed in the simulation is still not large enough for complete absorption by the present mechanism. We will discuss

this point in detail in Chapter V and VI. Therefore, the fundamental cyclotron damping layer is placed in front of the right wall to absorb the wave energy, thus eliminated the wave reflection, which greatly simplifies the wave physics.

In Fig. 3.1(a), wave potential contours are shown. The corresponding electric field perpendicular to the immersed magnetic field is shown in Fig. 3.1(b). The measured wavenumber ($\mathrm{Re}k_\perp$) in this run is shown as circles in Fig. 3.1(c). In order to compare the results obtained in this with those predicted from linear theory, we calculate the linear dispersion relation Eq. (3.1) (which is the same as Eq. (2.15)) and calculated results shown in Fig. 3.1(c) as a solid line.

$$\varepsilon(k,\omega)=1+\sum_\sigma \frac{k_\sigma^2}{k^2}\left\{1+\sum_n \frac{\omega}{\omega-n\Omega_\sigma}\left[W\left(\frac{\omega-n\Omega_\sigma}{k_{//}\ (T_\sigma/m_\sigma)^{1/2}}\right)-1\right]\Lambda_n(\lambda_\sigma)\right\} . \tag{3.1}$$

The measured values in the simulation are in good agreement with the values calculated from the linear dispersion relation. On the other hand, the values of imaginary part of $k_\perp$ ($\mathrm{Im}\ k_\perp$) are also calculated from the linear dispersion relation and the calculated values are drawn as a broken line in Fig. 3.1(c). The values of $\mathrm{Im}\ k_\perp$ are almost negligible compared with those of $\mathrm{Re}\ k_\perp$ in a whole region except the highest-field side $x>200$. This wave damping predicted here is due to the ion-cyclotron resonance, because the ion-cyclotron region is placed in the highest-field side. In this run, the imaginary parts of $k_\perp$ are approximately estimated from the measured wave amplitudes and are shown in Fig. 3.1(c) as lozenges, indicating

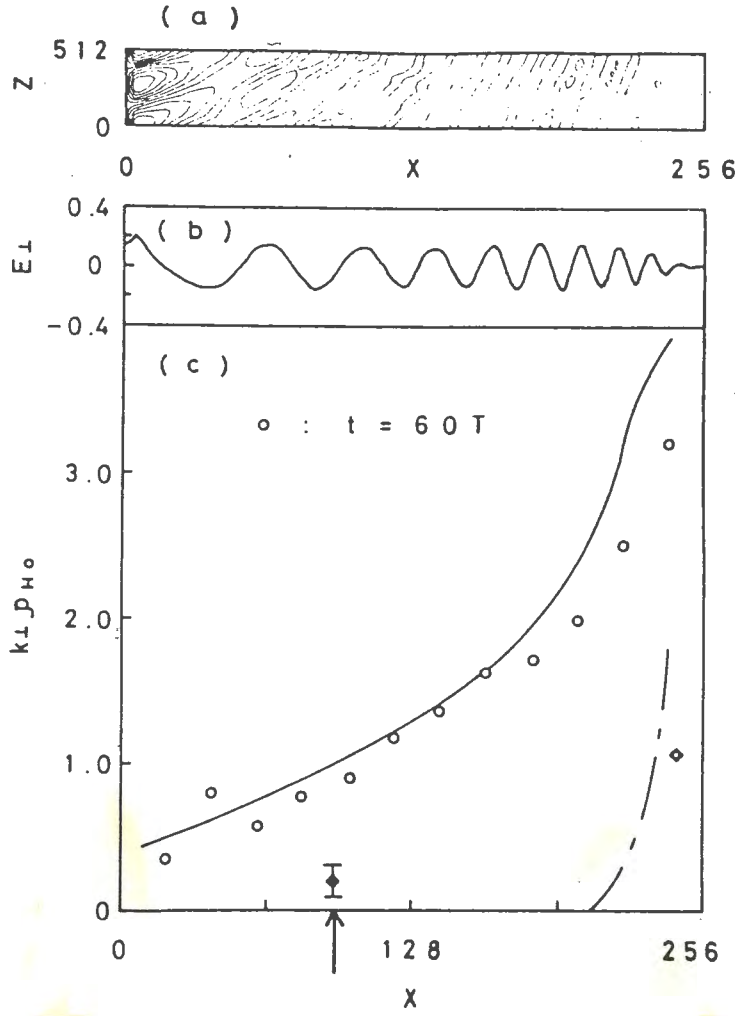

Fig.3.1. The wave propagation profiles: (a) Wave potential contours. Distance in the z direction is scaled down by one sixteenth compared with that in the x direction. (b) $E_\perp$ vs x in steady state at t=60T. (c) $k_\perp$ vs x. The solid line and dashed line are the real and imaginary parts of $k_\perp$ calculated from the linear dispersion relation. The circles and lozenges are the real and imaginary parts of $k_\perp$, obtained from the simulation. The arrow in the figure indicates the position of the cyclotron subharmonic resonance:$\delta\omega_d=\frac{2}{3}\Omega_H-\omega+k_{//}v_z=0$.

a significant absorption region near $\omega=3/2\Omega_H$. The linear theory, of course, predicts no damping here.

In order to observe waves in plasma, we measure the wave spectra of the potential which is Fourier-analyzed with respect to both z (the direction parallel to the immersed magnetic field) and t. In Fig. 3.2, we show the result only for m=1, where m is a mode number in the z direction. The wave energy of higher-modes ($m>1$) are negligibly small compared with that of m=1 mode. This result shows that the excited wave in plasma is monochromatic whose frequency and wavelength parallel to the immersed magnetic field are quite equal to those of wave source. We cannot observe any evidence of occurrence of parametric instabilities.

In Fig. 3.2(a), the spatial energy deposition profile are presented. This results are measured from $t=32T$ to $60T$, during which the wave propagation is in steady state. It is clear that the energy deposition into ion assumes the maximum valve around the position x=100 where $\omega=3/2\Omega_H$.

In order to analyze this heating process in a more simplified system than a self-consistent simulation, the so-called single particle simulation following Ref.6 are performed. In this single particle simulation, the exact equations of motions of many particles (N=5000) are numerically calculated in the presence of a static magnetic field and a monochromatic wave with the fixed wave amplitude α and wavenumber k. In this case, we include ∇B effects in the equation of motion. The adopted equations are

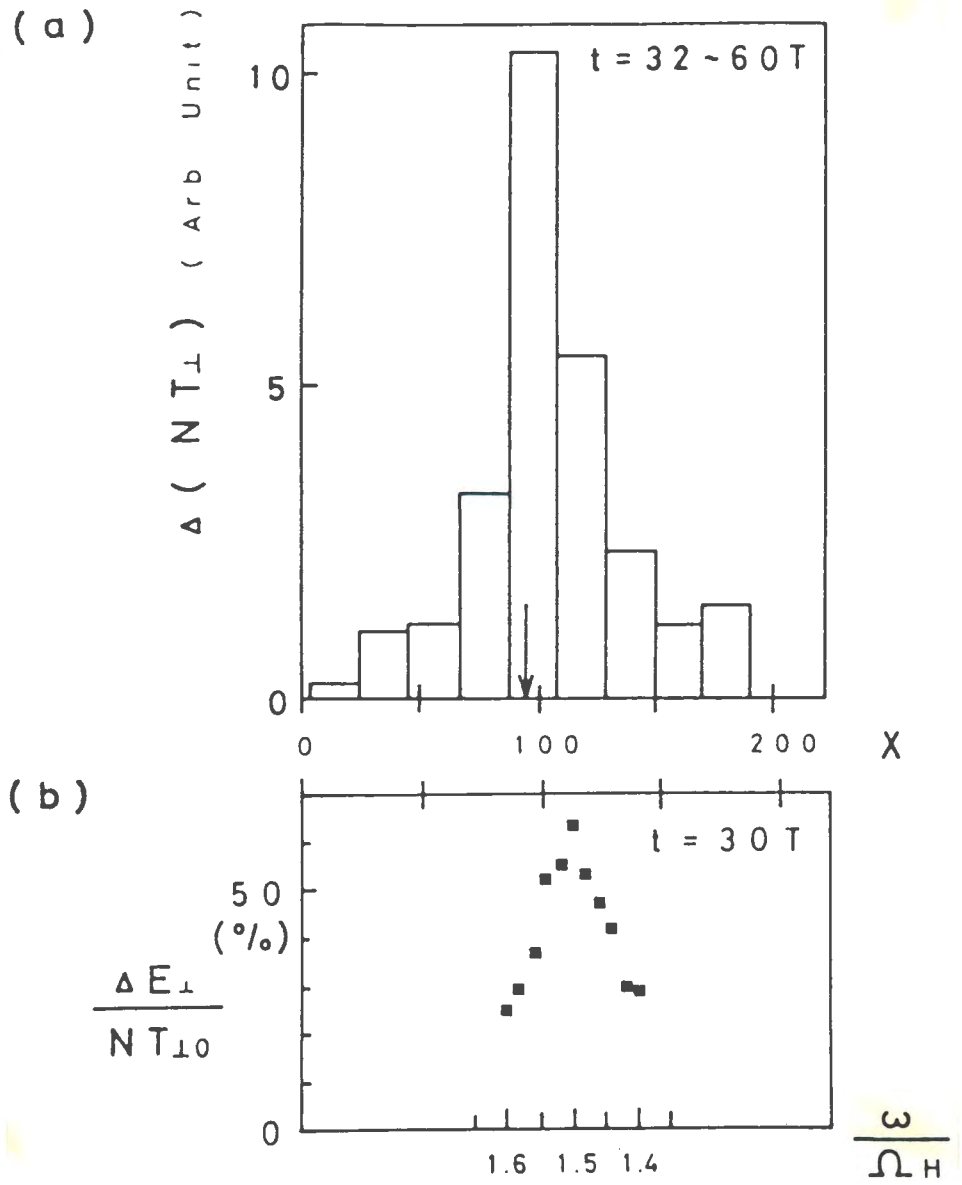

Fig.3.2. The energy increase of ions. The arrow means the same as in Fig.3.1(b). (a) The spatial profiles of the energy deposition to H in the simulation. (b) The energy increment in the single-particle simulation.

$$m\frac{d^2\mathbf{r}}{dt^2} = e(\mathbf{E}(\mathbf{r})+\mathbf{v}\times\mathbf{B}(\mathbf{r})), \tag{3.2}$$

$$\mathbf{B}(\mathbf{r}) = (0,\ 0,\ B_0+\beta x), \tag{3.3}$$

$$\mathbf{E}(\mathbf{r}) = (E_\perp sin(k_\perp x+k_{//}z-\omega t),\ 0,\ 0,) \tag{3.4}$$

where $E_\perp$ and B_0 are constant, and β is set such that ∇B is similar to that in $3/2\Omega_H$ region in the self-consistent simulation. The ∇B effects, however, are found to contribute only several percent enhancement of the energy increment in the situation given in the simulation and may be neglected. We also neglect the acceleration in the z direction and assume $z=v_{z0}t$ (v_{z0}:constant) because we can approximate $k_\perp \gg k_{//}$. A maxwellian velocity distribution is assumed initially.

Simulation parameters are shown in Table. III-II.

Table III-II Simulation parameters

α	0.31
$k_\perp/k_{//}$	15.0
$k_{//}\ v_{Ti0}/\Omega_H$	0.05
ω/Ω_H	1.6-1.4
Number of particle	5000

We adopt the simulation parameter values normalized wave source amplitude α=0.31 ($=ek_{\perp}^2\Psi/m_H\Omega_H^2$), normalized wavenumber perpendicular to the immersed magnetic field $k_{\perp}/k_{//}$=15, and normalized thermal velocity $k_{//}v_{Ti0}/\Omega_H$=0.05, which are the averages of the measurement values at the position of interest in the self-consistent simulation (x=66~128). The wavenumber parallel to the immersed magnetic field $k_{//}$ is constant.

In order to survey the dependence of ion-energy increment on source frequency, the normalized frequency ω/Ω_H is scanned from 1.6 to 1.4 corresponding to the positions from x=86 to 140 in the self-consistent simulation. The perpendicular energy increase per particle $\Delta E_{\perp}/NT_{\perp 0}$ is shown in Fig. 3.2 (b) for comparison. We can see the factor~3 enhancement at ω/Ω_H=1.5 compared with the values at the both sides (ω/Ω_H=1.6 and ω/Ω_H=1.4), which is similar to the results obtained in the self-consistent simulation shown in Fig. 3.2(a).

In Figs.3.3(a) and 3.3(b), the observed perpendicular energy distributions and the single particle simulation, respectively. In both simulations, bulk parts of the distribution is heated. The similarity observed in the velocity distribution functions shows that this mechanism can be described well with a single-particle model.

In Fig. 3.4, the phase space plot in ($v_{\perp}^2$, $v_{//}$) is shown for ω/Ω_H=1.46, which is a typical example. In this phase space plot, the particles with v_z satisfying the resonance condition, $\omega-k_{//}v_z-3/2\Omega_H$=0, is seen to be accelerated

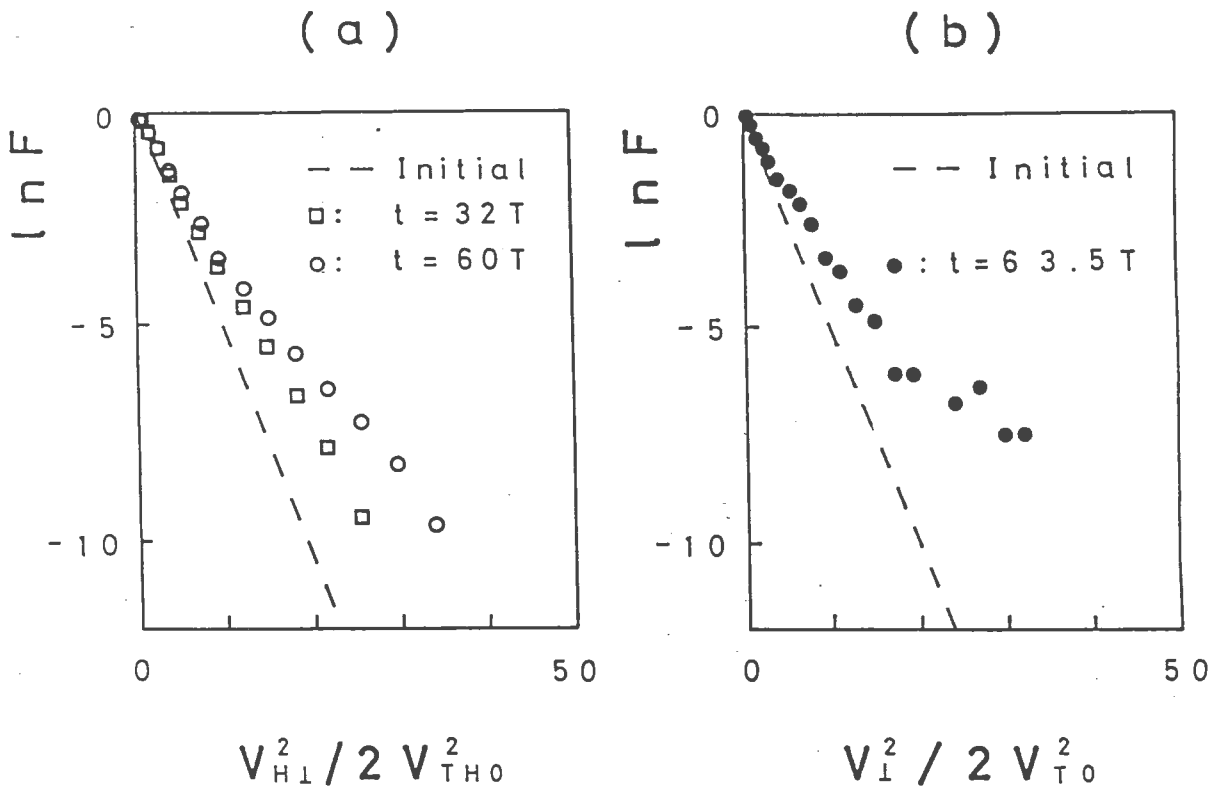

Fig.3.3. The observed velocity distribution functions, ln F vs $v_\perp^2$: (a) for H in the simulation : (b) for the particles in the single-particle simulation.

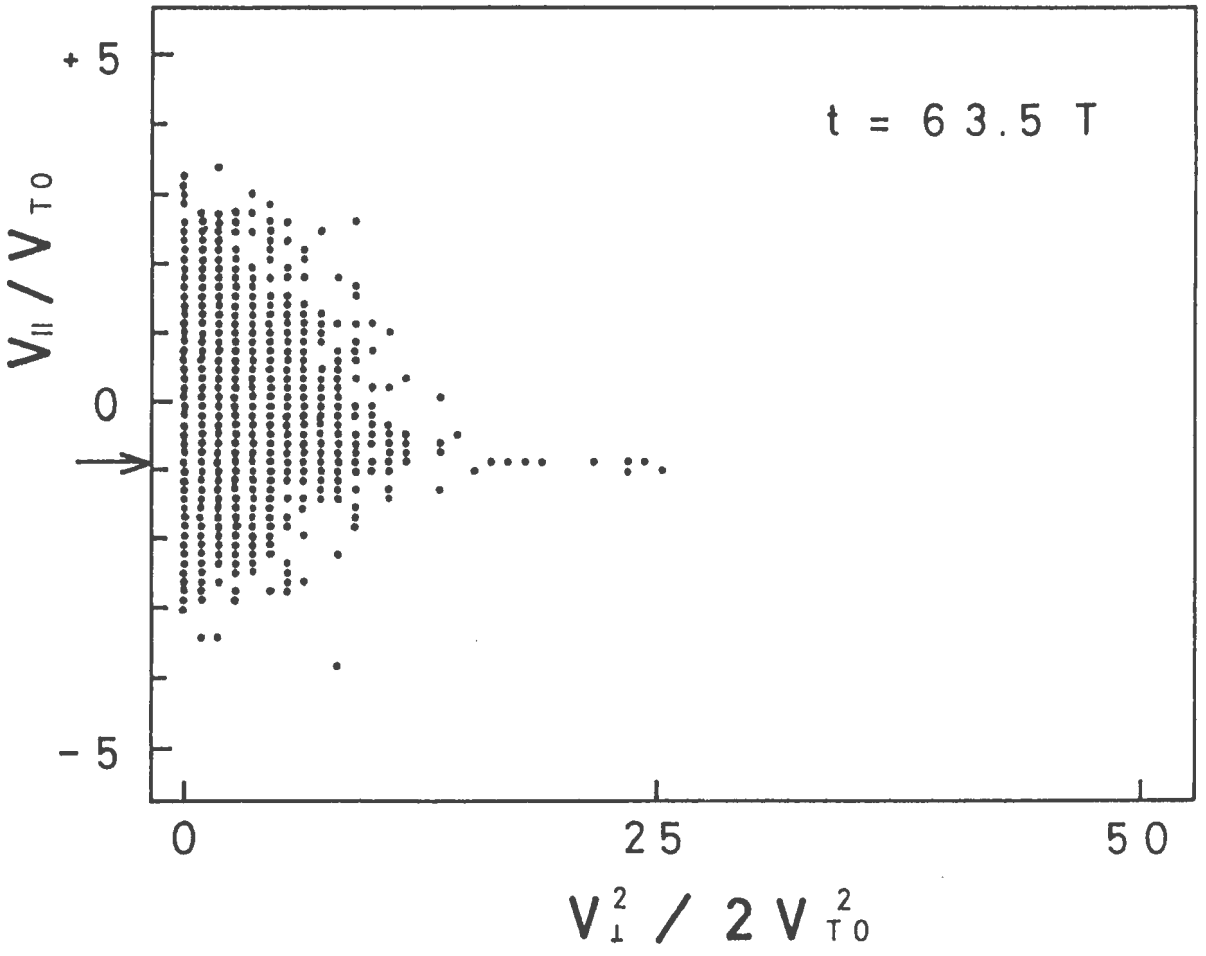

Fig.3.4. the phase-space plot in ($v_\perp^2$, $v_{//}$) in the single-particle simulation(ω/Ω_H=1.46). The arrow indicators $v_{//}$ which satisfies $\delta\omega_d=\omega-k_{//}v_z-3/2\Omega_H=0$. The broken line indicates the boundary of the initial distribution.

selectively. This result clearly shows the evidence of selective acceleration around source frequency $\omega/\Omega_H=3/2$.

3.3 Analytical approach to the cyclotron subharmonic resonance

As is confirmed in the previous section, the cyclotron subharmonic heating process can be approximately described with a equation of motion of a charged particle in an oscillating electric field and a statical magnetic field. In this section, we will analyze the equations of motion by means of multiple-time-expansion which was applied to the cyclotron subharmonic acceleration by R. Sugihara and Y. Ogawa for the first time[4].

The kinetic equation of a charged particle is

$$\frac{d^2}{dt^2}x+x=\varepsilon\alpha\sin(x-\omega t), \tag{3.5}$$

where x,t,ω and ε denote the position of a charged particle, time, the frequency of the electric field, and non-dimensional small parameter. All quantities in Eq. (3.5) are normalized to the wavenumber in length, the cyclotron frequency in time, respectively. α denotes the normalized amplitude of the electric field ($\alpha=ek_\perp E/m_H\Omega_H{}^2$, where e, $k_\perp$, E, m_H and Ω_H denote charge, wavenumber, amplitude of an electric field, mass, and cyclotron frequency, respectively), which is constant both in time and space.

Adopting then method of the multiple-time-scale perturbation, the perturbation analysis is carried out to the order of ε^2 [4].

$$x(t_0, t_1, t_2) = x^{(0)}(t_0 t_1, t_2) + \varepsilon x^{(1)}(t_0, t_1, t_2) + \varepsilon^2 x^{(2)}(t_0 t_1, t_2),$$

$$\frac{d}{dt} = \frac{d}{dt_0} + \varepsilon \frac{d}{dt_1} + \varepsilon^2 \frac{d}{dt_2}. \tag{3.7}$$

The equation in the zeroth order of ε is

$$\frac{d^2}{dt_0^2} x^{(0)} + x^{(0)} = 0. \tag{3.8}$$

The solution of Eq. (3.8) is

$$x^{(0)}(t_0, t_1, t_2) = A(t_1, t_2) \sin(t_0 + \Psi(t_1, t_2))$$

The equation of the first order of ε is

$$\frac{d^2}{dt_0^2} x^{(1)} + x^{(1)} = -2 \frac{d^2}{dt_0 dt_1} x^{(0)} + \alpha \sin(x^{(0)} - \omega t_0) \tag{3.10}$$

Solving the Eq. (3.10), the first order solution of ε, $x^{(1)}$ is obtained. The secular equations are given to eliminate the secular terms in $x^{(1)}$:

$$\frac{dA}{dt_1} = 0, \tag{3.11}$$

$$A\frac{d\Psi}{dt_1}=0. \tag{3.12}$$

We assume that source frequency is not set around cyclotron-harmonic frequency $\omega=l$, (l: integer) when we derive Eqs. (3.11) and (3.12). From the secular equations in the first order of ε Eqs. (3.11) and (3.12), we get

$$A=A(t_2) \tag{3.13}$$

$$\Psi=\Psi(t_2) \tag{3.14}$$

When we assume $\omega=l$, we obtain the secular equations instead of Eqs. (3.11) and (3.12),

$$\frac{dA}{dt_1}=\frac{l}{A}J_l(A)sin(l\phi-\omega t_1), \tag{3.15}$$

$$A\frac{d\Psi}{dt_1}=J_l'(A)cos(l\phi-\omega t_1), \tag{3.16}$$

which were introduced by Timofeev [7]. In Eqs. (3.15) and (3.16), J_1 and J_1' are Bessel function of l-th order and its first-order derivative with respect to its argument A. Equations. (3.15) and (3.16) were adopted in order to analyze stochastic acceleration process by J. Hsu [8].

The solution of the first order of ε without the secular terms is

$$x^{(1)}(t_0,t_1,t_2)=a\sum_l J_l(A(t_2))\times\left\{cosl\psi(t_2)\frac{l-\omega}{(l-w)^2-1}\left[sint_0-\frac{1}{l-\omega}sin(l-\omega)t_0\right]+sinl\psi(t_2)\frac{1}{(l-\omega)^2-1}\right.$$

$$\times\left[2\cos t_0-\cos(l-\omega)t_0\right]\Big\}. \tag{3.17}$$

The equation in the second order of ε is

$$\frac{d^2}{dt_0^2}x^{(2)}+x^{(2)}=-2\frac{d^2}{dt_0dt_1}x^{(1)}-\left(\frac{d^2}{dt_0^2}+2\frac{d^2}{dt_0dt_2}\right)x^{(0)}+\alpha x^{(1)}\cos(x^{(0)}-\omega t_0). \tag{3.18}$$

The secular equations in the second order of ε are

$$\frac{dA}{dt_2}=-\frac{\alpha^2}{4}\sum_l\frac{\sin 2\omega\psi}{(l-\omega)^2-1}J_l(J_{1+2\omega-l}+J_{-1+2\omega-l}), \tag{3.19}$$

$$A\frac{d\psi}{dt_2}=\frac{\alpha^2}{4}\sum_l\frac{J_l}{(l-\omega)^2-1}\left[\cos 2\omega\psi(J_{1+2\omega-l}-J_{-1+2\omega-l})-J_{l+1}+J_{l-1}\right], \tag{3.20}$$

where $J_l=J_l(A)$ is Bessel function of the l-th order. A and Ψ are correspond to finite-Larmor-radius term $k_\perp\rho_H$ and phase, respectively. We have assumed that source frequency ω is equal to $m/2\Omega_H$ ($m=1,3,5\ldots$). When source frequency ω is set out of cyclotron subharmonic resonance (of course, out of cyclotron-harmonic resonance), secular equations in the second order of ε obtained are

$$\frac{dA}{dt_2}=0, \tag{3.21}$$

$$A\frac{d\psi}{dt_2}=-\frac{\alpha^2}{4}\sum_l\frac{J_l}{(l-\omega)^2-1}(J_{l+1}-J_{l-1}). \tag{3.22}$$

Equations. (3.21) and (3.22) show that $A(=k_\perp \rho_H)$ is constant, *i.e.*, particle cannot be accelerated when source frequency is set out of cyclotron subharmonic resonance.

We calculate Eqs. (3.19) and (3.20) for source frequency $\omega=3/2\Omega_H$, and we compare the results obtained with those in the simulation shown in the previous section.

Secular equations for source frequency $\omega=3/2\Omega_H$ are

$$\frac{dA}{dt_2}=-\frac{a^2}{4}\sum_l \frac{sin3\Psi}{(l-1.5)^2-1}J_l(J_{4-l}+J_{2-l}), \tag{3.23}$$

$$A\frac{d\Psi}{dt_2}=\frac{a^2}{4}\sum_l \frac{J_l}{(l-1.5)^2-1}\left[cos3\Psi(J_{4-l}-J_{2-l})-J_{l+1}+J_{l-1}\right], \tag{3.24}$$

where notations adopted are the same as in Eqs. (3.19) and (3.20). We set initial values as $A(0)=1.62$, and $\Psi(0)=0.31$. At $\Omega_H t=65$, we obtain the values $A(=k_\perp \rho_H)=2.37$ and $\Psi=0.26$, which correspond to $v_\perp^2/2v_{T0}^2=25.0$. As shown in Fig.3.4, simulation result shows that charged particles are accelerated to $v_\perp^2/2v_{T0}^2=25.0$. Numerical calculations of Eqs. (3.23) and (3.24) show the same results as obtained in the simulation. In order to investigate the behavior of charged particles described by Eqs. (3.23) and (3.24), we have to pursuit trajectories in the phase space (A,Ψ). Such investigations have been made by R. Sugihara and Y. Ogawa[4]. The results will be published elsewhere[4].

3.4 Conclusion

In this chapter, we have introduced the particle acceleration mechanism due to waves whose frequencies are set around $m/2\Omega_H$ (m=1,3,5,...), by means of self-consistent simulation, single-particle simulation, and analytical approach employing multiple-time-expansion. There different approaches clearly show the evidence of selective acceleration due to waves of $\omega=m/2\Omega_H$ (m=1,3,5,...).

We compared the results obtained by the single-particle simulation with those self-consistent simulation. Based on the comparison, we conclude that cyclotron subharmonic acceleration can be described approximately with a single particle motion in a electromagnetic field. Self-consistency does not play an important role in the acceleration.

In order to solve the equation of motion which can describe the cyclotron subharmonic heating, we adopted multiple-time-expansion which was introduced by R. Sugihara and Y. Ogawa for the first time[4]. We also derived the secular equations for $\omega=3/2\Omega_H$, then we compared the numerical results obtained from the secular equations with those obtained in the single-particle simulation. By means of numerical calculation of the secular equations, we could obtain the same results as in the single-particle simulation . We conclude that the equations introduced by R. Sugihara and Y. Ogawa can describe the cyclotron subharmonic process.

REFERENCES

[1] H. Abe, H. Okada, R. Itatani, M. Ono, and H. Okuda: Phys. Rev. Lett. 53,1153(1984).

[2] H. Okada, H. Abe, R. Itatani, and M. Ono: Phys. Fluids 23,2417 (1986).

[3] H. Okada, H. Abe, R. Itatani, and M. Ono: Plasma Physics. 29,743 (1987).

[4] R. Sugihara, and Y. Ogawa: Plasma Phys. in press.

[5] M. Ono, T. Watari, R. Ando, J. Fujita, Y. Hirokura, K. Ida, E. Kako, K. Kawahata, Y Kawasumi, K. Matsuoka, A. Nishizawa, N. Noda, I. Ogawa, K. Ohkubo, M. Okamoto, K. Sato, S. Tanahashi, Y. Taniguchi, T. Tetsuka, K. Toi, and K. Yamazaki: Phys Rev. Lett. 54,2339(1985).

[6] H. Abe, H. Momota, R. Itatani, and A. Fukuyama : Phys. Fluids 23,2417(1980).

[7] A. V. Timofeev: Nucl. Fusion 14,165 (1974).

[8] J. Hsu: Phys. Fluids 25,159 (1982).

Chapter IV

Computational Study on the Excitation and Propagation of the Ion-Bernstein Wave

4.1 Introduction

In order to investigate the excitation and propagation of the ion-Bernstein wave, we have performed three runs, denoted by A, B, and C. [1]. As a first step of the investigation on the ion-Bernstein wave heating, waves will be launched into a single-component-ion plasmas in every run. We will show the essential difference between these runs in each subsection. In run A, we will identify the mode-transformation process [2] by comparing the results calculated using the linear theory with the particle simulation results. In run B, we will investigate the effects of particle collision on the propagation of the ion-Bernstein wave. In run C where the ion-Bernstein wave fails to be excited, we will discuss the problems concerning the excitation of the ion-Bernstein wave.

The simulation parameters of these runs are presented in Table IV-I. The initial plasma density is taken to be uniform in the z direction and to be increased exponentially in the x direction. The initial temperature distributions for the ion and electron are Maxwellian, isotropic and uniform in both directions. The immersed static magnetic field changes, as given by Eq. (2.34) with $n=-1$.

Table IV-I Simulation parameters

Run name	run A	run B	run C
$\lambda_{//}$	256	512	512
$q\ \Psi_{max.}/T_{e,\ max.}$	0.5	0.5	3.0
$(\omega/\Omega_H)_{max.}$ $(\omega/\Omega_H)_{min.}$	1.69 1.125	1.65 0.99	1.375 1.1
$\omega_{pe}{}^2{}_{max.}/\Omega_{e,}{}^2{}_{max.}$	0.1	1.0	0.15
$\omega_{pe}{}^2{}_{min.}/\Omega_{e,}{}^2{}_{max.}$	0.069	0.05	0.1
m_H/m_e	10	10	10
m_D/m_e			
$T_{e,\ max.}$ $T_{e,\ min.}$	1.0 1.0	1.0 1.0	1.0 1.0
$T_{H,\ max.}$ $T_{H,\ min.}$	1.0 1.0	1.0 1.0	1.0 1.0
System length X-direction	512	512	128
System length Z-direction	256	512	512
$(v_{phase}/v_{Te,//})_{max.}$ $(v_{phase}/v_{Te,//})_{min.}$	5.5 5.5	8.07 8.07	9.0 9.0
Number of Electron	205275	83950	85068
Number of H	205275	83950	85068
Streching Factor	8	16	16

4.2 Excitation and propagation(run A)

The interferograms between the observed potential and the source signal are shown in Fig. 4.1(a) and (b). At $t=6T$, the wave is excited near the plasma surface. At $t=18T$, the wavefront reaches the neighborhood of the cold lower-hybrid resonance, and after $t=18T$, the wave is observed to penetrate into higher-field side beyond the cold lower-hybrid resonance whose position is indicated with the dotted line in Fig. 4.1(a). Figure 4.1(a) shows the evidence of the excitation of the wave beyond the cold lower-hybrid resonance region.

In Sec. 2.3, the excitation of the ion-Bernstein wave through the mode-transformation process from the electron-plasma wave is predicted from the reduced linear dispersion relation, Eq.(2.18). In Eq. (2.18), the Bessel function is Taylor expanded with its argument, $\lambda_i=k_\perp^2 T_i/m_i\Omega_i^2$, and only the first-order terms of λ_i are retained;therefore, Eq.(2.18) is valid only when $\lambda_i \ll 1$.

We numerically confirm this process using the exact linear dispersion relation, Eq.(2.15), including the higher-order terms of λ_i . The calculated perpendicular wavenumber $k_\perp$ are shown in Fig. 4.1(c). For comparison, Eq.(2.24) for the electron-plasma wave, and Eq.(2.26) for the approximated ion-Bernstein wave are calculated and their numerical results are shown in this figure.

In Fig. 4.1(c), we show <u>three lines</u> indicating the values of the real part of $k_\perp/k_{//}$(Re $k_\perp/k_{//}$) calculated from Eqs.(2.15), (2.24), and (2.26). The line that encounters the divergence near the cold lower-hybrid resonance〔Eq.(2.24)〕indicates the

Fig. 4.1. The simulational and the calculated results in run A. (a) The x dependent interferograms of the potential in run A. The symbol LHR denotes the position of the cold lower-hybrid resonance. (b) Wave potential contour. Distance in the z direction is scaled down by one sixteenth compared with that to the x direction. (c) $k_\perp$ vs x. The solid line and dashed line are the real and imaginary part of $k_\perp$ calculated from the linear dispersion relation. The squares and circles are the real part of $k_\perp$ obtained from the simulation at $t=22T$, and $58T$, respectively. The symbol LHR means the same as in Fig. 4-1 (a).

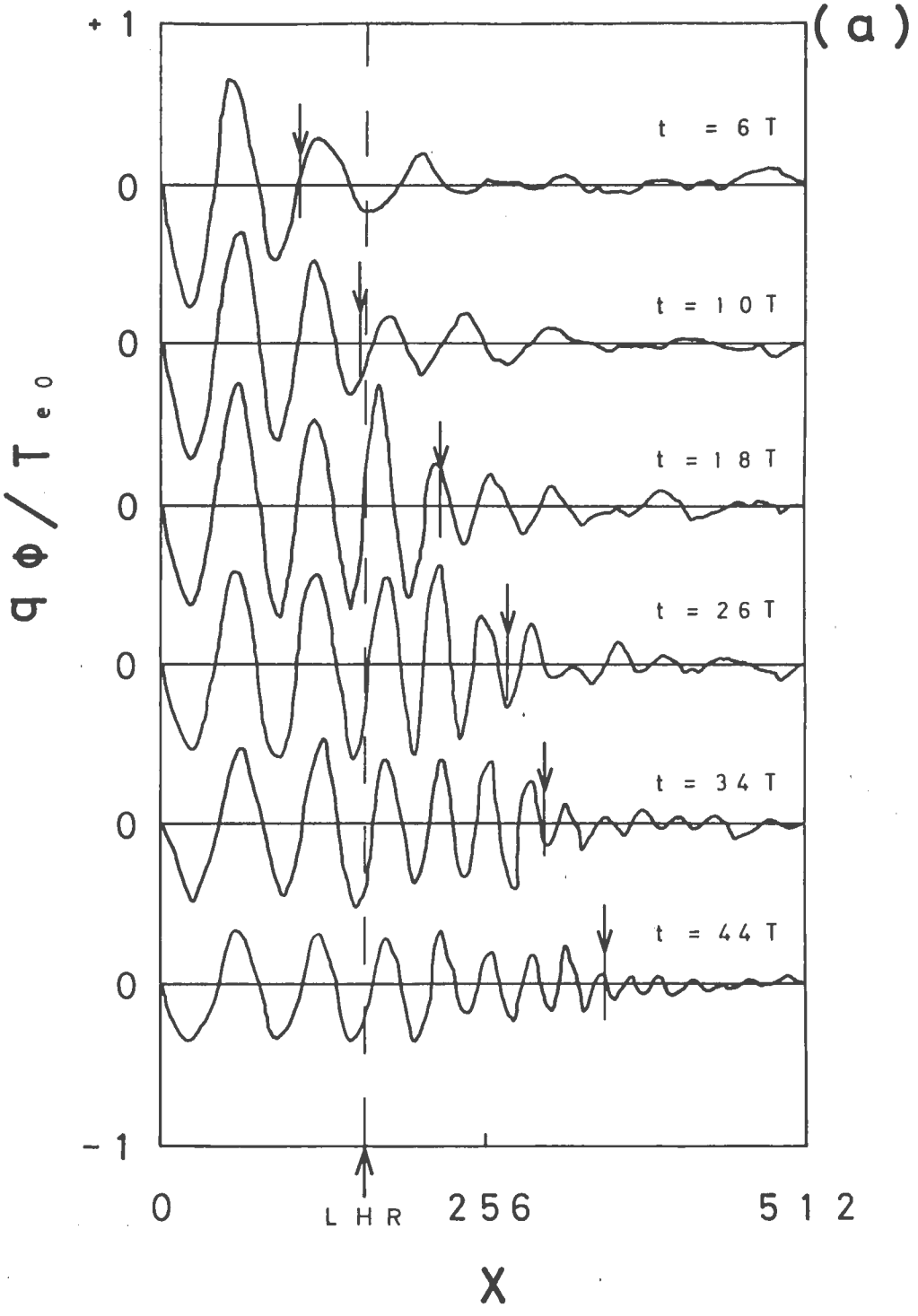
(a)
+1
0
0
0
0
0
0
-1
t = 6 T
t = 10 T
t = 18 T
t = 26 T
t = 34 T
t = 44 T
qφ / T e 0
0
LHR
256
512
X

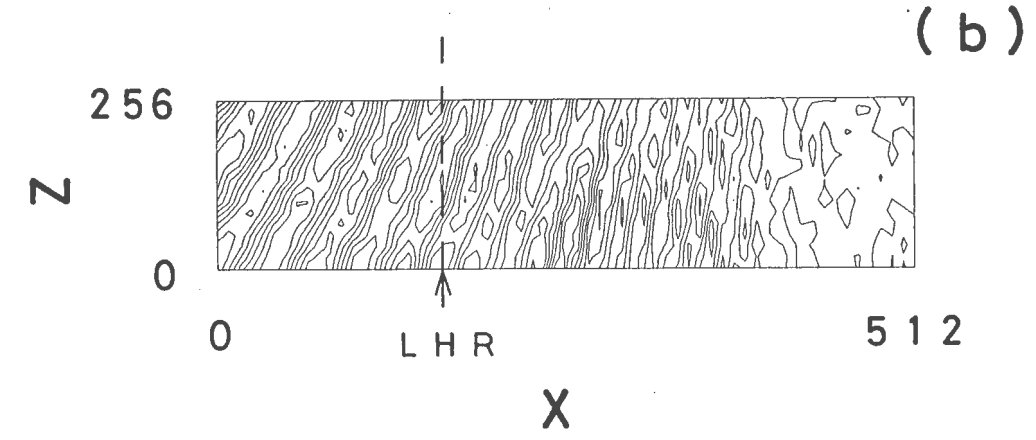
(b)
256
Z
0
0
LHR
512
X

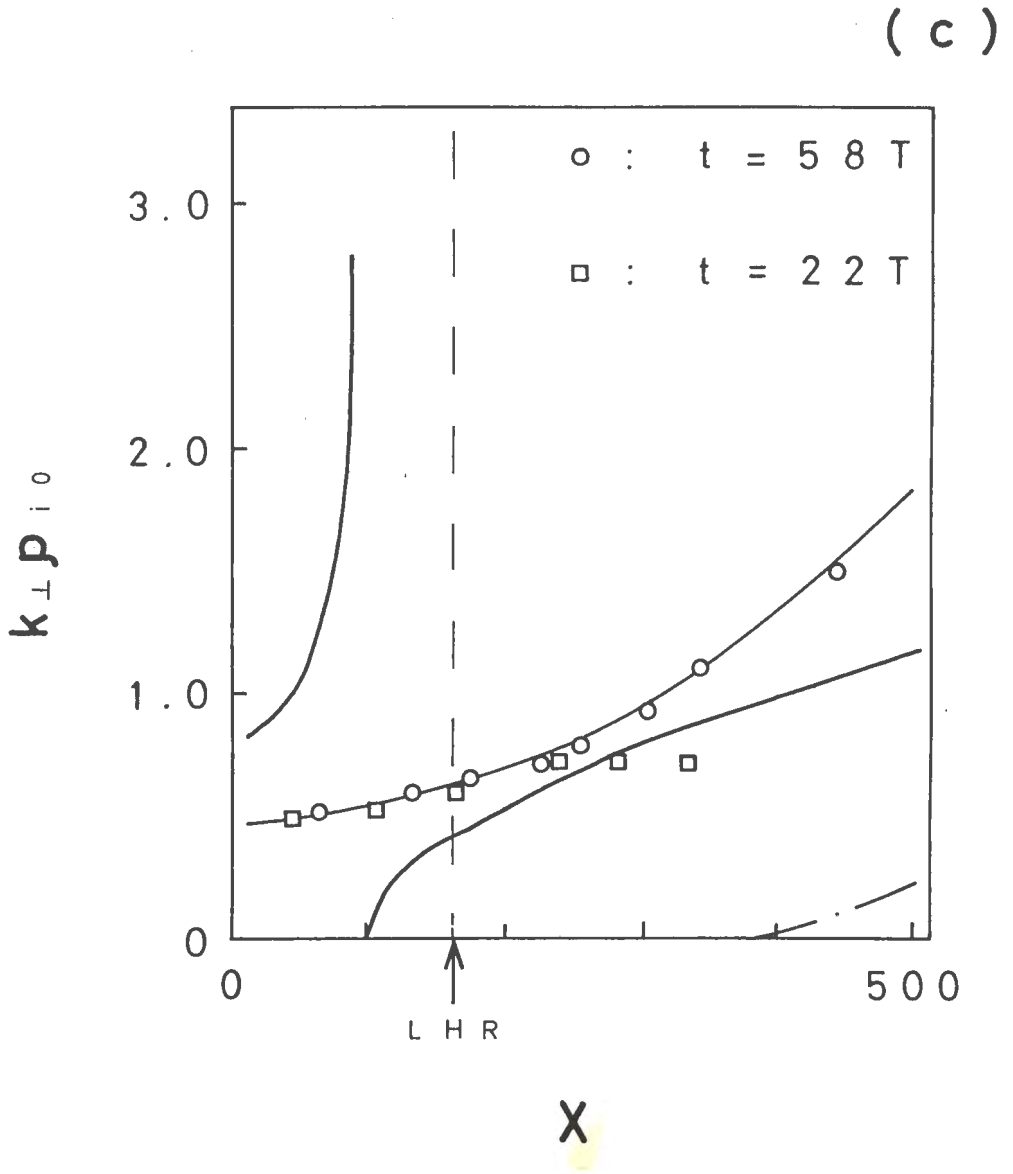
(c)
o : t = 58 T
□ : t = 22 T
3.0
2.0
1.0
0
$k_\perp \rho_{io}$
0
LHR
500
X

dispersion relation of the electron-plasma wave. The line arising near the position x=100〔Eq.(2.26)〕indicates the dispersion relation of the approximated ion-Bernstein wave. The other solid and dotted lines indicate the real and imaginary parts of $k_\perp/k_{//}$ calculated from Eq.(2.15).

As seen in Fig. 4.1(c), there is a difference between the values of $k_\perp/k_{//}$ calculated from Eqs.(2.15) and (2.24). Near the cold lower-hybrid resonance region, the electron-plasma wave encounters the cold resonance and cannot propagate beyond the resonance region. The values of Re $k_\perp/k_{//}$ obtained from Eq.(2.15) do not diverge near the cold resonance region(x=160) because of the ion thermal effects, which is indicated in Eq. (2.25). Near the region x=160 to the higher-field side, the values of $k_\perp$ obtained from Eq.(2.26) become close to those from Eq. (2.25). Near the region x=500, a difference is seen between the results calculated from Eq.(2.15) and Eq.(2.26).

This difference originates from neglect of the higher-order terms of λ_i in Eq.(2.26). Therefore, this approximation is not accurate for the region where the value of λ_i is large. This is accurate only for the region where λ_i is moderate.

From the calculation of Eq.(2.15), the spatial wave damping rate becomes finite in the region x = 400. In run A, the values of $(\omega-\Omega_i)/k_{//}v_{Ti}$ near the highest field side x=500 is approximately 1.4. Therefore, the finiteness of the spatial wave damping rate is attributed to the fundamental ion-cyclotron resonance located near the outside of the right wall.

Corresponding to the numerical calculation results, the perpendicular wavenumbers are measured at t=22T and 58T, and are

shown in Fig. 4.1(c). The wavenumbers obtained from the simulation at t=22T agree with those from numerical results in the region x⟨230. At t=58T, the measured wavenumbers are in good agreement with those from calculated results in the whole region. This means that the wavefront propagates toward the higher-field side with time.

In order to evaluate the velocity of the wave front, the group velocity of wave, $v_{g\perp}$, is calculated from Eq.(2.15);

$$\frac{\partial\varepsilon(k,\omega)}{\partial\omega}+\frac{1}{v_{g\perp}}\frac{\partial\varepsilon(k,\omega)}{\partial k_{\perp}}=0 \tag{4.1}$$

Using this $v_{g\perp}$, the position where the wavefront reaches at time t is calculated as

$$t=\int_0^x\frac{dx}{v_{g\perp}}, \tag{4.2}$$

and the positions predicted from the calculation are shown in Fig. 4.1 (a) by arrows. At t=6T and 10T, the positions predicted from the numerical calculation do not quite agree with those of the wavefront seen in the simulation. After t=18T, the numerically predicted values gradually approach the observed positions of the wavefront in the simulation.

4.3 Collisional effects on the propagation of the ion-Bernstein wave (run B)

As shown in Fig. 4.2, the damping of the wave is observed at the steady state of $t=80T$ in the region $x=100$-300, where the ion-Bernstein wave is excited.

As an origin of the wave damping, the possibility of the nonlinear effects which are usually examined may be excluded. We will show this as follows. The wave trapping of the electrons does not occur because the phase velocity of the wave is much faster than the electron thermal velocity ($v_{\mathrm{phase}//}/v_{Te//}=8.07$) and the amplitude of the wave source is not large enough to trap the electrons ($q\phi/T_e=0.5$). Actually, the electrons trapped by the wave are not observed in the measurements of the electron velocity distribution. As confirmed in the wave spectra, the parametric instabilities do not occur. The effect of the cyclotron subharmonic resonance [3] is not important because the value of ω/Ω_i is changes from 1.45 to 1.2 in the region $100 \leqq x \leqq 300$ and the amplitude of the observed potential in this region is not large ($\alpha=k_\perp^2 q\phi/m_i\Omega_i^2=0.1$).

The linear ion-cyclotron damping does not occur because the cyclotron resonant velocity is much faster than the ion thermal velocity in this region ($v_{\mathrm{resonance}}/v_{Ti}=(\omega-\Omega_i)/k_{//}v_{Ti}=8.0-4.0$). The magnitude of the imaginary part of $k_\perp$ is also much smaller than that of the real part from the calculation of the linear dispersion relation ($\mathrm{Im}k_\perp/\mathrm{Re}k_\perp<10^{-3}$). Therefore, only the collisional wave damping remains as an origin of this wave damping.

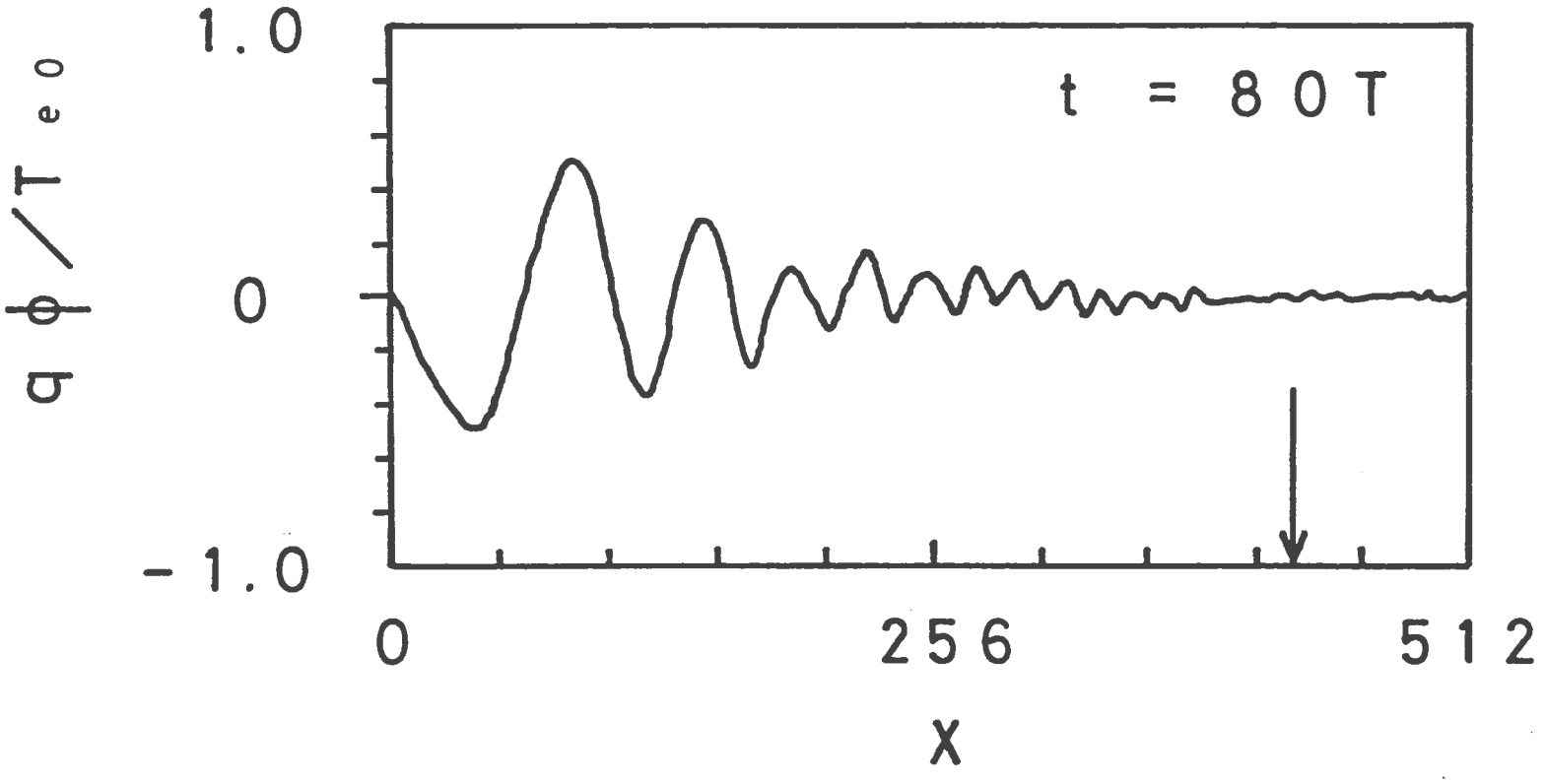

Fig. 4.2. The dependent interferograms of the potential in run B. The arrow located near the right side indicates the position of the cyclotron resonance: $\omega - k_{//} v_{Ti} - \Omega_i = 0$.

The collision frequency ν is evaluated as

$$\upsilon \propto \frac{ne^4}{v_t^3}, \tag{4.3}$$

where n is the plasma density, e is the charge of a particle, and v_t is the thermal velocity of particles. Using Eq.(4.3), the collision frequency in run B is compared with that in run A.

$$\frac{\upsilon_{\text{runB}}}{\upsilon_{\text{runA}}} = 3.5\times10^3 . \tag{4.4}$$

Through the estimation in Eq.(4.4), it is thought that the observed spatial damping of the wave is caused by the collision. To consider the collisional effects further, we have estimated the spatial wave damping rate, Im $k_\perp/k_{//}$, and obtained the value of Im $k_\perp/k_{//}$=0.73−1.43 around x=200 from the measured potential wave amplitude, where Im $k_\perp/k_{//}$ denotes the imaginary part of $k_\perp/k_{//}$.

On the other hand, we can estimate the spatial wave damping rate in the collisional plasma using the linear dispersion relation, Eq.(2.15). We set $\omega=\omega_r-i\upsilon_e$ for electrons and $\omega=\omega_r-i\upsilon_i$ for ions in Eq.(2.15) to include the effect of collisions, where ω_r is the real part of ω; the collision frequencies ν_e and ν_i indicate the inverses of the slowing−down times of electrons and ions, respectively. The magnitude of ν_e or ν_i is proportional to each density, $\nu_i=(m_e/m_i)^{1/2}\nu_e$ is assumed. Including the finite ν_i and ν_e, we calculate Eq. (2.33) to obtain Im $k_\perp/k_{//}$ and compare these values with those obtained from the

simulation. The collisional frequency at the position x=200 in run B is estimated as $\nu_c/\omega=1.7\times10^{-2}$.

From the calculation of Eq.(2.33) with varying the values of ν_e and ν_i, the wave damping rate is determined mainly by ν_i in the region where the ion-Bernstein wave is excited. If we set $\nu_e/\omega=5.4\times10^{-2}$ and $\nu_i/\omega=1.7\times10^{-2}$, Im $k_\perp/k_{//}$ is nearly equal to 1.1. If ν_e/ω is set to zero and ν_i/ω remains 1.7×10^{-2}, Im $k_\perp/k_{//}$ is still 1.1, which means strong damping. However, if ν_e/ω is set 5.4×10^{-2} and ν_i/ω is set to zero, Im $k_\perp/k_{//}$ is 3.3×10^{-2}, which means little damping. Therefore, the ion collisional damping on the IBW dominates over that of the electrons, which may not be surprising since the ion-Bernstein wave is mainly supported by the kinetic motion of the ions.

4.4 Failure mode of the ion-Bernstein wave excitation (run C)

In run C, the essential difference in the simulation parameters from those in run A is the value of ω/Ω_i near the antenna position. The change in the system size is not essential. In run A, ω/Ω_i changes from 1.69 to 1.125;however, in run C, this value changes from 1.375 to 1.1. In run C, the cold lower-hybrid resonance region is located out of the system in the left side. The ion Bernstein wave is expected to be excited not only through the mode-transformation process, but

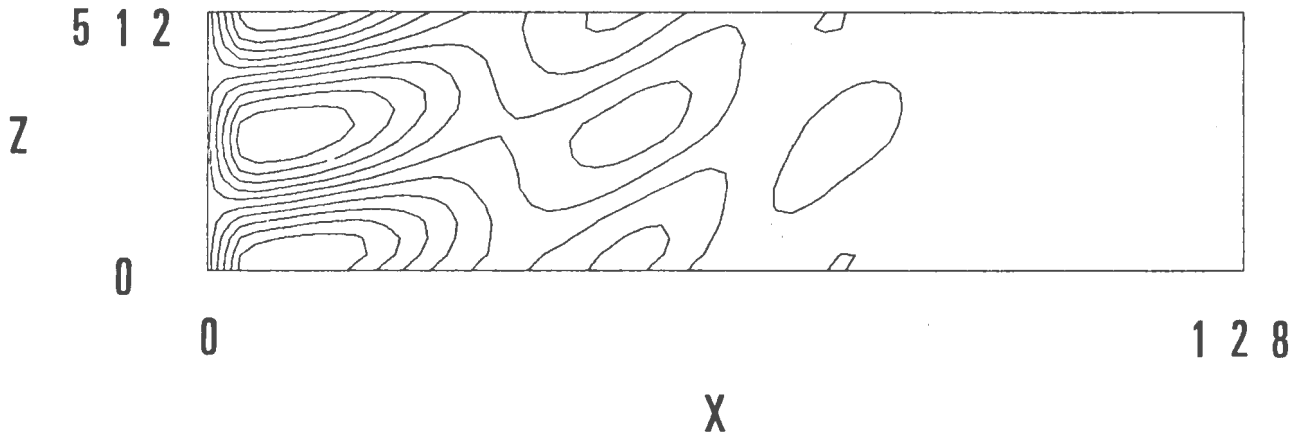

Fig. 4.3. Wave potential contour in run C. Distance in the z direction is scaled down by one sixteenth compared with that to the x direction.

also directly. We call the direct excitation of the ion-Bernstein wave. The successful excitation of the wave is predicted from the calculation of Eq. (2.15) because the value of Im $k_\perp$/Re $k_\perp$ is very small in almost the whole region of the system.

The interferogram in (x,z) space between the measured wave potential and the antenna signal is observed at $t=12T$ and shown in Fig. 4.3. The measured values of $k_\perp$ are far from those predicted from the linear dispersion relation, Eq.(2.15). In particular, the measured values of $k_\perp$ near the plasma surface($5<x<20$) is nearly equal to zero, *i.e.*, close to the value of $k_\perp$ in the vacuum. Run C is an example that the wave is not excited successfully. As a physical quantity which might exert an influence on the wave excitation, we can point out the gradient scale lengths compared to the ion Larmor radius(We call these quantities GSLILR parameters.) which is a characteristic length of the ion-Bernstein wave. As to the GSLILR parameters, there are three kinds of the gradient scale lengths in the system;density, temperature, and strength of the external magnetic field. The values of the GSLILR parameters and the Larmor radius spatially averaged are presented in the Table IV-II.

Table IV-II. The Ion Larmor Radii and the Gradient Scale Lengths Compared to the Ion Larmor Radius (GSLILR Parameters)

Run name	Lamer redius (Δ_x)	Dencity	Temperature	Magnetic feild
run A	4.6	283	uniform	272
run B	5.9	28	uniform	211
run C	5.0	57	uniform	118
run 3	5.5	41	68	95

Among the above-mentioned runs, only run C is the case in which the wave is not excited successfully.

The GSLILR parameters in run C are not much different from those in other runs in which the successful excitation of the wave is observed. In run C, the GSLILR parameter for the temperature is zero because the temperature is set to be uniform initially. This parameter for the density in run C is smaller than in run B. The parameter for the strength of the external magnetic field is as same as that in run 3. Both run B and run 3 are the cases in which the wave excitation is successful.

We measured the increment of the kinetic energy in run C. The increment of electron kinetic energy to the initial value is less than 1%. This is not significant increment. The increment of the ion kinetic energy to the initial value is 30% in the region near the plasma surface. This value in run 3, in which the successful excitation of the wave is observed, is 24% measured at the same time in the same region in run 3. (In run

3, the amplitude of the wave source is as large as that in run C.)We do not think that the changes in the GSLILR parameters affect the energy absorption into plasma.

In order to make it double sure, we tried again run C with the same size in the x direction as run B. We call this new-run C. The GSLILR parameter of the density in new-run C is smaller than that in run B. This value of the strength of the external magnetic field in new-run C is as same as that in run A. These parameters in new-run C are almost as same as those in the cases in which the successful wave excitation is observed. In new-run C, however, the wave excitation is not successful as is observed in old-run C, as is expected.

Table IV-III. The Ion Larmor Radii and the Gradient Scale Lengths Compared to the Ion Larmor Radius (GSLILR Parameters)

Run name	Larmer radius (Δ_x)	Density	Temperature	Magnetic field
run A	4.6	283	uniform	272
run B	5.9	28	uniform	211
old-run C	5.0	57	uniform	118
new-run	5.0	114	uniform	236
run 3	5.0	41	66	95

4.5 Discussion and conclusion

The excitation and propagation of the ion-Bernstein wave in a single-component ion plasma are studied using electrostatic self-consistent particle simulation code. Here, we will summarize the results obtained and indicate the relation between these simulation results and the results of other works, particularly of the experimental works.

With regard to excitation of the ion-Bernstein wave, we do not find any problems through the mode-transformation process from the externally excited electron-plasma wave in the usual experimental conditions, as was already performed in the experiment made with the ACT-1 device [2]. In order to excite the ion-Bernstein wave directly, it is necessary to set the value of ω/Ω_i near the antenna position close to the cutoff of the branch;that is, for excitation of the branch of $\Omega_i < \omega < 2\Omega_i$, ω/Ω_i must be set close to 2 near the antenna position. If ω/Ω_i is set far from 2, (for example, 1.375, as in run C), the ion-Bernstein wave is not excited successfully, as shown in Fig. 4.3. We also find that there are not much difference in the gradient scale lengths compared to the Larmor radius (GSLILR) parameters between in run C and other runs as shown in Table IV-III. The changes of the GSLILR parameters in run C, therefore, do not significantly affect the wave excitation. Without changing the simulation parameters except for the value of ω/Ω_i near the antenna position, the ion-Bernstein wave can be excited successfully as shown in Fig. 4.3. It is thought that what affects the wave excitation is only the value of ω/Ω_i near the plasma surface. The theoretical explanation of the correlation between feasibility of the excitation of the ion-Bernstein wave and the value of ω/Ω_i near the antenna

position has been remained to be solved. However, we have pointed out the condition for the direct excitation of the ion–Bernstein wave.

Concerning the propagation of the ion–Bernstein wave, we have reached the conclusion that the ion–Bernstein wave might be damped by particle collision. From the calculation using the linear dispersion relation, the ions play a main role in this collisional process. The value of ν_i/ω is estimated to be 1.7×10^{-2} from the results in both the simulation and the numerical calculation. However, this collisional effect should not affect wave propagation when the ion–Bernstein wave is applied to fusion plasma heating, because the value of the collisional frequency between ions, ν_{ii}/ω, is calculated to be$\sim10^{-7}$, using typical fusion plasma parameters.

The values of $k_\perp$ obtained in the simulation are in good agreement with those calculated from the linear dispersion relation. The velocity of wavefront is also well predicted from the wave group velocity calculated using the linear dispersion relation. The excited wave is an almost monochromatic one whose frequency and wavelength are the antenna frequency and wavelength, respectively.

REFERENCES

[1] H. Okada, H. Abe, R. Itatani, and M. Ono : Phys. Fluids 29,489 (1986).

[2] M. Ono, K. L. Wong, and G. A. Wurden:Phys. Fluids 26, 298 (1983).

[3] H. Abe, H. Okada, R. Itatani, M. Ono, and H. Okuda : Phys. Rev. Lett. 53, 1153(1984).

Chapter V

Computational Study on the $3\Omega_D$ Heating due to the Ion-Bernstein Wave

5.1 Introduction

In order to investigate the $3\Omega_D$ heating, three runs(runs 1−3)were performed. These simulation parameters are presented in Table V−I [1]. In the experiment done with the JIPP T−II−U device [2], the heating efficiency were measured for the various concentrations of the minority ion. Corresponding to this experimental situations, only the minority ion concentrations in the simulation parameters were varied for these runs: n_D/n=0.5 for run 1, 0.125 for run 2, and 0.0 for run 3, where $n=n_D+n_H$.

The spatial profile of the immersed magnetic field corresponds to the lower-field side excitation in a tokamak experiment. In the lowest-field side, the wave is launched at the position where ω/Ω_H=1.9. At this frequency, *i.e.*, ω/Ω_H=1.9, the direct excitation of the ion−Bernstein wave is presumed to be successful from the data obtained in Chapter IV. The number of particle is many enough to avoid the wave damping due to Coulomb collision.

The $3\Omega_D$ resonance region is located in the middle of the system in order to absorb the wave energy into D through the $3\Omega_D$ resonance. In the case of the heating experiment, the fundamental−hydrogen cyclotron resonance region has sometimes

been outside of the system [2]. If this region is set outside of the system in the simulation, the wave penetrates the plasma, reflects on the wall, and then propagates reversely. In this case, the observed phenomena around the position of $\omega/\Omega_D=3$ are too complex to discuss. In this simulation, therefore, we placed the hydrogen-cyclotron resonance region inside the system in order to absorb the wave energy.

In Sec. 5.2, the numerical results concerning wave propagation are presented. In Sec.5.3, the discussions with regard to energy deposition into ions are mainly made. In Sec. 5.4, we conclude with a discussion.

Table V-I Simulation parameters

Run name	run 1	run 2	run 3
$\lambda_{//}$	512	512	512
$q\ \Psi_{max.}\ /\ T_{e,\ max.}$	3.0	3.0	3.0
$(\omega\ /\ \Omega_H)$ max.	1.9	1.9	1.9
$(\omega\ /\ \Omega_H)$ min.	0.99	0.99	0.99
$(\omega\ /\ \Omega_D)$ max.	3.8	3.8	3.8
$(\omega\ /\ \Omega_D)$ min.	1.98	1.98	1.98
ω_{pe}^2 max. / $\Omega_{e,}^2$ max.	0.3	0.3	0.3
ω_{pe}^2 min. / $\Omega_{e,}^2$ max.	0.1	0.1	0.1
$m_H\ /\ m_e$	15	15	15
$m_D\ /\ m_e$	30	30	30
$T_{e,\ max.}$	1.0	1.0	1.0
$T_{e,\ min.}$	0.25	0.25	0.25
$T_{H,\ max.}$	1.0	1.0	1.0
$T_{H,\ min.}$	0.25	0.25	0.25
$T_{D,\ max.}$	1.0	1.0	1.0
$T_{D,\ min.}$	0.25	0.25	0.25
System length X direction	256	256	256
System length Z direction	512	512	512
$n_D\ /\ (n_D + n_H)$	0.5	0.125	0.0
$(v_{phase}\ /\ v_{Te//})$ max.	10.6	10.6	10.6
$(v_{phase}\ /\ v_{Te//})$ min.	5.38	5.38	5.38
Number of Electron	180334	177992	179163
Number of H	90167	155743	179163
Number of D	90167	22249	0
Stretching Factor	16	16	16

5.2 Wave propagation

In Figs. 5.1-5.3, we show the interferograms between the observed electric field perpendicular to the immersed magnetic field and the wave source signal,the values of Re $k_\perp$ measured in steady state, and the values of Re and Im $k_\perp$ calculated from the linear dispersion relation. Figures 5.1—5.3 correspond to runs 1-3, respectively. In run 1, the wave energy is almost completely absorbed around the $3\Omega_D$ resonance region, and the wave cannot penetrate toward the higher—field side beyond this resonance region. In runs 2 and 3, the waves are only partially damped through this region, and propagate to the higher—field side. Significant differences are not seen in the profiles of the electric field between runs 2 and 3 as seen in Fig.5.2 and 5.3. In these runs, the measured values of $k_\perp$ in the simulation agree well with those predicted from linear theory.

Figure 5.4 shows the wave spectra of the potential, $\phi_1(x,\omega)$, which is Fourier-analyzed with respect to both z and t; subscript 1 indicates the fundamental Fourier mode in the z direction. These wave spectra are measured at t=60T. In those runs, the amplitudes of $\phi_m(x,\omega),(m\geqq 2)$, are less by one order of magnitude than that of $\phi_1(x,\omega)$;therefore, we omit the higher-order Fourier components of the results.

In these figures, the horizontal and vertical lines indicate the frequency and amplitude of the potential, respectively,and the diagonal line shows the x direction. The position of the frequency of the wave source is shown by the dotted line. In run 1, sharp peaks around the dotted lines are observed in the region $0\leqq x<95$; however, they are not observed

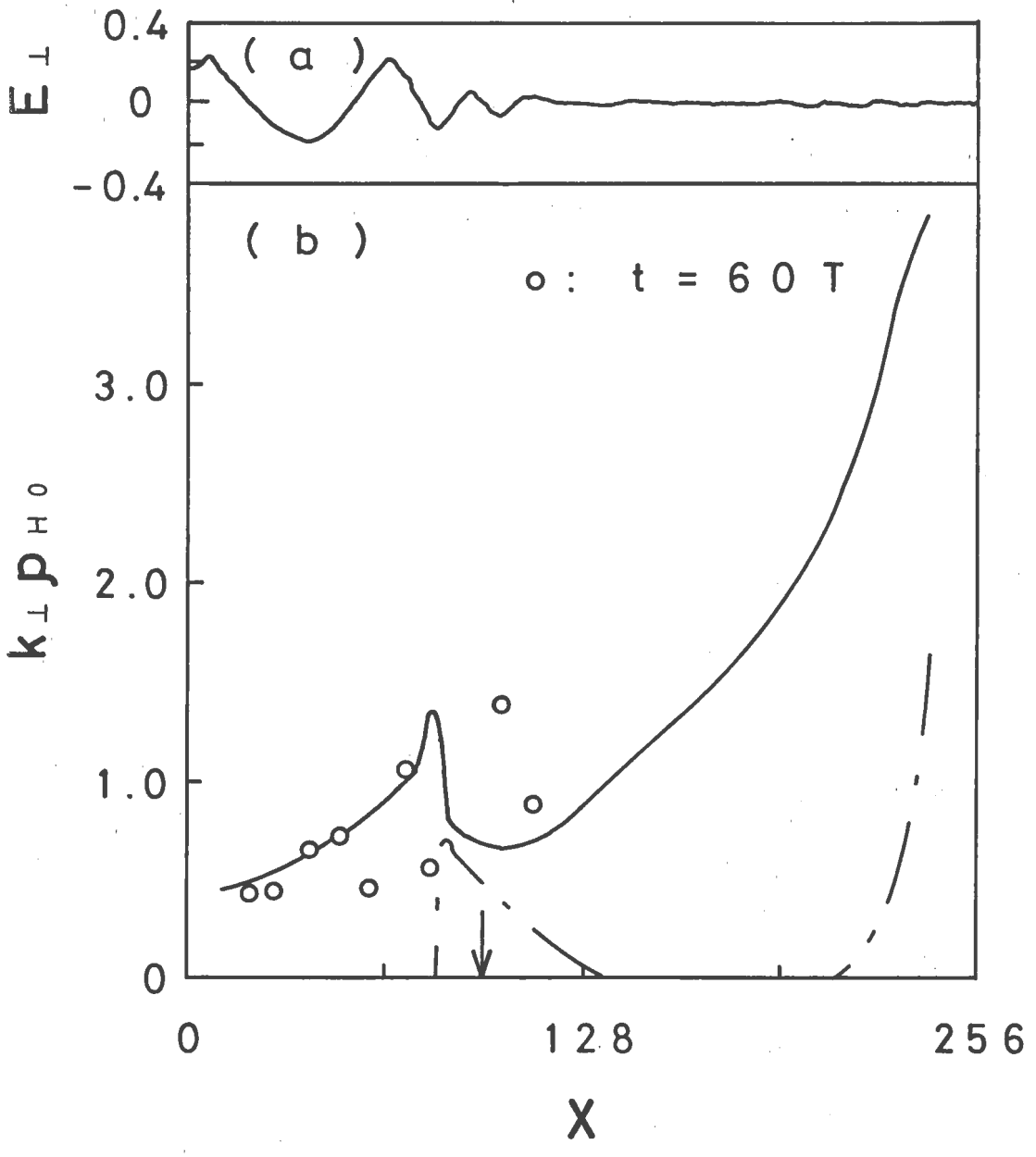

Fig.5.1. Wave interferogram and dispersion relation for run 1. (a) The x dependent interferograms of the electric field perpendicular to the immersed magnetic field. (b) $k_\perp$ vs x. The solid and dashed lines are the real and imaginary part of $k_\perp$ obtained from the calculation of the linear dispersion relation. The circles are the real part of $k_\perp$ obtained from the simulation. The arrows denote the position of the $3\Omega_D$ resonance : $\omega - k_{//} v_{TD} - 3\Omega_D = 0$

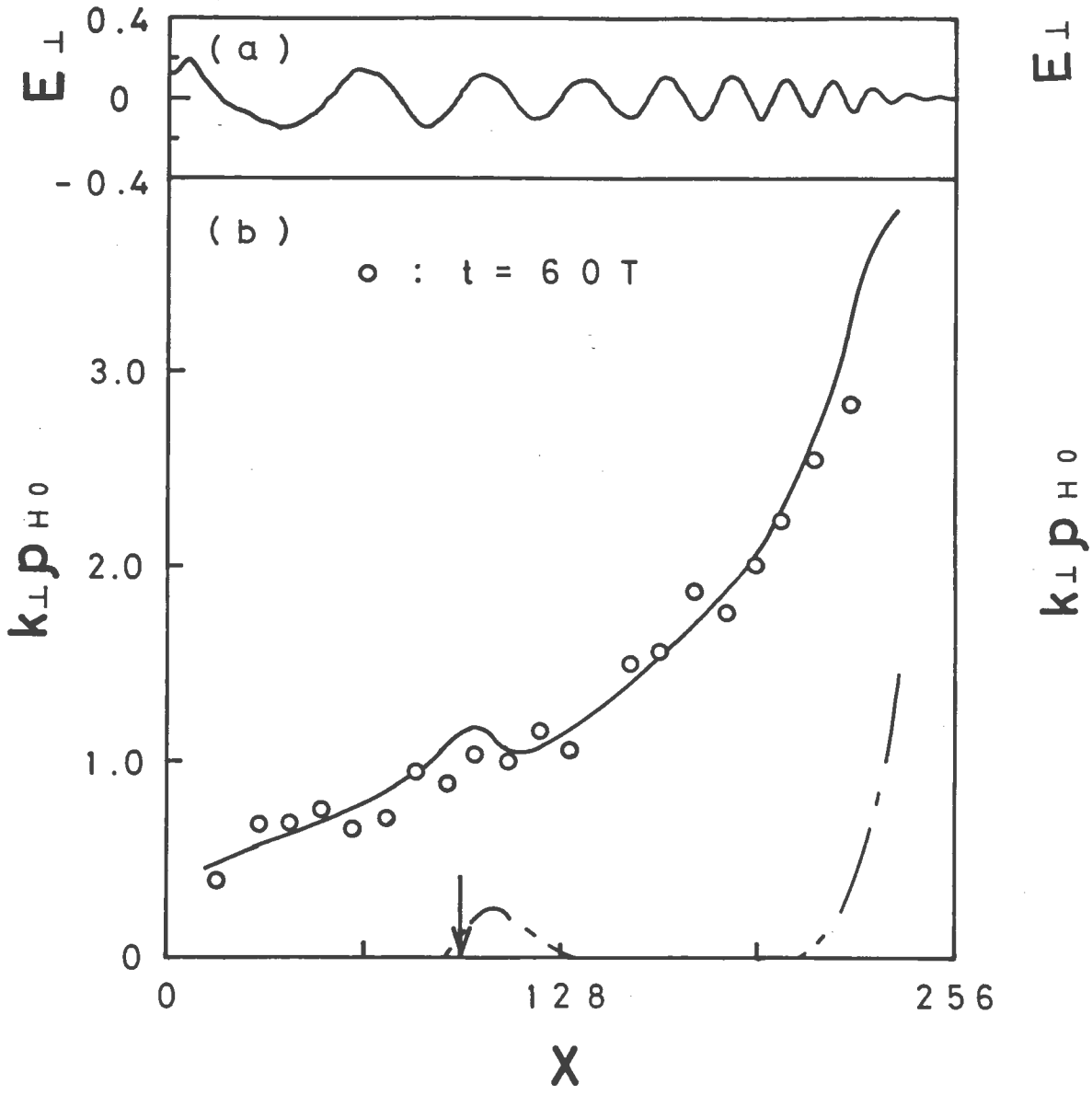

Fig. 5.2. Wave interferogram and dispersion relation for run 2. (a) The x dependent interferograms of the electric field perpendicular to the immersed magnetic field. (b) $k_\perp$ vs x. The solid and dashed lines are the real and imaginary part of $k_\perp$ obtained from the calculation of the linear dispersion relation, the circles are the real part of $k_\perp$ obtained from the simulation. The arrows denote the position of the $3\Omega_D$ resonance : $\omega - k_{//} v_{TD} - 3\Omega_D = 0$.

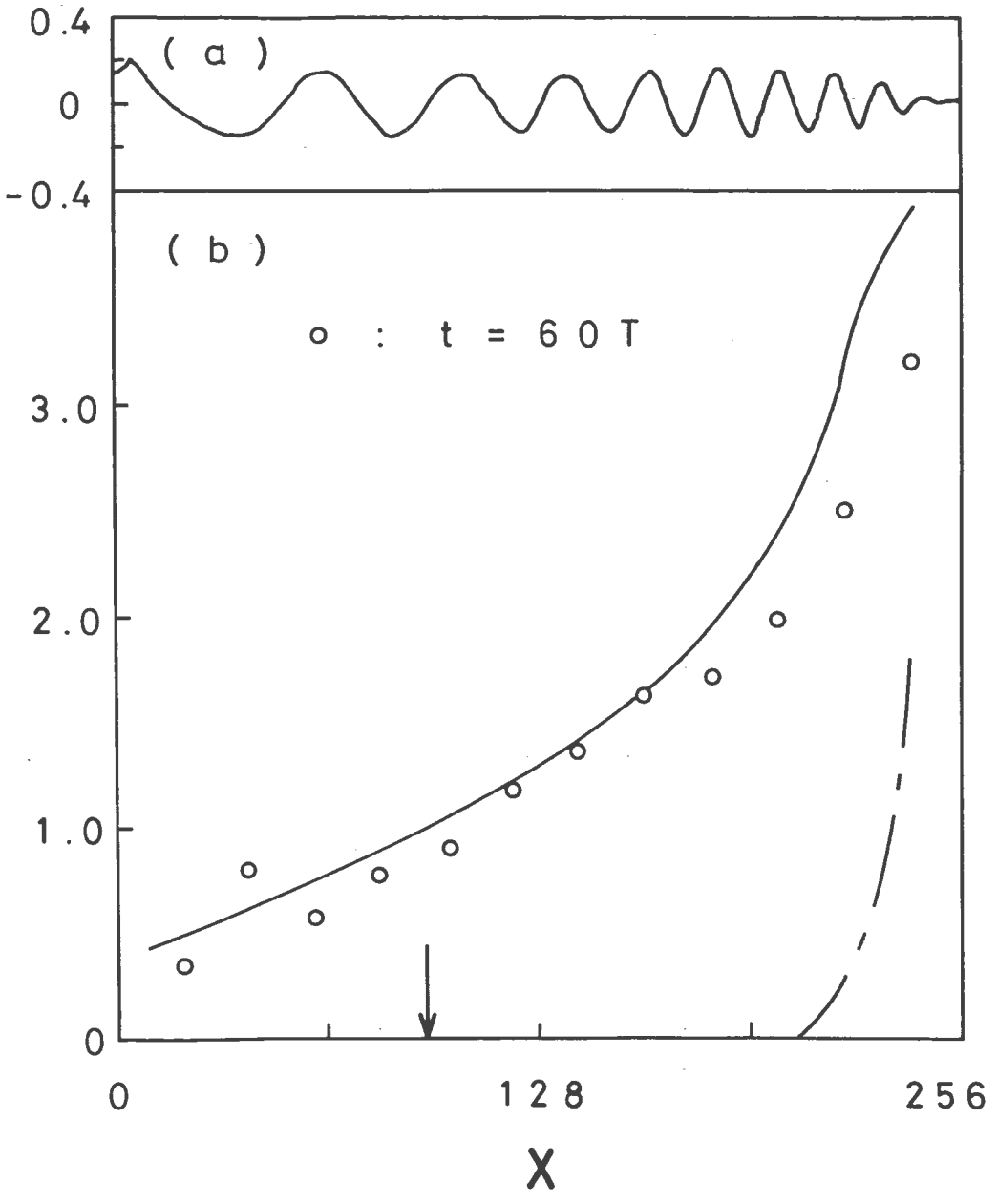

Fig. 5.3. Wave interferogram and dispersion relation for run 3. (a) The x dependent interferograms of the electric field perpendicular to the immersed magnetic field. (b) $k_\perp$ vs x. The solid and dashed lines are the real and imaginary part of $k_\perp$ obtained from the calculation of the liner dispersion relation. The circles are the real part of $k_\perp$ obtained from simulation. The arrows denote the position of the $3\Omega_D$ resonance : $\omega - k_{//} v_{TD} - 3\Omega_D = 0$.

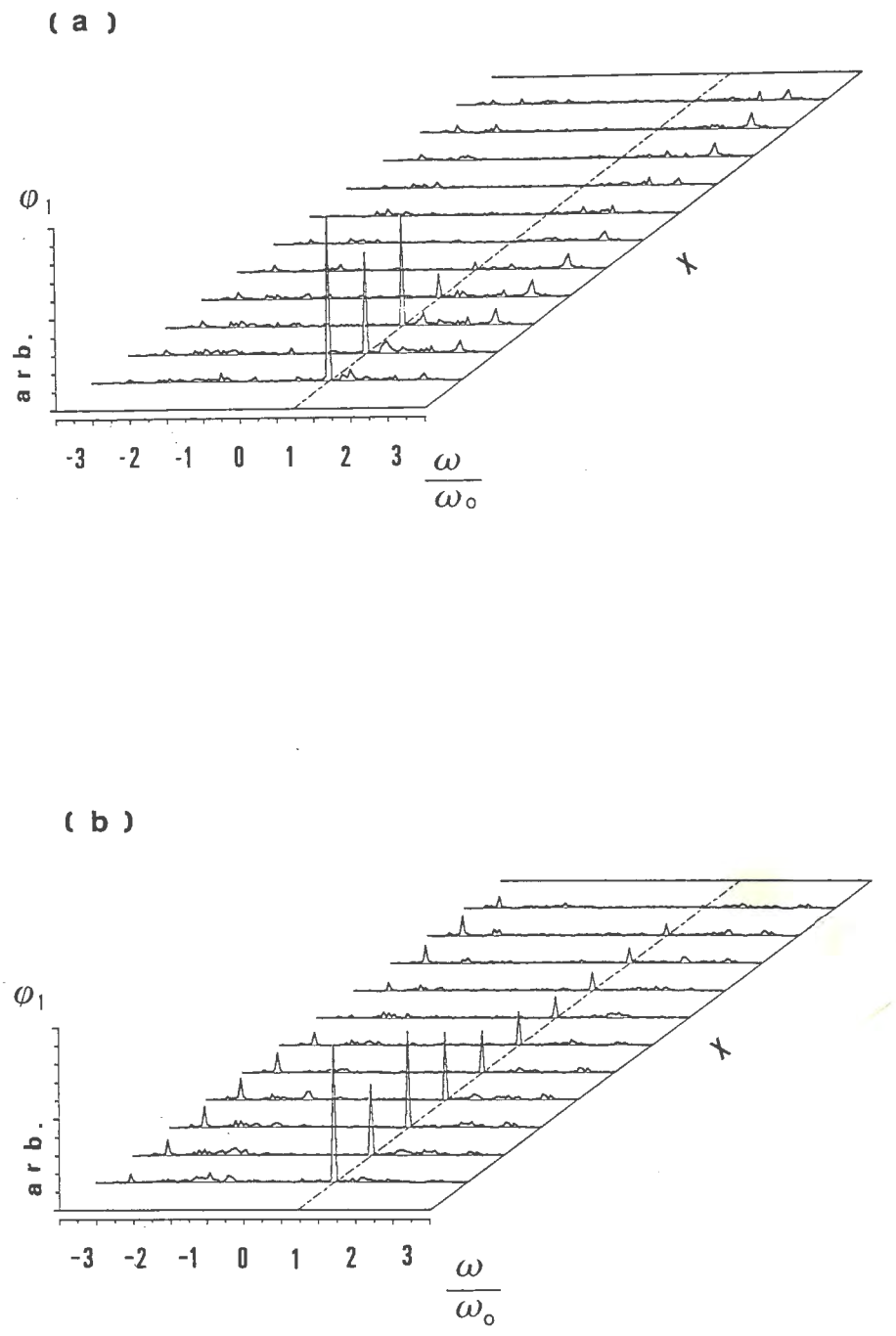

Fig. 5.4. The x dependent wave spectra of the potential for the first Fourier mode Ψ_1 (x, ω). The dashed lines indicate the position of the frequency of the wave source. (a) for run 1, (b) for run 2, and (c) for run 3.

(c)

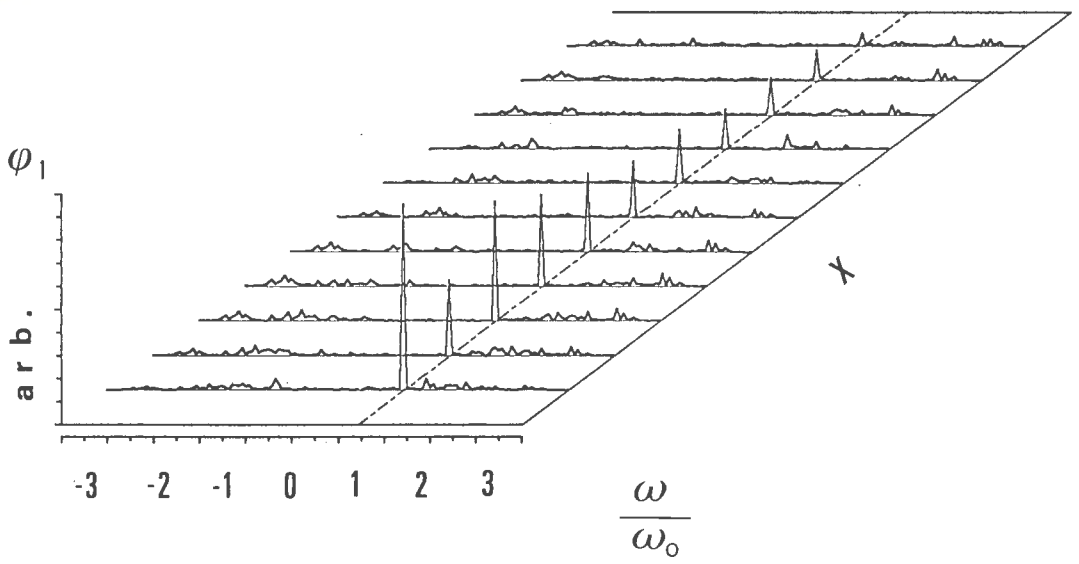

beyond the region x=95 which is near the $3\Omega_D$ resonance region. In runs 2 and 3, sharp peaks are observed throughout most of the entire region. These figures show that the excited wave in the plasma is an almost monochromatic wave with wave frequency ω and antenna wavelength $\lambda_{//}$. The fact that the excited wave is almost monochromatic is useful for analysis of the heating process in the next section.

5.3 Energy deposition to plasmas

Figure 5.5 shows the spatial profile of perpendicular energy deposition into both ions D and H, measured between region 1 and 9.

In these runs, we simulate the heating process from t=0 to $60T$. It takes time for the propagating wave to reach the highest-field side. In order to observe the ion acceleration in steady state, the measurement of the ion-energy increments is started at time t=$32T$.

The energy deposition into the electron can be neglected compared with that into ions, because the parallel phase velocity of the wave is much faster than the electron thermal velocity ($v_{ph//}/v_{Te}$=5.6~10.5) and the electron-Larmor-radius is much smaller than the perpendicular wavelength ($k_{\perp}\rho_e$=0.3).

In Fig. 5.5, the energy deposition in each region is shown by the bar graph, which is divided into two parts : the shaded part corresponds to that deposited into H and the unshaded part that into D. The profiles of the energy depositions peak around $3\Omega_D$ resonance region, the positions of which are shown by

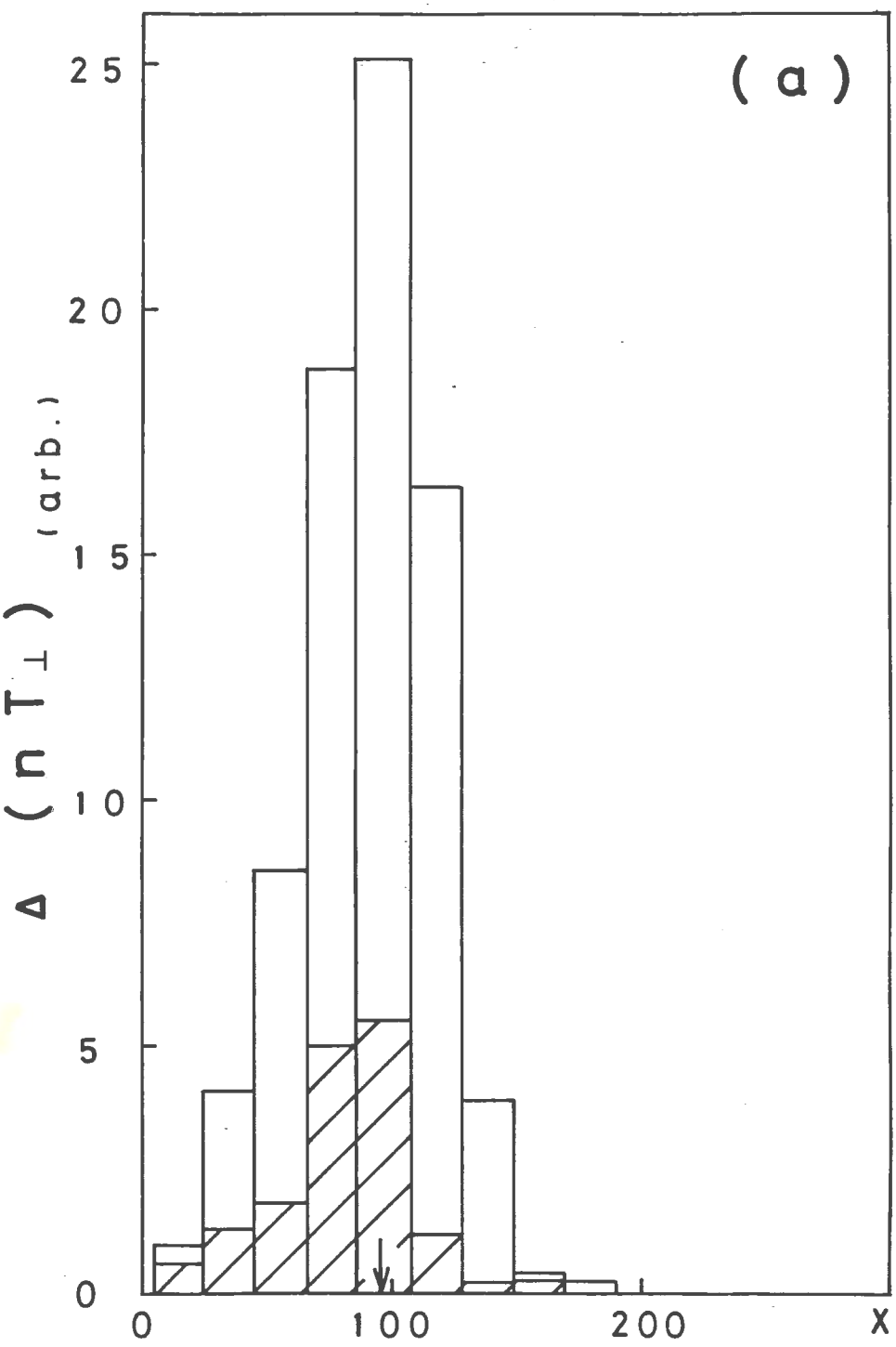

Fig. 5.5. The x dependent energy deposition into each ion : shaded parts into H, and unshaded parts into D. The arrows mean the position of $3\Omega_D$ resonance. (a) for run 1, (b) for run 2, and (c) for run 3.

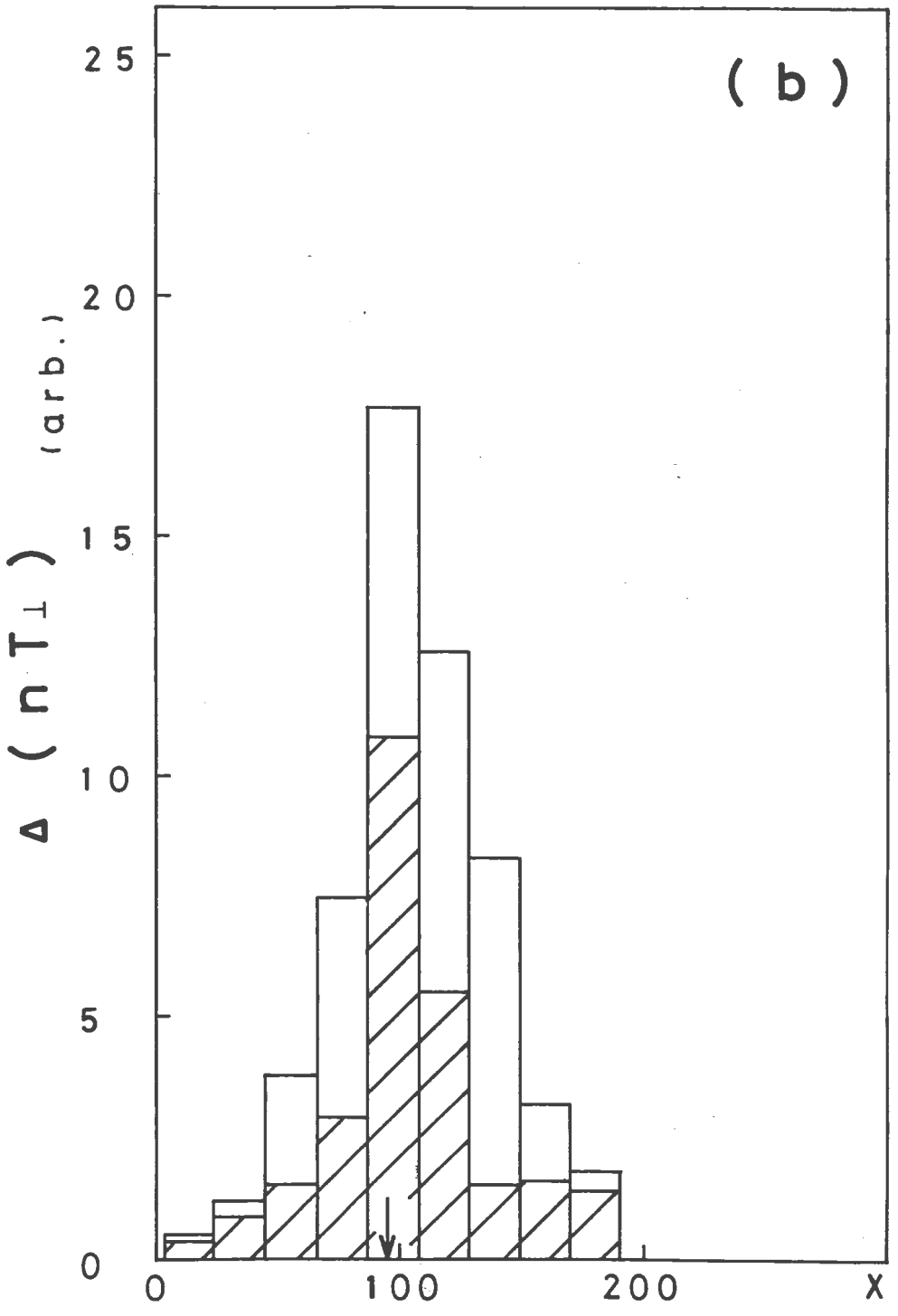
(b)
25
20
15
10
5
0
Δ (n T⊥) (arb.)
0
100
200
X

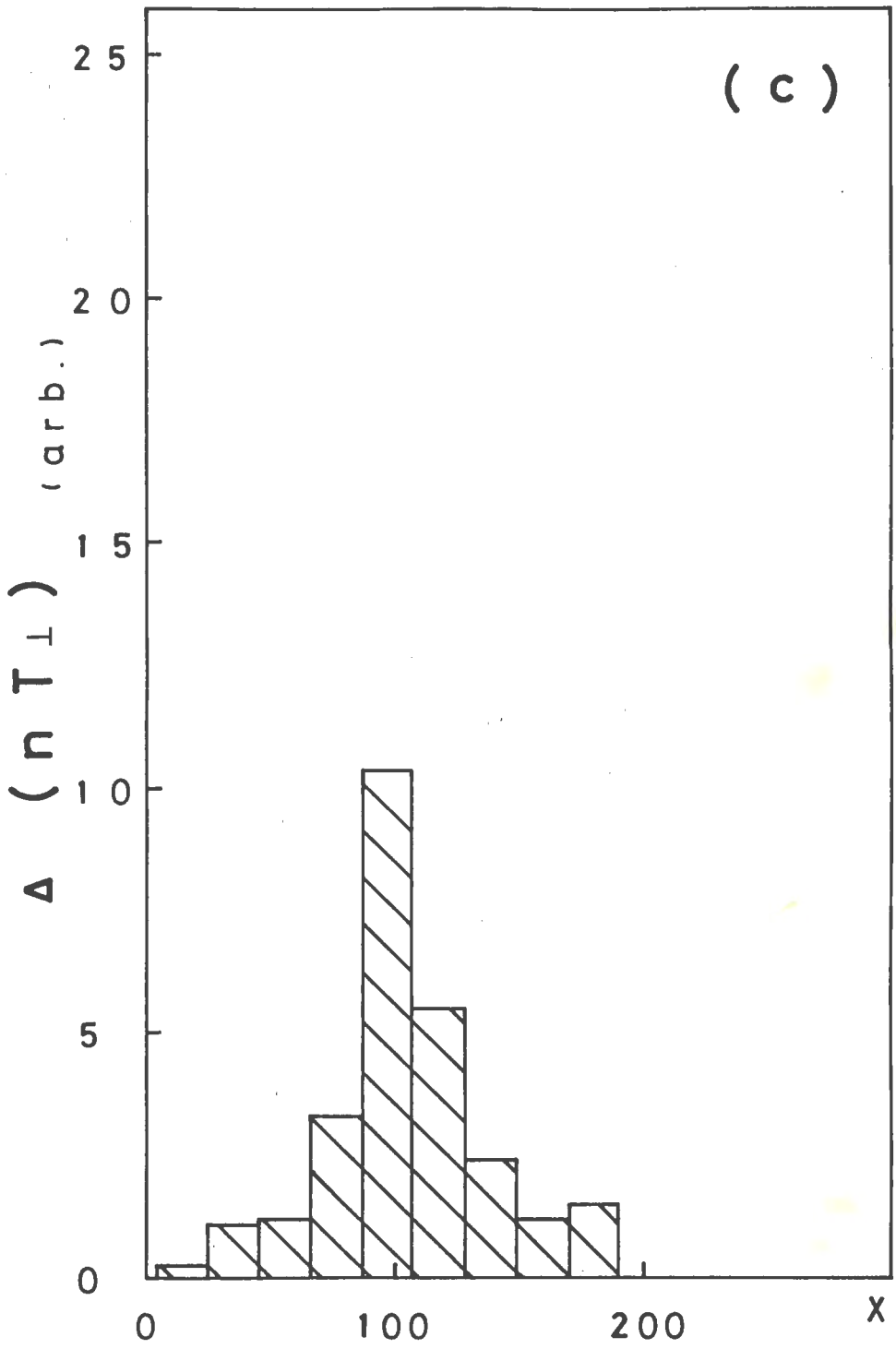
(c)
Δ (n T⊥) (arb.)
25
20
15
10
5
0
0
100
200
X

arrows in the figures. These peaks results from the localization of the energy deposition into both ion species D and H. The peaking feature of the energy deposition into D (unshaded part) can be easily understood through the theory of the usual cyclotron harmonic resonance heating because the value of ω/Ω_D is nearly equal to 3 around the peaking position. However, the profile of energy deposition into H is also observed to peak around the peaking position of the energy deposit of D.

Although one might suppose that H is heated by the thermal relaxation from D, accelerated through the $3\Omega_D$ resonance, the energy relaxation time, estimated as $2.0\times10^{4}T$ in the simulation plasma, is much longer than the simulated time $60T$. In run 3, H is accelerated around the region x=100 without the existence of D. This result shows that the acceleration of H has no relation to the existence of D. From the measurement of the potential wave spectra shown in Fig. 5.4, we can conclude that H is accelerated by the wave whose frequency is nearly equal to $3/2\Omega_H$, because the excited waves in these runs are almost monochromatic. Therefore, we conclude that the mechanism of acceleration of H is the $3/2\Omega_H$ cyclotron subharmonic resonance heating, which has been already reported [3].

The ion velocity distribution functions are measured, and their results are presented in Figs. 5.6—5.9. These velocity distribution functions are measured in region 4—6, where the $3\Omega_D$ resonance region and the cyclotron subharmonic resonance region are located.

In Fig 5.6, the velocity distribution functions of H in ln F vs $v_\perp^2$ are presented. The heating feature of H is close to so—called bulk heating, *i.e.*, the production of the high—energy

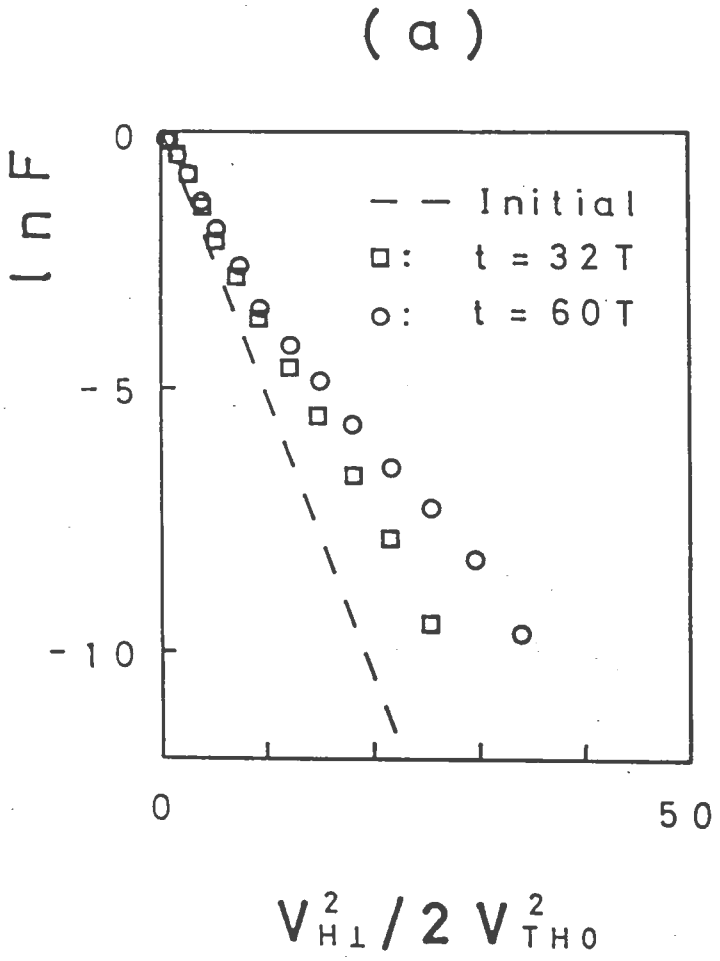

Fig. 5.6. The perpendicular velocity distribution function of H, ln F vs $v_\perp^2$ (a) for run 1, (b) run 2, and (c) for run3.

(b)

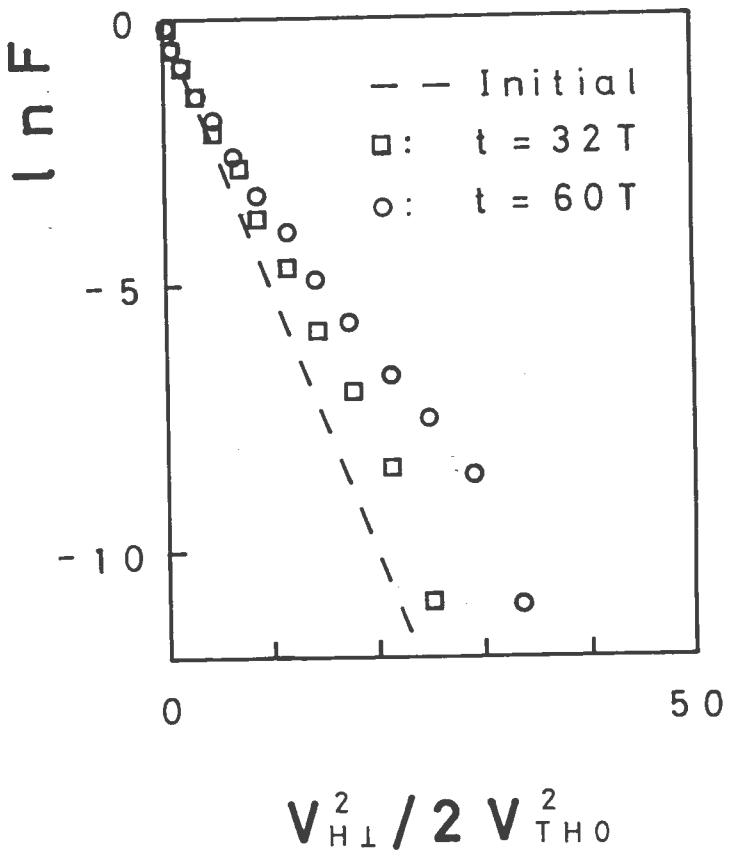
0
-5
-10
ln F
— — Initial
□: t = 32T
○: t = 60T
0
50
$V_{H\perp}^2 / 2 V_{TH0}^2$

(c)

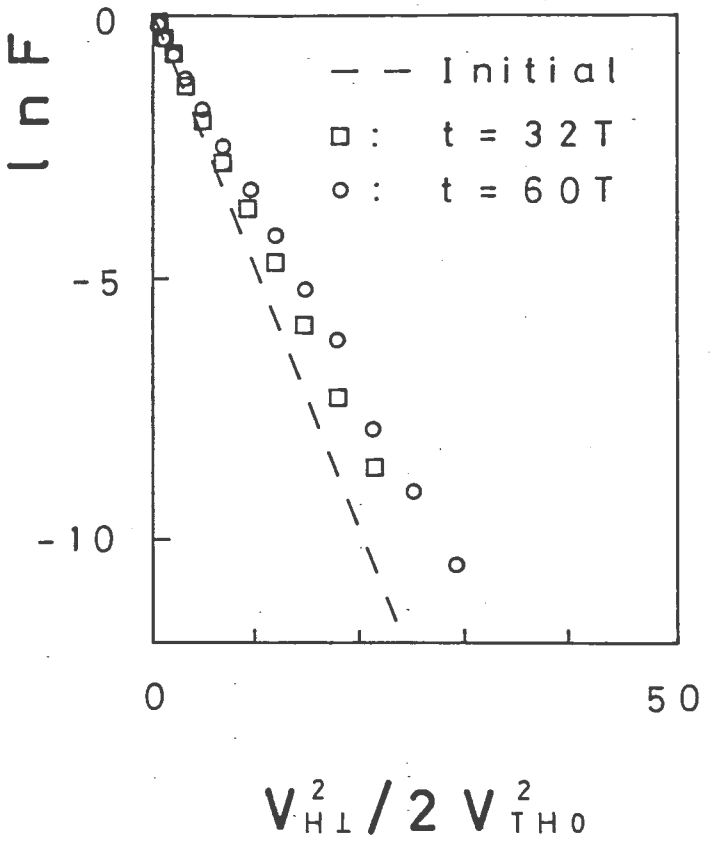
0
-5
-10
ln F
— — Initial
□: t = 32T
○: t = 60T
0
50
$V_{H\perp}^2 / 2 V_{TH0}^2$

tail is negligibly small. No differences are seen in the shape of the velocity distribution functions measured at $t=60T$ between runs 2 and 3. The maximum ion velocity at $t=60T$ is $v_H^2/2v^2_{TH0}=35$ in both runs, while, in run 1, it is $v_H^2/2v^2_{TH0}=30$, which is a little bit smaller than those in runs 2 and 3. The difference between run 1 and runs 2 and 3 is thought to be caused by the amplitude of the excited wave around the $3\Omega_D$ resonance region. In run 1, $\alpha=k^2_\perp q\Phi/m_H\Omega^2_H=0.13$ which is measured around the $3\Omega_D$ resonance region,and in runs 2 and 3, $\alpha=0.3$ which is observed near the $3\Omega_D$ resonance region. To predict the maximum velocity under the condition of a given wave potential amplitude and a given wavenumber, it is necessary to further investigate the cyclotron subharmonic heating process quantitatively.

In Fig. 5.7, we show these phase-space plots of H in ($v_\perp^2$, $v_{//}$) measured in region 4—6, where the immersed magnetic field changes as $\omega/\Omega_H=1.67\sim1.45$. In Fig. 5.7, we show the range of the velocity parallel to the immersed magnetic field, which satisfies the resonance condition $v_{//}/v_{TH0}=(\omega-3/2\Omega_H(x))/k_{//}v_{TH0}$. In these runs, the H ions whose parallel velocity $v_{//}/v_{TH0}$ satisfies this condition ($v_{//}/v_{TH0}=3.2\sim-1.25$). are accelerated strongly.

In Fig.5.8, the velocity distribution functions of D, ln F vs v^2, are shown. Comparing these results with the distribution functions of H shown in Fig. 5.6 the bulk parts are heated; however, the production of tails are also observed in both runs. In the results of run 1, a large high energy tail is observed; however, the ratio of kinetic energy and number of particles in

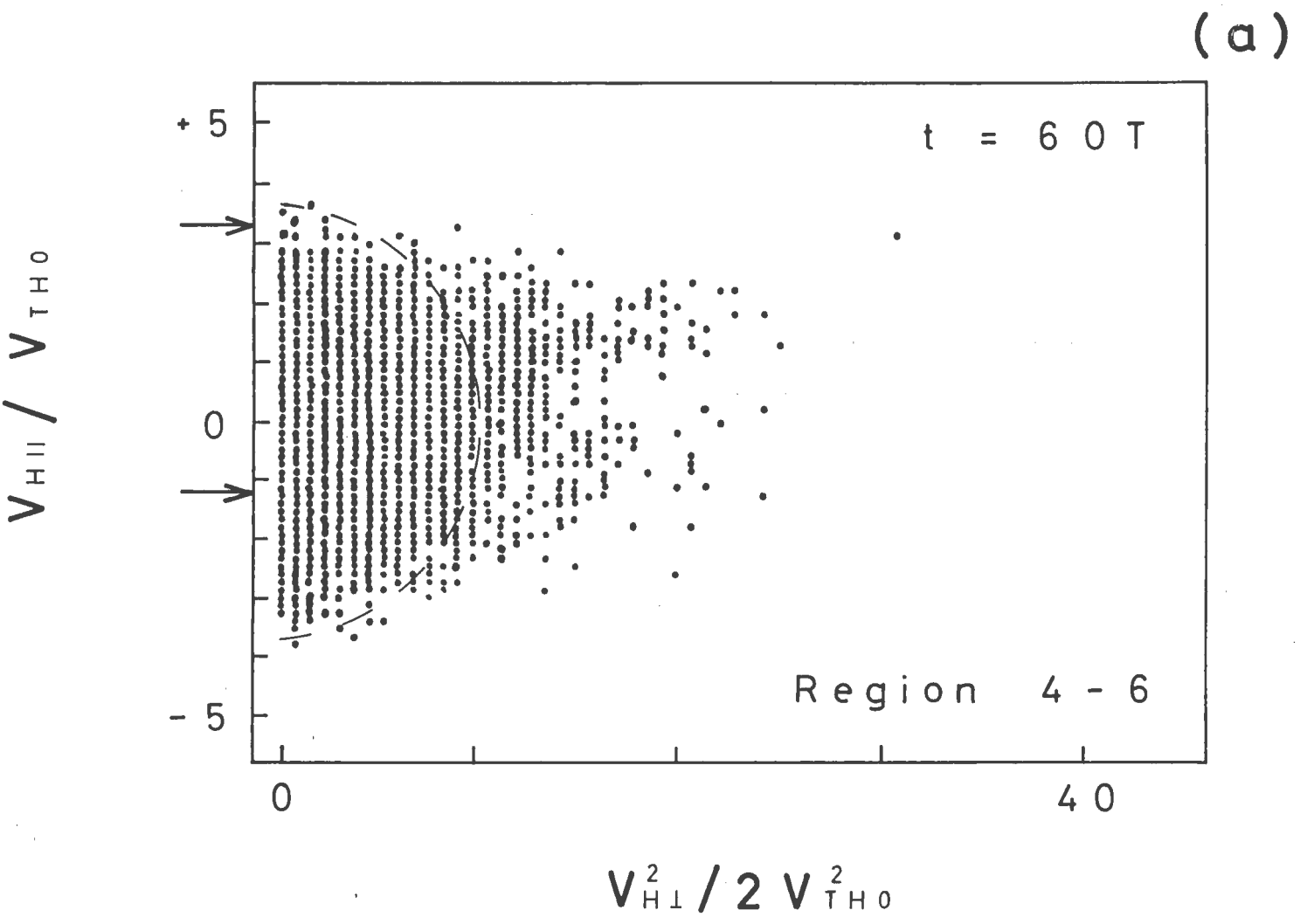

Fig. 5.7. Plots of H phase space ($v^2_\perp$, $v_{//}$) in region 4-6. The arrows mean the upper and lower limits of the parallel resonant velocities. $v_{//}=(\omega-3/2\Omega_H(x))/k_{//}$. The dashed lines indicate the boundaries of the initial distribution functions which are Maxwellian. (a) for run 1, (b) for run 2, and (c) for run 3.

(b)

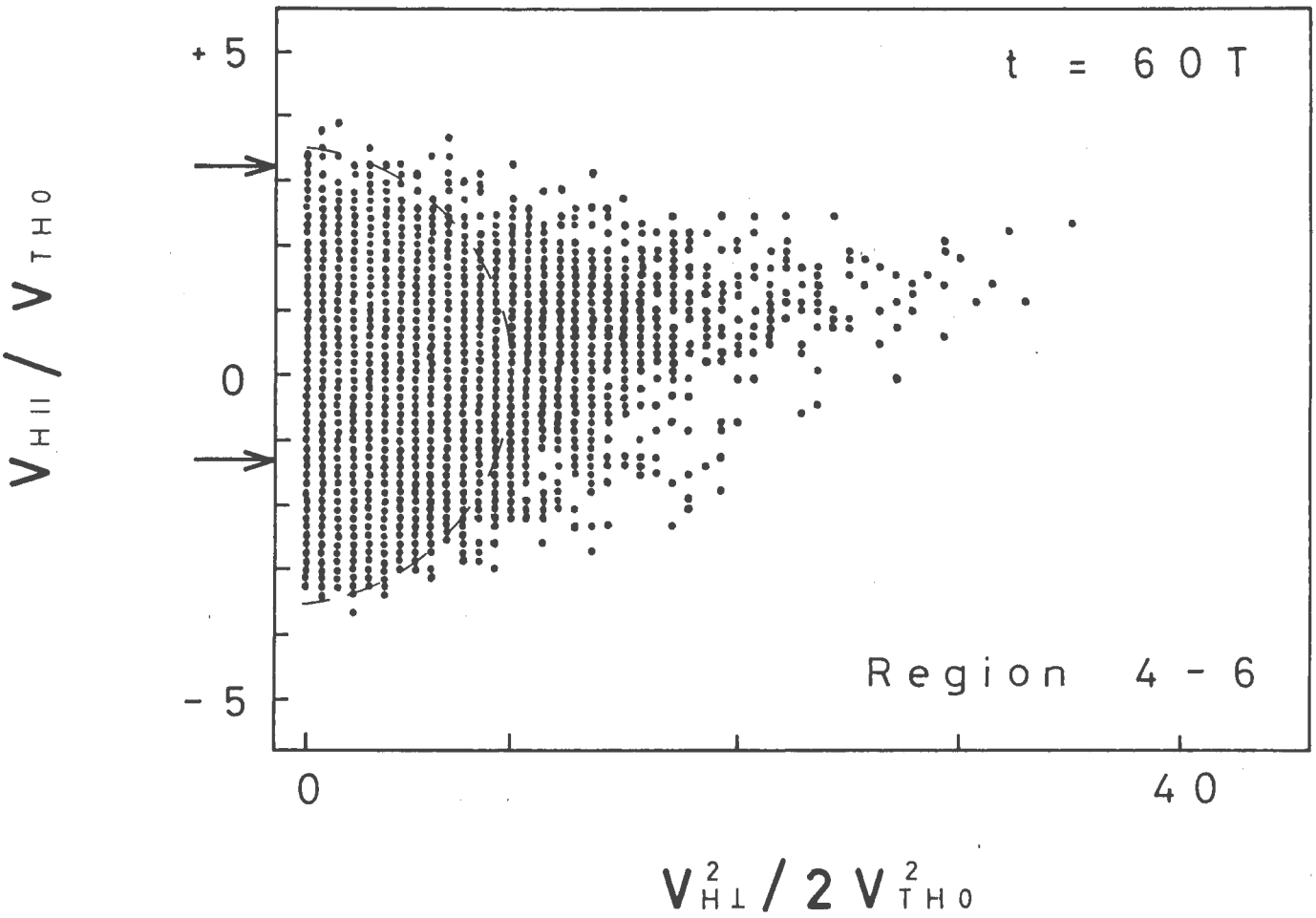

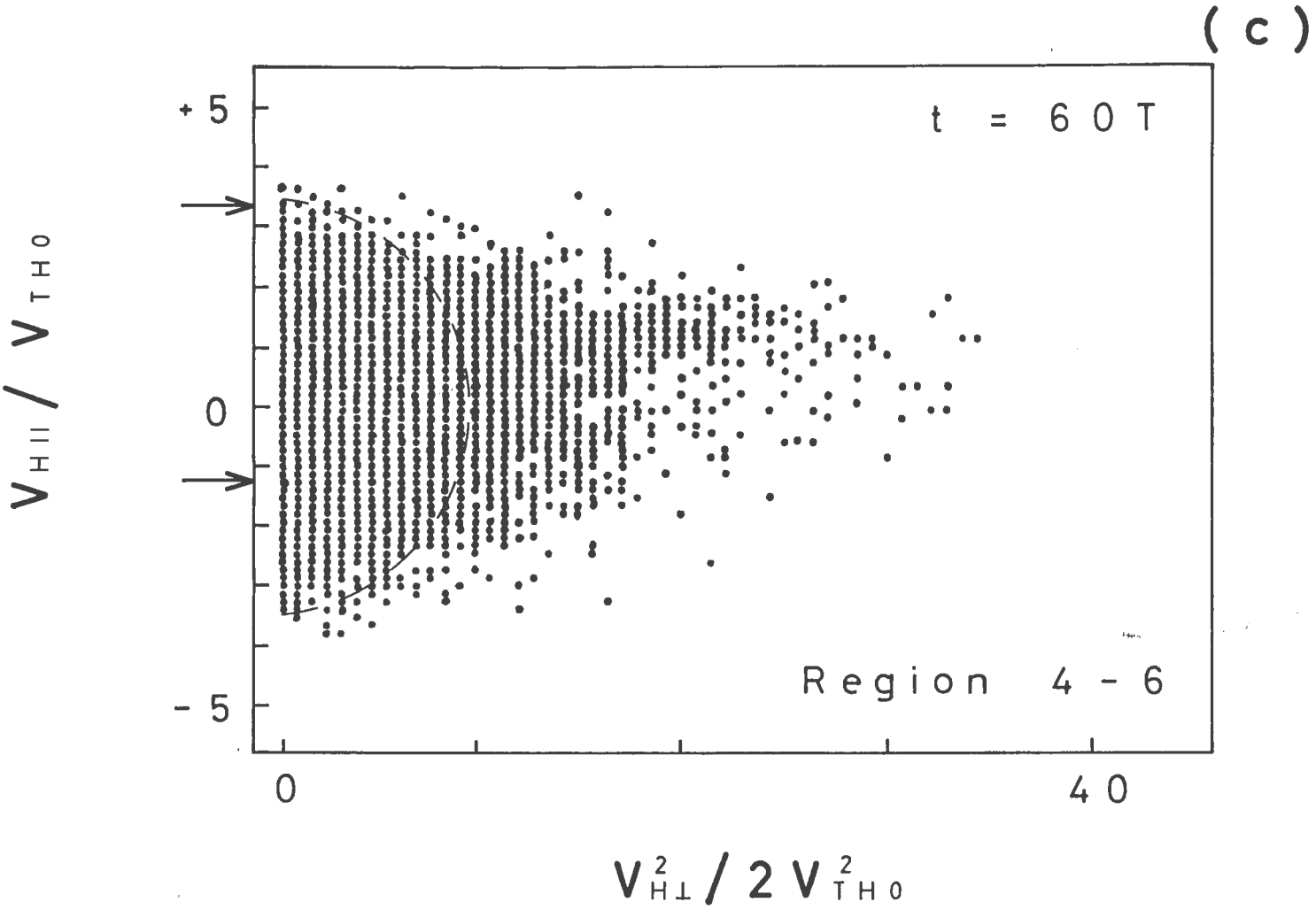
(c)
t = 60 T
Region 4 - 6
+ 5
0
- 5
0
40
$V_{H\parallel} / V_{TH0}$
$V_{H\perp}^2 / 2 V_{TH0}^2$

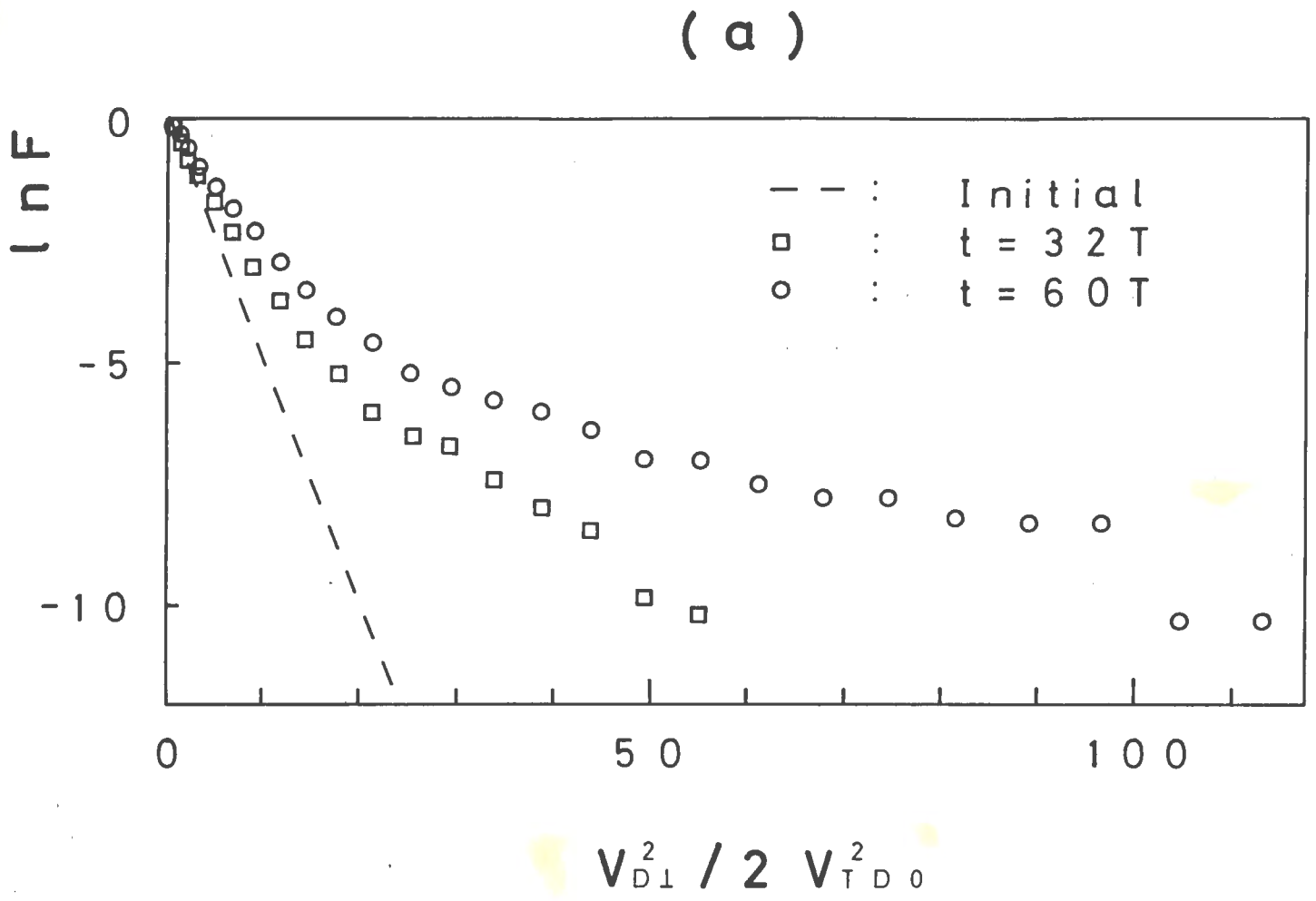

Fig. 5.8. The perpendicular velocity distribution function of D ln F vs $v_{\perp}^2$. (a) for run 1, and (b) for run 2.

(b)

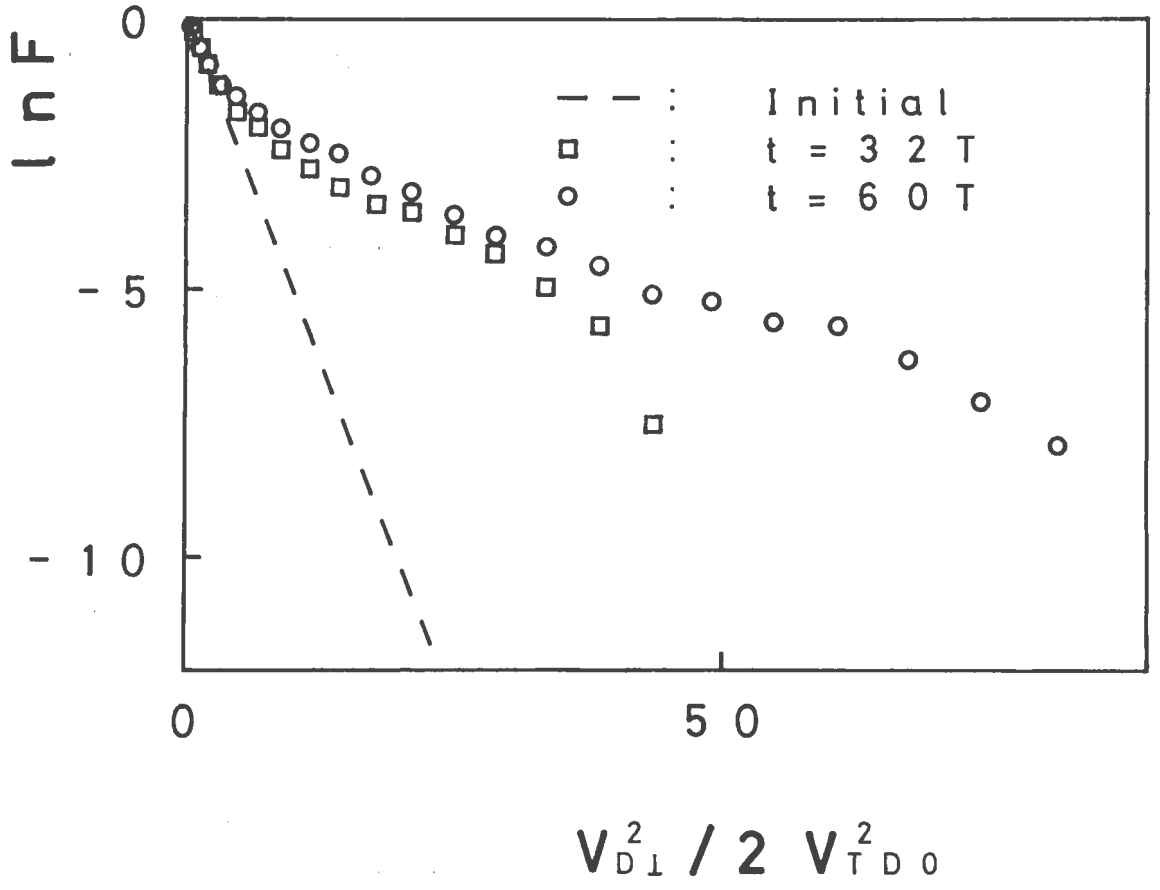

the tail to the total thermal energy and particle number in region 4—6 are 11% and 0.7%, respectively.

In Fig.5.9, we show the phase—space plot of D measured in $(v_\perp^2, v_{//})$ space to identify the heating mechanism of D with the $3\Omega_D$ resonance. In this figure, we show the range of the velocity parallel to the immersed magnetic field, which satisfies resonance condition $v_{//}=(\omega-3\Omega_D(x))/k_{//}$. The ions with the velocity $v_{//}/v_{TD0}=4.7\sim-1.8$, which satisfies this condition, are accelerated selectively. Therefore, we conclude the mechanism of acceleration of D is the third harmonic cyclotron resonance heating.

5.4 Discussion and conclusion

We have investigated the propagation of the ion—Bernstein wave and $3\Omega_D$ heating due to the ion-Bernstein wave in a two-component—ion—plasma. In this section, we will summarize the results obtained these simulation and compare them with those obtained in the experiments. With regards to wave propagation, the values of wavenumber of wave excited in the plasma agree well with those predicted employing the linear dispersion relation. Moreover, the excited waves in the plasma are almost monochromatic waves whose frequency and wavelength are nearly equal to those of wave source, respectively. These results mean that the propagation of the ion—Bernstein wave can be described well with linear theory.

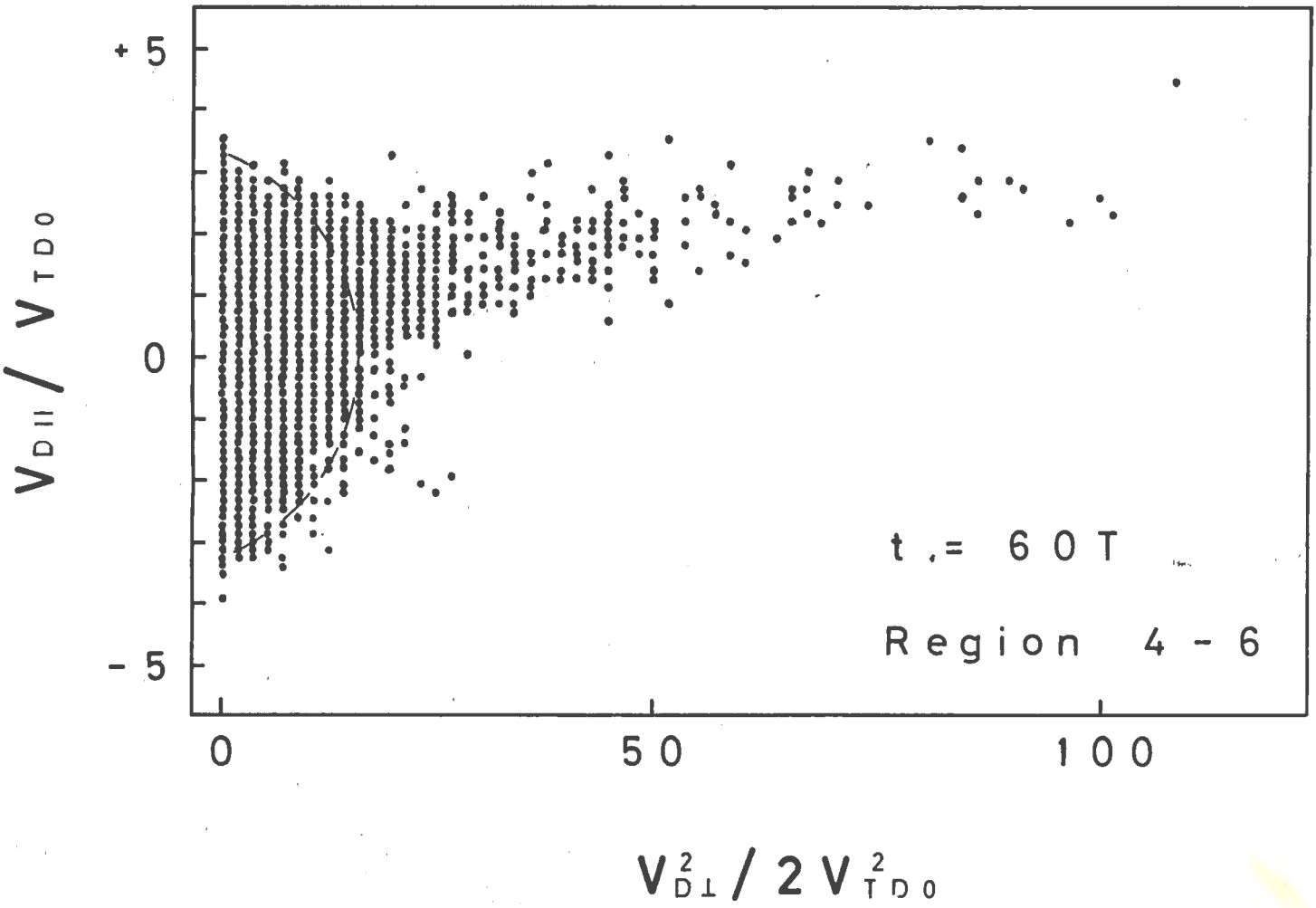

Fig. 5.9. Plots of D phase space ($v_\perp^2$, $v_\parallel$) in region 4-6 in run 1. The arrows mean the upper and lower limits of the parallel resonant velocities, $v_\parallel=(\omega-3\Omega_D(x))/k_\parallel$. The dashed lines indicate the boundaries of the initial distribution functions which are Maxwellian.

As an advantage of the $3\Omega_D$ heating, it is noted that the deposited energy is well localized around the $3\Omega_D$ resonance region in spite of the concentration of minority ion (D). However, there exists a difference between the results obtained from this simulation and those of the experiments. From the results in runs 1–3, the quantities of the energy deposited to ions depend on the concentrations of D. In run 1, in which the concentration of D is 50%, the wave energy is almost completely absorbed near the $3\Omega_D$ resonance region. However, in runs 2 and 3, in which the concentrations of D are 12.5% and 0%, respectively, only partial wave energy is absorbed around this resonance region and the wave propagates beyond this region.

In the experiment with the JIPP T–II–U device, the observed heating efficiency did not depend on the concentration of the minority ion [2]. This difference between the results obtained from the simulation and the experiment can be attributed to the difference in the system length. In order to evaluate the system length, we introduce a characteristic quantity R/ρ_H, where R is the magnetic field gradient scale length, typically equal to the major radius of the torus, and ρ_H is the Larmor radius which is the main characteristic length for the IBW [3]. In a typical tokamak experiment, this quantity is an order of $\sim 10^3$, in this simulation, this quantity is $\sim 10^2$ as is mentioned in Sec. 4.4. This means the system size for the present simulation calculation is a factor of ten smaller than that in the experiment. If the length of the simulation system becomes about ten times larger, the complete absorption of the wave energy should also be observed for runs 2 and 3. However,

the length of the simulation system is still limited by the computer memory size and time.

The reason why the spatial profile of deposited energy is localized around the $3\Omega_D$ resonance region is because of the direct absorptions through the mechanisms of the $3\Omega_D$ resonance and the $3/2\Omega_H$ cyclotron subharmonic resonance, respectively. In a pure H plasma, therefore, it is predicted that the wave energy is absorbed locally around the $3/2\Omega_H$ resonance region. In the experiment done with the JIPP T-II-U device, the wave energy was also absorbed in a plasma without the existence of D [2]. In order to explain this result, the existence of impurity ions whose specific charge was equal to that of minority ion D was assumed. However, it is suggested from our computational results that the wave energy can also be absorbed into pure H plasma, *i.e.*, without impurity ions.

With regard to the $3\Omega_D$ resonance acceleration, the properties of this acceleration were investigated numerically [4] and theoretically [4]. From the results in Ref. 4, the bulk ion is accelerated and the high-energy tail is produced simultaneously by the wave whose frequency is nearly equal to $3\Omega_D$. The shape of the velocity distribution functions of the accelerated D is similar to that in Ref. 4.

Concerning the $3/2\Omega_H$ cyclotron subharmonic heating, the properties were already studied numerically and theoretically [3]. It is shown that the bulk ion is accelerated because of a particle trapping by the wave whose frequency is $3/2\Omega_H$ [3]. In order to evaluate the relationship between the wave amplitude and the increment of the deposited energy to ion, we perform another run, called run 3S. The simulation parameters in run 3S

are the same as those in run 3 except for the amplitude of the wave source, which is 1.9 times as large as that in run 3. The increment of the ion-kinetic energy in run 3S is 3.5 times as much as that in run 3. This result suggests that the deposited energy into ion is proportional to the square of the wave amplitude.

It is already reported that ion is accelerated stochastically when the value of the normalized wave amplitude $\alpha(=k_{\perp}^{2}q\phi/m_{H}\Omega_{H}^{2})$ is greater than 0.75 with wave frequency $\omega/\Omega_{H}=1.5$ [5]. In both runs 3 and 3S, the observed ion accelerations are not stochastic since the value of α is 0.31 in run 3,and 0.57 in run 3S, which are below the threshold value of the stochastic acceleration.

REFERENCES

〔1〕 H. Okada, H. Abe, R. Itatani, and M. Ono:Phys. Fluids 29,489 (1986).

〔2〕 M. Ono, T. Watari, R. Ando, J. Fujita, Y. Hirokura, K.Ida, E. Kato, K. Kawahata, Y. Kawasumi, K. Matsuoka, A. Nishizawa, N. Noda, I. Ogawa, K. Ohkubo, M. Okamoto, K. Sato, S. Tanahashi, Y. Taniguchi, T, Tetsuka, K. Toi, and K. Yamazaki : Phys. Rev. Lett. 54,2339 (1985).

〔3〕 H. Abe, H. Okada, R. Itatani, M. Ono, and H. Okuda : Phys. Rev. Lett. 53,1153 (1984).

〔4〕 H. Abe, H. Momota, R. Itatani, and A.Fukuyama : Phys. Fluids 23,2417 (1980).

〔5〕 A. Fukuyama, H. Momota, R.Itatani, and T. Takizuka : Phys. Rev. Lett. 38,701 (1977).

〔6〕 J. Hsu : Phys. Fluids. 25,159 (1982).

Chapter VI

Computational study on the $5\Omega_D$ Heating due to the Ion-Bernstein Wave

6.1 Introduction

The purpose of this chapter is to investigate higher-harmonic launching at and heating the $5\Omega_D$ and $5/2\Omega_D$ resonance through particle simulation and to compare the results those with in the $3\Omega_D$ heating presented in the previous chapter [1]. In this regime, the wave is launched just below $3\Omega_D$, and therefore, requires higher-order Larmor radius terms for launching and propagation [2]. One motivation for the $5\Omega_D$ heating study is to investigate the physics of the high harmonic IBW heating where due to its relatively high frequency nature, more compact waveguide couplers can be utilized. The $5\Omega_D$ heating was investigated in the ACT-1 device [3], and also recently, it was observed in the PLT device [4] It should be also mentioned that an attractive heating regime at $5\Omega_D$ was identified in the Intor IBW Ignition Study [5]. As to the scheme of $5\Omega_D$ heating, moreover, it is predicted that the non-resonant ions are directly accelerated through the cyclotron subharmonic resonance around the region where the value of ω/Ω_H is nearly equal to 5/2 [6, 7]. It is also main purpose of this chapter to confirm the direct energy absorption through the $5/2\Omega_H$ subharmonic resonance [6].

Two runs, called run 1 and 2, are preformed. The simulation parameters in these runs are the same except the

concentration of the minority ion D. In run 1, the ion concentration (n_D, n_H) is (25%, 75%), In run 2, this value is (0%, 100%). These simulational parameters are presented in Table VI-I.

In the $5\Omega_D$ heating process, the wave is launched at the position where the values of (ω/Ω_D, ω/Ω_H) is just below (6, 3). In the center of the system the wave encounters the $5\Omega_D$ and the $5/2\Omega_H$ and the $5/2\Omega_H$ subharmonic resonance region. In the highest-field side, $4\Omega_D$ ($2\Omega_H$) resonance region is located inside the system to absorb the residual wave energy transmitted through the $5\Omega_D$ ($5/2\Omega_H$) resonance region to prevent the occurrence of unwanted standing waves which might make the physics in the $5\Omega_D$ resonance region complicated. Unwanted standing wave is generated by forward-propagating wave excited by wave source and backward-propagating wave reflected on the perfect conducting wall in the right-hand side. We, therefore, show the computational results measured between region 1 to region 8, whose terms are already explained in Sec. 2.3. In a typical experiment, this $2\Omega_H$ resonance region is set to be outside the system.

In Sec. 6.2, the results of wave propagation are presented, while Sec. 6.3 shows the results of (D-H) plasma heating. A discussion is given in Sec 6.4.

Table VI-I Simulation parameters

Run name	Run 1	Run 2
$\lambda_{//}$	512	512
$q\ \Psi_{max.}\ /\ T_{e,\ max.}$	3.0	3.0
$(\omega\ /\ \Omega_H)_{\ max.}$	2.9	2.9
$(\omega\ /\ \Omega_H)_{\ min.}$	1.99	1.99
$(\omega\ /\ \Omega_D)_{\ max.}$	5.8	
$(\omega\ /\ \Omega_D)_{\ min.}$	3.98	
$\omega_{pe}^{\ 2}{}_{\ max.}\ /\ \Omega_{e,}^{\ 2}{}_{\ max.}$	0.55	0.55
$\omega_{pe}^{\ 2}{}_{\ min.}\ /\ \Omega_{e,}^{\ 2}{}_{\ max.}$	0.50	0.50
$m_H\ /\ m_e$	15	15
$m_D\ /\ m_e$	30	
$T_{e,\ max.}$	1.0	1.0
$T_{e,\ min.}$	1.0	1.0
$T_{H,\ max.}$	1.7	1.7
$T_{H,\ min.}$	0.85	0.85
$T_{D,\ max.}$	1.7	
$T_{D,\ min.}$	0.85	
System length X-direction	256	256
System length Z-direction	512	512
$n_D\ /\ (n_D + n_H)$	0.25	0.0
$(v_{phase}\ /\ v_{Te//})_{\ max.}$	10.8	10.8
$(v_{phase}\ /\ v_{Te//})_{\ min.}$		10.8
Number of Electron	499712	499712
Number of H	374784	374784
Number of D	124928	0
Stretching Factor	16	16

6.2 Wave propagation

Figure 6.1(a) shows the interferogram between the observed electric field and the wave source signal in run 1. Figure 6.2(a) shows the same physical quantity in run 2. In Fig. 6.1(b) and 6.2(b), circles denote the values of wavenumber perpendicular to the external magnetic field observed in run 1 and 2, respectively. Comparing the results obtained in both run 1 and 2, we find the results from these two runs to be quite similar except the resonance-like discontinuity occurring for run 1 due to the $5\Omega_D$ resonance.

The numerical results shown in both Fig. 6.1 (b) and 6.2 (b) correspond to the dispersion relation ($k_\perp\rho_{H0}$, ω/Ω_H). Actually, the vertical axis corresponds to the finite-Larmor-radius term $k_\perp\rho_{H0}$. On the other hand, the horizontal axis corresponds to the position x. In the x direction, only the strength of external magnetic field changes drastically ($3>\omega/\Omega_H>2$) ; on the contrary, the density changes slightly as shown in Table VI-I. The horizontal axis, therefore, corresponds to ω/Ω_H.

In order to compare the simulational results with linear theory, the electrostatic linear dispersion relation [7]. is calculated and the results are shown in Fig. 6.1(b) and 6.2(b) which are in run 1 and 2, respectively. From linear theory, there is some difference between run 1 and 2 in the values of the real and imaginary parts of wavenumber $k_\perp$ (which are denoted as Re $k_\perp$ and Im $k_\perp$, respectively) around the $5\Omega_D$ resonance region located near the position of x=100.

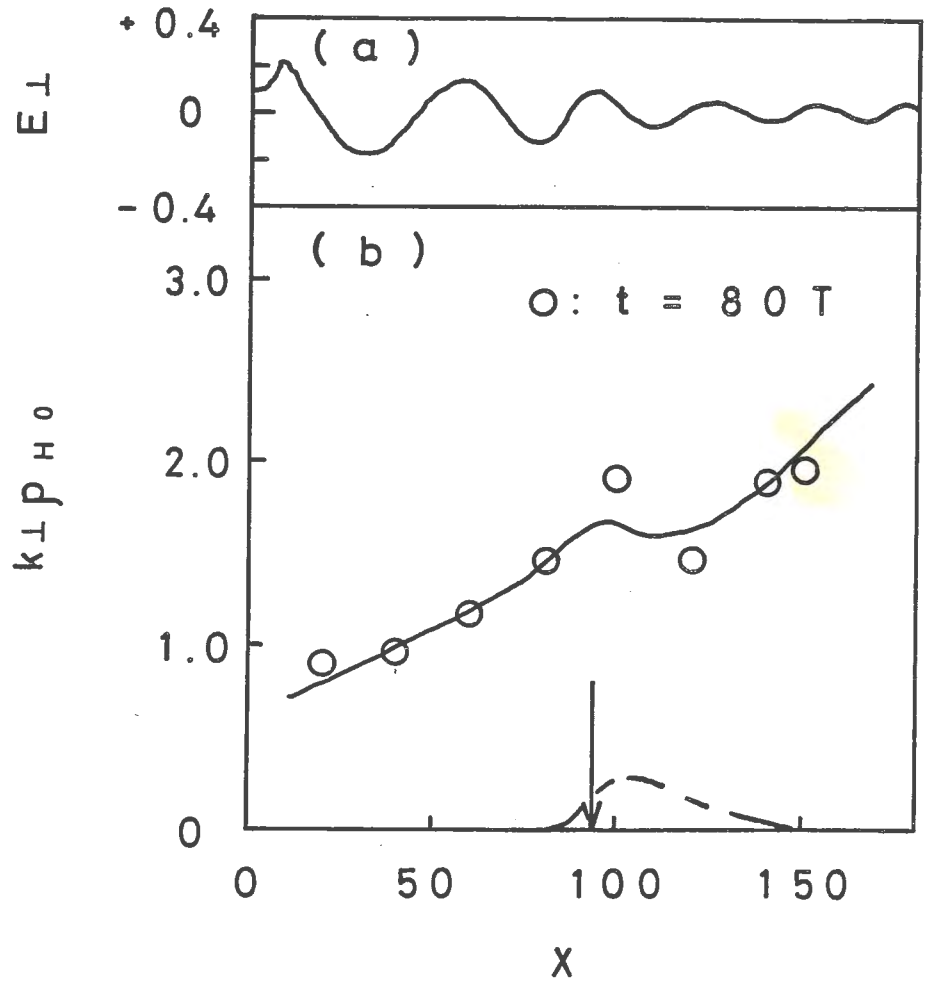

Fig.6.1. Wave interferogram and dispersion relation in run 1. (a) The x dependent interferogram of the electric field perpendicular to the immersed magnetic field. (b) $k_{\perp}$ vs x. the solid and dashed lines are the real and imaginary part of obtained from the calculation of the linear dispersion relation. The circles are the real part of $k_{\perp}$ obtained from the simulation. The arrows denote the position of the $5\Omega_D$ resonance : $\omega - k_{//}\, v_{TD} - 5\Omega_D = 0$.

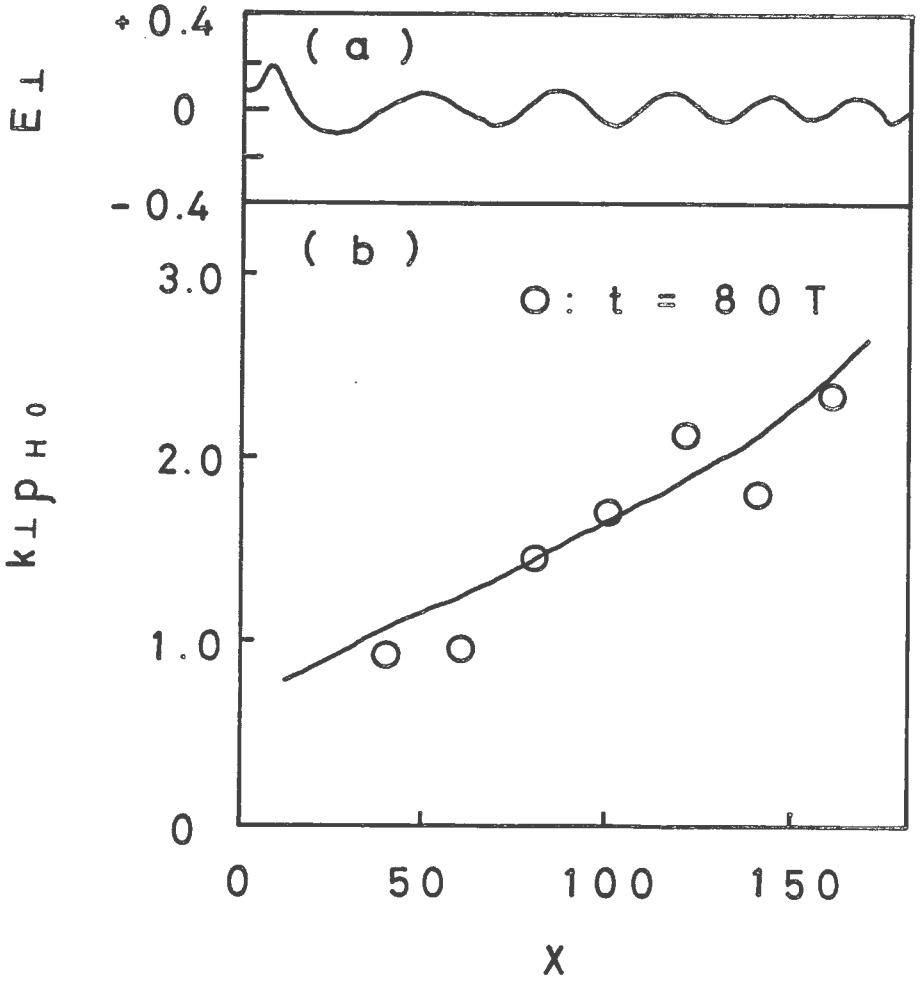

Fig.6.2. Wave interferogram and dispersion relation in run 2. (a) The x dependent interferogram of the electric field perpendicular to the immersed magnetic field. (b) $k_{\perp}$ vs x. The solid line is the real part of $k_{\perp}$ obtained from the calculation of the linear dispersion relation. The circles are the real part of obtained from the simulation.

This difference is due to the difference of the concentration of D which has its fifth cyclotron harmonic resonance around the center of the system. In run 1, the values of Re $k_\perp$ become larger toward the $5\Omega_D$ resonance region and have the maximum value around this region. The values of Im $k_\perp$ in run 1 become finite around this resonance region. On the other hand, in run 2, the values of Re $k_\perp$ become larger monotonously toward the higher field side, and the values of Im $k_\perp$ are much smaller than those of Re $k_\perp$ in the whole region. In run 2, the wave damping is not predicted from the linear theory near the center of the system.

In both run, the values of the wavenumber obtained from the simulation agree reasonably well with those calculated from the linear theory.

In Fig.6.2 (a), it seems that the wave amplitude swells as wave propagates toward the higher-field side, *i.e.*, the resonance region. This results can be explained qualitatively as follows. As wave propagates toward resonance region, group velocity v_g becomes to deteriorate, which is obvious from the dispersion relation of the ion-Bernstein wave. Group velocity v_g relates to energy flow density S and energy density W as $S=Wv_g$. Assuming that wave energy is absorbed only in resonance region, energy flow density S should be conserved in propagating region. Energy density should become to be larger as group velocity v_g becomes to be smaller, because energy flow density should be conserved. Energy density W is proportional to E^2, where E denotes the magnitude of electric field. Therefore, E swells as the decrease of group velocity.

In the above-mentioned discussion, we have neglected the changes of plasma permittivity. Actually, energy density W is a function of both E and plasma permittivity. Plasma permittivity changes with change of plasma parameters, *i.e.*, strength of magnetic field, plasma density, and plasma temperature. In order to treat this problem accurately, it is required to solve wave equation under consideration of boundary conditions and plasma inhomogeneity. Such treatment has already been made by A. Fukuyama *et al.* [8].

Figures 6.3(a) and 6.3(b) show the wave spectra of the potential in run 1 and 2 which are Fourier-analyzed with respect to both z and t. In both figures Fig. 6.3(a) and 6.3(b), the sharp peaks are observed closely around the dotted lines which denote the frequency of the wave source. In both runs, we find that amplitudes of wave with the source frequency are much larger than those of the waves whose frequencies are different from that of the source wave. These non-driven disturbance are due to the system noise. In Figs. 6.3(a) and 6.3(b), we showed only the first Fourier-analyzed component(m=1), because the amplitude of the higher modes($m \geqq 2$) are much smaller than that of the first mode(m=1).

These figures show that the almost monochromatic waves with the source frequency and wavelength parallel to the external magnetic field are excited both runs 1 and 2.

6.3 Energy deposition to ions

In both run 1 and 2, the absorbed energy into electrons is negligibly small because the phase velocity of the source wave

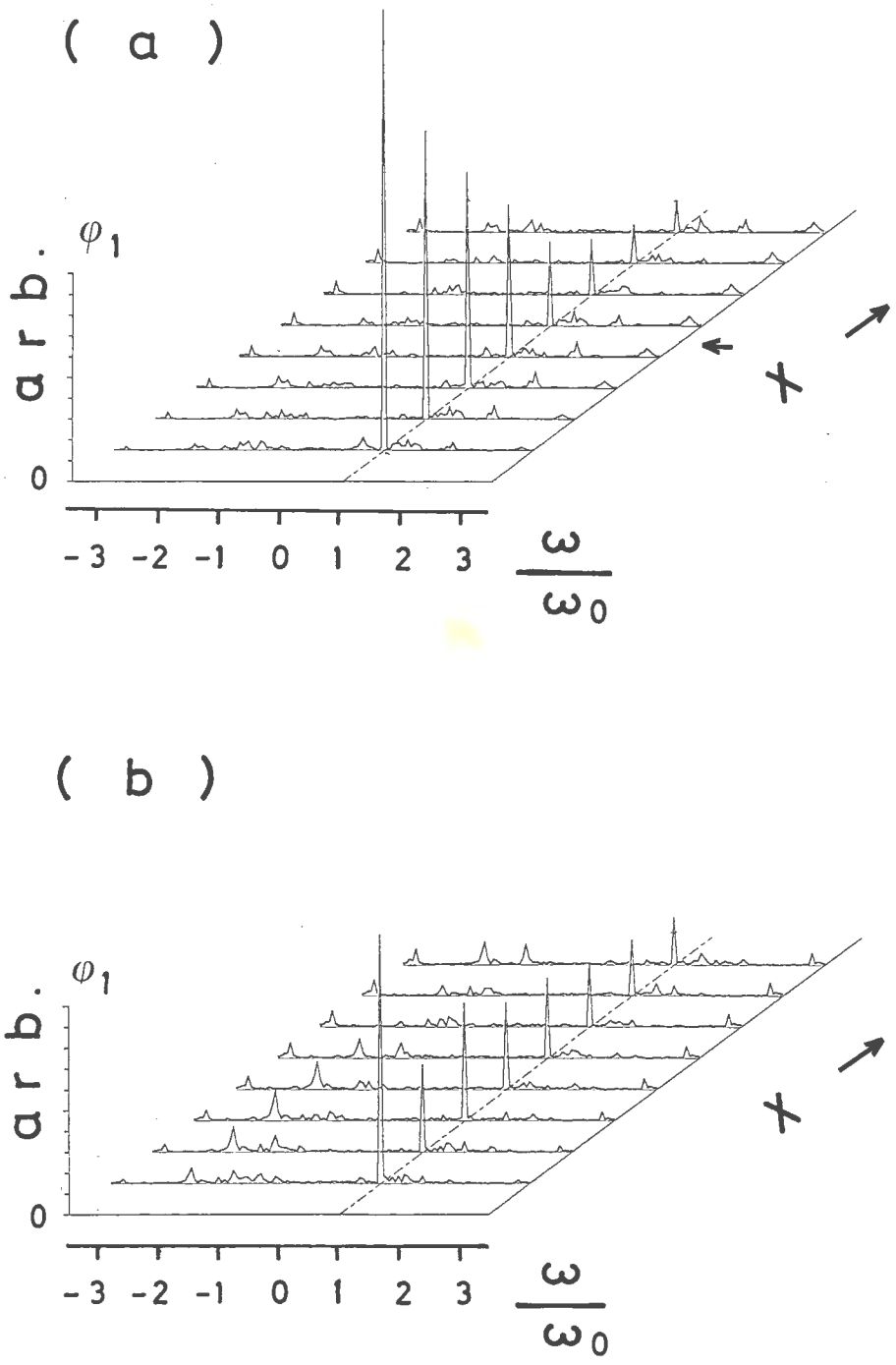

Fig.6.3. The x dependent wave spectra of the potential for the first Fourier mode in run 1. The dashed lines indicate the position of the frequency of the wave source. (a) in run 1. The arrow means the position of $5\Omega_D$ resonance : $\omega - k_{//} v_{TD} - 5\Omega_D = 0$. (b) in run 2.

is much faster than the electron thermal velocity $v_{ph//}/v_{Te}=10.8$, and the magnitude of the finite-electron-Larmor-radius term $k_{\perp}\rho_e$ is less than 0.36. Actually, the increments of electron kinetic energy are only one percent to the initial kinetic energy of electron. We, therefore, will only discuss the absorbed energy into ions.

Figures 6.4 and 6.5 show the x dependent profiles into both ions D and H. Figure 6.4 is the observed results in run 1, and Fig. 6.5 is in run 2. These observations are started at $28T$ to measure the ion kinetic energy increments in the steady state.

In run 1 shown in Fig. 6.4, the wave energy is locally deposited around the $5\Omega_D$ resonance region located in the center of the system. The sharp localization is caused by the localized energy absorption into both D (unshaded part in Fig. 6.4) and H (shaded part in Fig. 6.4), respectively.

In run 2 shown in Fig. 6.5, the localized energy deposition profile is also observed notwithstanding that there is no cyclotron resonance region in the system, and the damping of the wave is not predicted from the linear theory.

The localization of the energy absorption into D, which is shown in Fig. 6.4, is easily understood from the results using the linear theory shown in Fig. 6.1. The acceleration mechanism of D is thought to be the $5\Omega_D$ resonance. However, the acceleration of H observed in the center of the system is not predicted from the usual linear theory.

On the other hand, the particle acceleration around the frequency of $\omega=5/2\Omega_H$ is predicted by Abe and Okada *et al.* [6] and Porkolab [7]. In run 1 and 2, the excited waves in the plasmas are almost monochromatic with the source frequency and

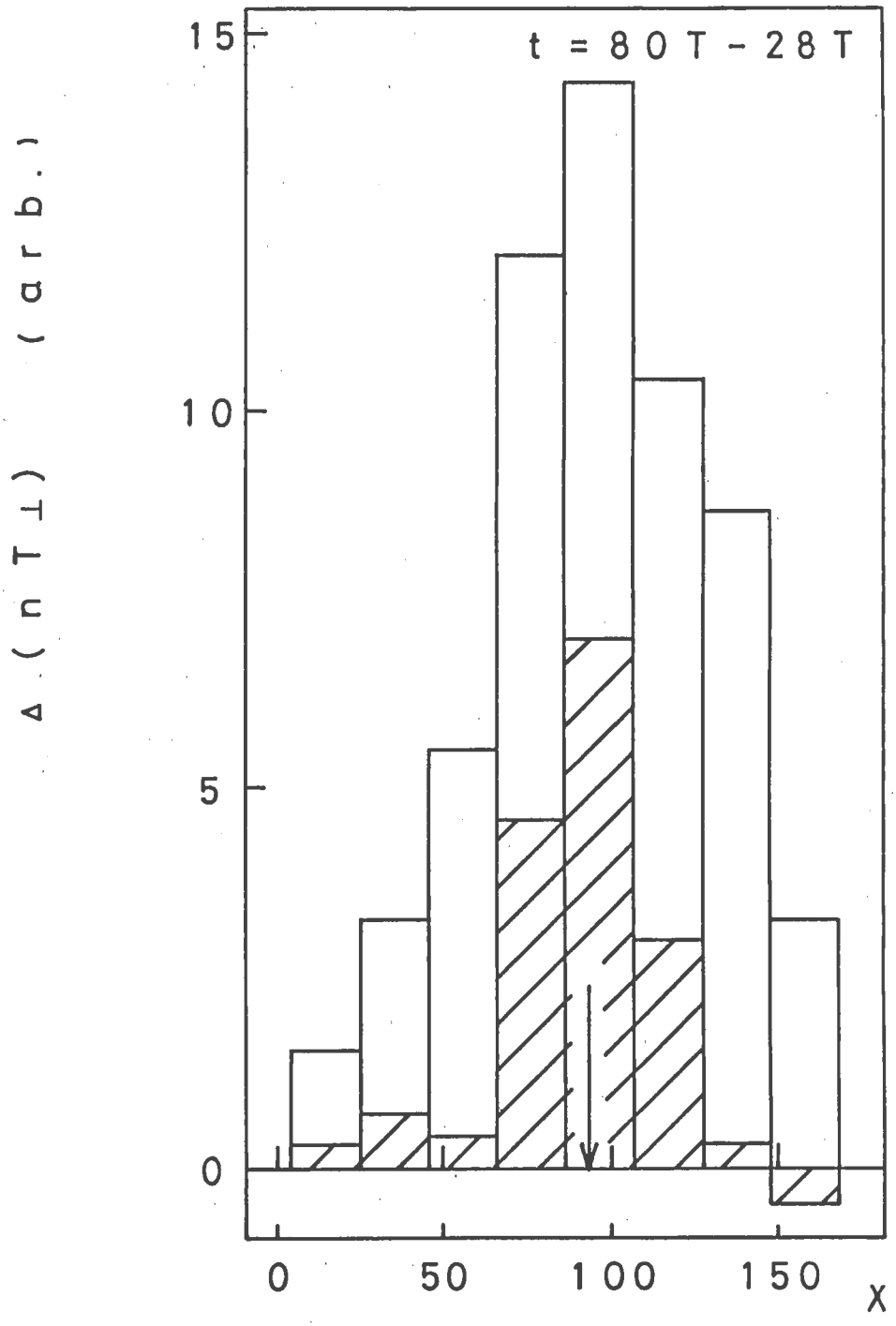

Fig. 6.4. The x dependent energy deposition into each ion in run 1; shaded parts into H and unshaded parts into D. The arrow means the position of $5\Omega_D$ resonance : $\omega - k_{//} v_{TD} - 5\Omega_D = 0$.

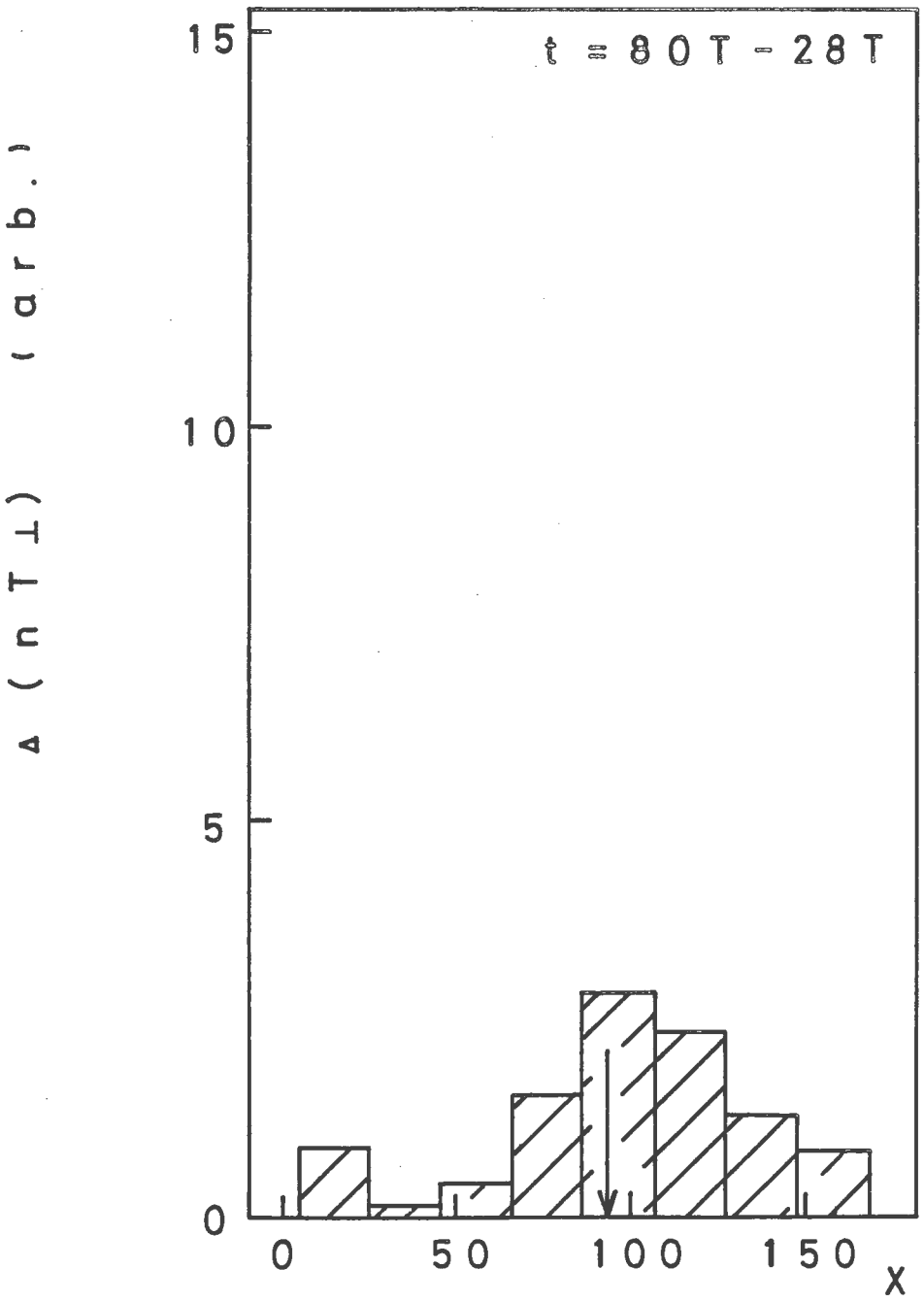

Fig. 6.5. The x dependent energy deposition into each ion in run 2 ; shaded parts into H. The arrow means the position of $5/2\Omega_H$ resonance : $\omega - k_{//} v_{TH} - 5/2\Omega_H = 0$.

wavelength parallel to the external magnetic field, which is already shown in Figs. 6.3(a). and 6.3(b). This fact means that the H ions located around the center of the system are accelerated by the wave whose frequency is nearly equal to $5/2\Omega_H$ in both runs. Therefore, we can identify the acceleration of H the $5/2\Omega_H$ subharmonic resonance acceleration.

It might be thought that H located around the position of $\omega=5/2\Omega_H$ is heated through the thermal relaxation from the directly accelerated D due to the $5\Omega_D$ resonance. Through this process, the localization of the deposited energy into H observed in run 1 can be explained. However, the thermal relaxation time from D to H is much longer than the simulated time, $80T$. Therefore, the thermal relaxation process is not dominant in this heating process of H.

Figure 6.6 shows the velocity distribution function of H in $\ln F$ vs. $v^2_\perp$ measured in the region 4-6 which is around the $5\Omega_D$ resonance region, *i. e.*, the $5/2\Omega_H$ cyclotron subharmonic resonance region. Figure 6.6(a) is the observed result in run 1, and Fig. 6.6(b) is in run 2. In both runs, the ion acceleration is almost so-called bulk heating. The increment in the ion kinetic energy in run 1 is larger than that in run 2, as is also shown in Figs. 6.4 and 6.5. This enhanced absorption at $5/2\Omega_H$ in run 1 can be attributable to the presence of the $5\Omega_D$ resonance in run 1. The $5\Omega_D$ resonance slows the wave group velocity considerably, which results in a longer time spent in the interaction region (thus more time for absorption) and in an enhanced wave electric field due to the amplitude swelling resulting in a larger non-linearity. This behavior was also pointed out by Porkolab [7].

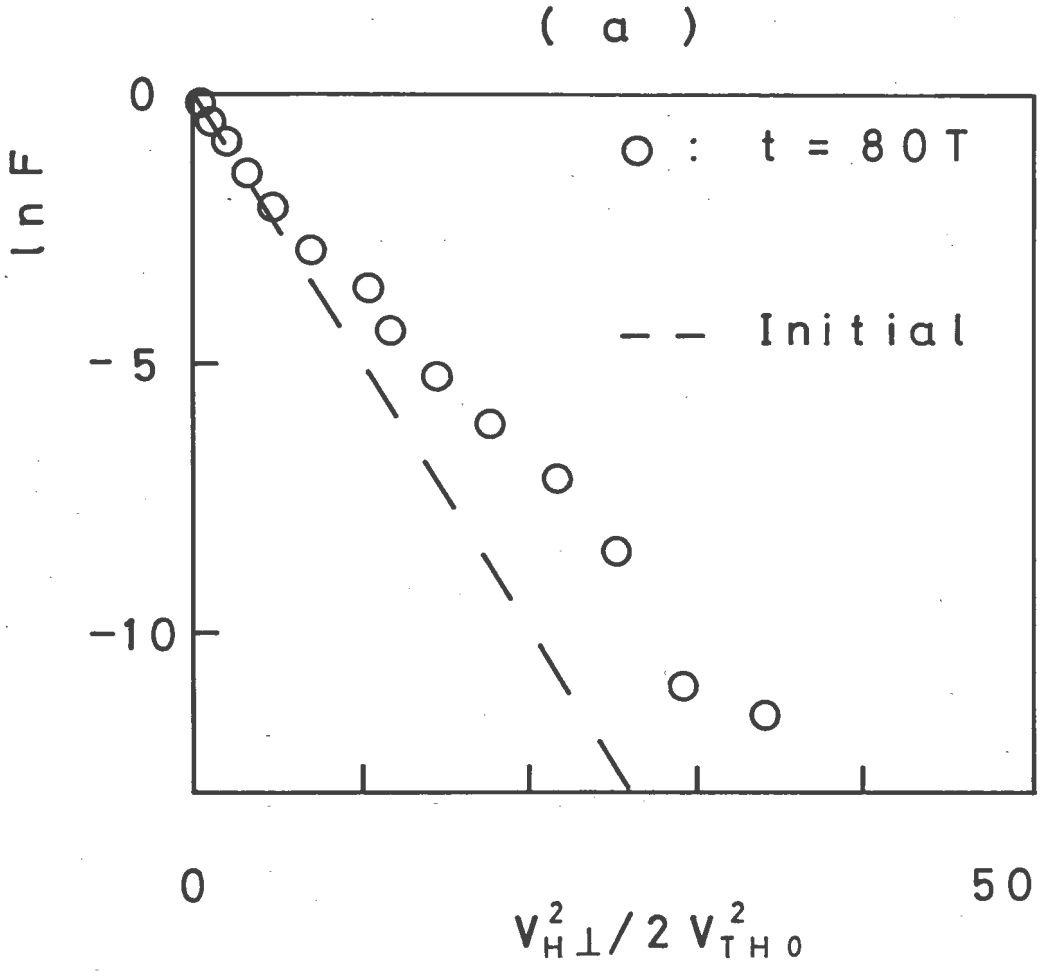

Fig.6.6. The perpendicular velocity distribution functions of H, ln F vs $v^2_\perp$. (a) in run 1, (b) in run 2.

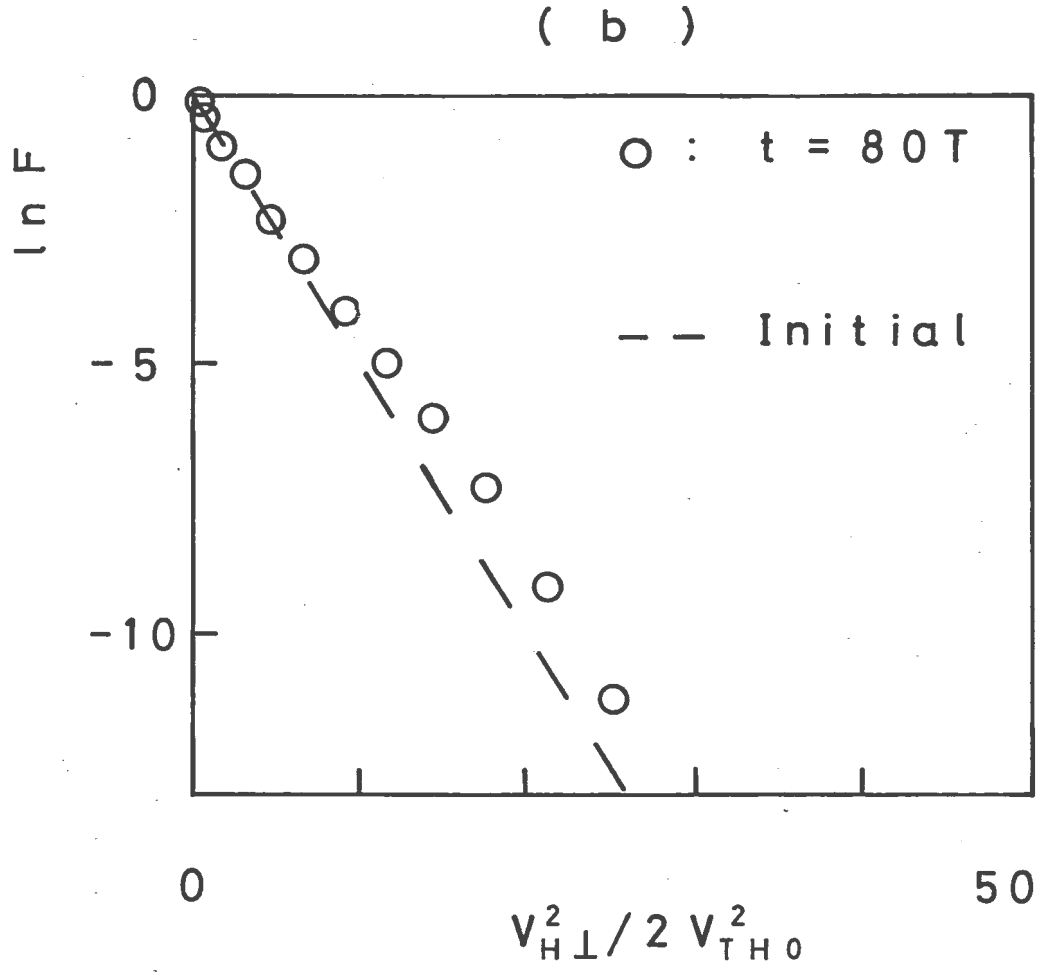
(b)
0
-5
-10
ln F
○ : t = 80T
– – Initial
0
50
$V_{H\perp}^2 / 2 V_{TH0}^2$

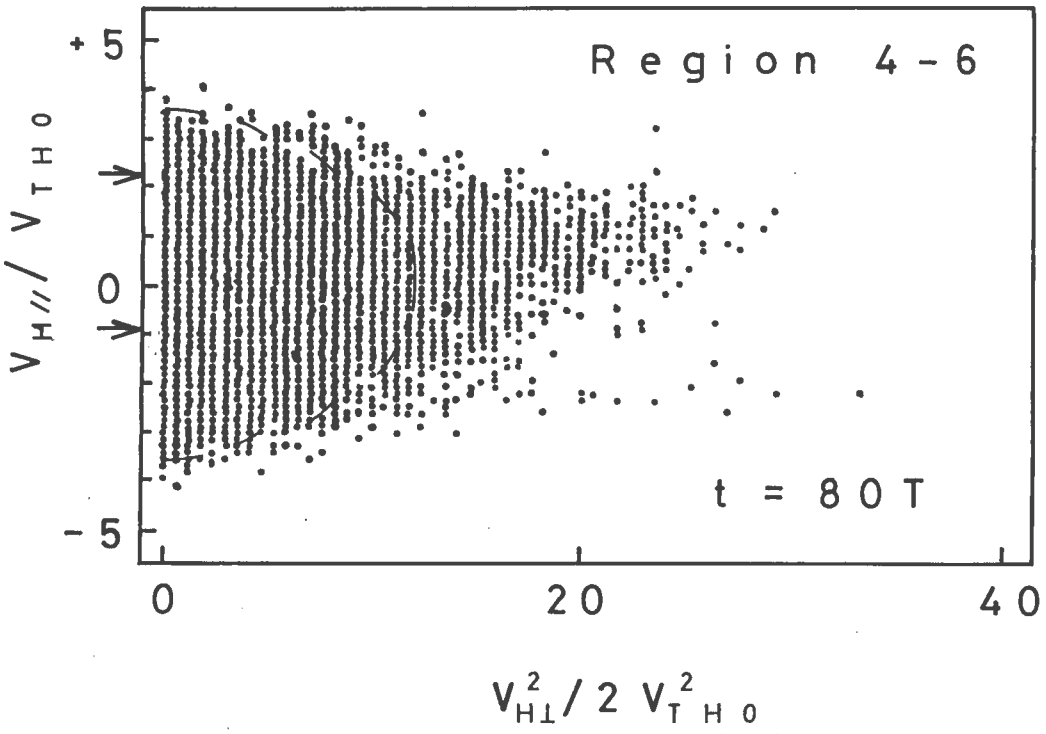

Fig. 6.7. Plots of H phase-space ($v_\perp^2$, $v_{//}$)in region 4-6 in run 1. The arrows mean the upper and lower limits of the parallel resonant velocities, $v_{//}=(\omega-5/2\Omega_H(x))/k_{//}$. The dashed lines indicate the boundaries of the initial distribution functions which are Maxwellian.

The phase-space plot of H in the space of ($v_\perp^2$, $v_{//}$) in run 1 is measured in the region 4-6 where the $5/2\Omega_H$ resonance layer is placed and shown in Fig. 6.7. The ions whose parallel velocities are in the range which is bounded with two arrows in Fig. 6.7 is observed to be accelerated selectively. This result means that the ions which satisfy the resonance condition $v_{H//}/v_{THO}=(\omega-5/2\Omega_H)/k_{//}v_{THO}=2.22\sim-0.88$ are accelerated selectively.

In Fig.6.7 some of H ions are accelerated in spite that their initial velocities are set outside of the resonance condition ($v/v_{H//} > 2.22$, $v/v_{H//} < -0.88$). In Fig.6.8, the measurement is made in region 4-6 where the resonance condition $\omega-k_{//}v_{TH}-5/2\Omega_H=0$ is satisfied. The particles observed in region 4-6 are accelerated not only in this region but also in the neighboring regions. The particles accelerated in the neighboring regions penetrate into region 4-6 because of their large Larmor radius.

Figure 6.8 shows the velocity distribution function of D in $\ln F$ vs. $v_\perp^2$ observed in the region 4-6 which is around the $5\Omega_D$ resonance region. The production of the high energy tail is observed, and the bulk of the velocity distribution is also accelerated. We assume that the high energy tail is composed of the D ions whose velocity $v_{D\perp}^2 / 2v_{TD0}^2$ is larger than 30. The number or D ion in the high energy tail is about 0.3% of the total number of D ion in region 4-6. In the bulk of the distribution, the acceleration of D is remarkable in the ions whose velocity, $v_{D\perp}^2 / 2v_{TD0}^2$, is lager than 10.

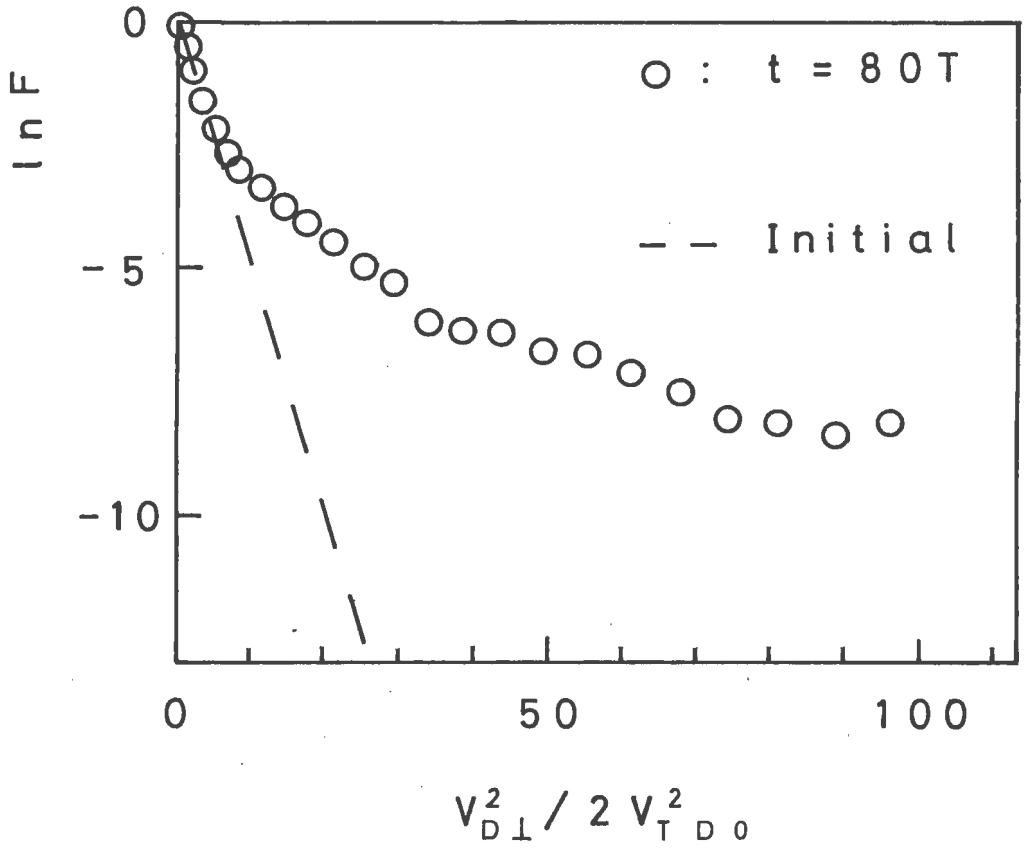

Fig.6.8. The perpendicular velocity distribution functions of D in run 1, ln F vs $v_\perp^2$.

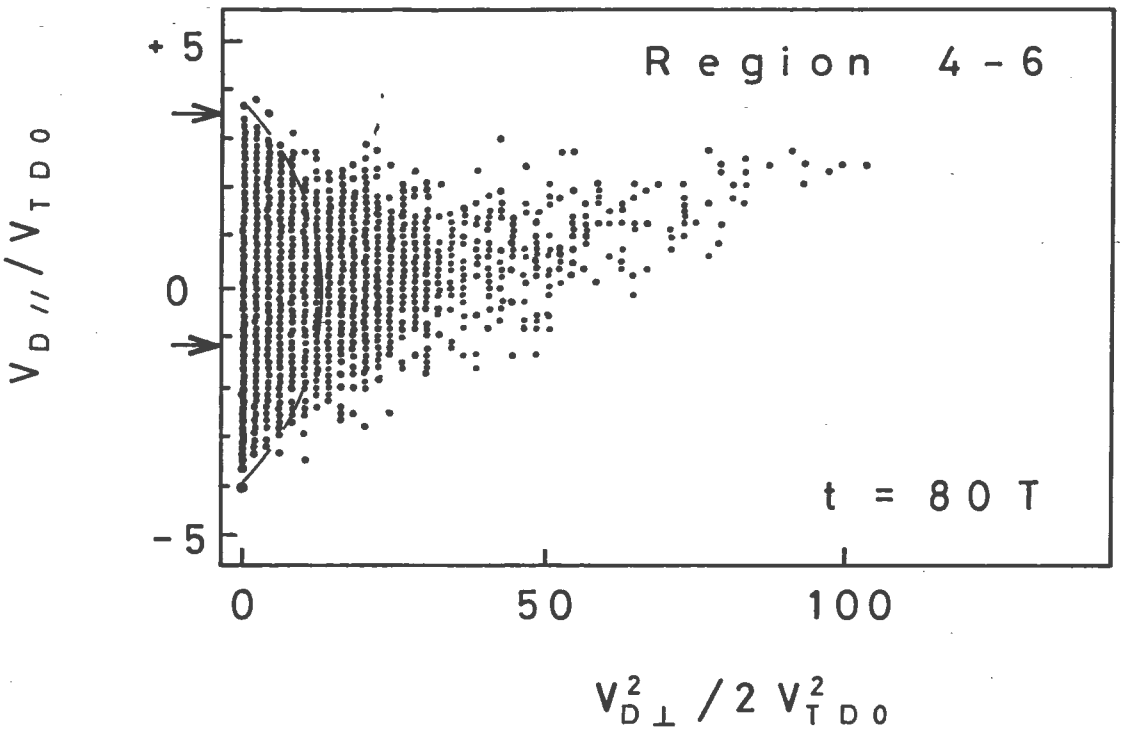

Fig.6.9. Plots of D phase-space ($v_\perp^2$, $v_{//}$) in region 4-6 in run 1. The arrows mean the upper and lower limits of the parallel resonant velocities, $v_{//}=(\omega-5\Omega_D(x))/k_{//}$. The dashed lines indicate the boundaries of the initial distribution function which are Maxwellian.

In Fig.6.9, the phase-space plot of D in the space ($v_\perp^2$, $v_{//}$) in run 1 is measured in the region 4-6 to identify the acceleration mechanism of D the $5\Omega_D$ resonance. In Fig.6.9, the range of the velocity which satisfies the resonance condition $v_{D//}/v_{TDO}=(\omega-5/2\Omega_D)/k_{//}v_{TDO}=3.55\sim-1.14$ is shown by the two arrows. The ions which satisfy this resonance condition are accelerated selectively. Therefore, the acceleration of D observed in run 1 is identified the $5\Omega_D$ resonance heating.

6.4 Discussion and conclusion

We performed several preliminary runs to investigate the $5\Omega_D$ IBW regime. We then chose two typical runs and analyzed them in detail to investigate the $5\Omega_D$ heating process due to the ion-Bernstein wave. The present paper covers the excitation, propagation, and ion heating process in the $5\Omega_D$ regime. We have already performed the computational and theoretical studies on the $3\Omega_D$ heating process [1]. Therefore,one of the purpose of this paper is to compare the results obtained in the $5\Omega_D$ hating process with those obtained in the $3\Omega_D$ heating. We will summarize the results obtained in these simulations and indicate the relation between these simulational results and results of other works concerning the physical processes of the ion-Bernstein wave heating.

With regard to the excitation, the ion-Bernstein wave is excited successfully in both runs. The ion-Bernstein wave is excited directly, which means the ion-Bernstein wave is excited not through the mode-transformation process [1]. In order to excite the ion-Bernstein wave directly, it is necessary to set

the value of ω/Ω_H near the launching region just below the cutoff of the branch [1]. In this case of the $3\Omega_H$ launching, the value of ω/Ω_H must be set just below three. Therefore,we set the value of ω/Ω_H shown in Table I, and the successful excitation of the ion-Bernstein wave is observed.

Concerning the propagation of the ion-Bernstein wave, the measured wavelengths of the excited wave agree well with those estimated from the linear theory. In the $3\Omega_D$ heating process, it is also shown that the propagation of the ion-Bernstein wave can be described with the linear theory.

As regards the ion heating, there are two processes to deposit the wave energy into ions. One is the $5\Omega_D$ resonance through which the wave energy is deposited into D, anther is $5/2\Omega_H$ subharmonic resonance through which the wave energy is deposited into H. The wave energy is deposited into both D and H, directly.

It is to be desired that the profile of the deposited energy into plasmas is well localized around the $5\Omega_D$ resonance region located in the center of the system. This desirable localization is due to the direct energy absorption into both D and H. There is a difference, however, in the total energy absorbed into the plasma between the results obtained in run 1 and 2. This result seems to indicate the dependency of the heating efficiency on the ion concentration. However, this difference is caused by the shortness of the system adopted in these runs. In order to evaluate the system length, we introduce an important quantity $\mathrm{Im}k \cdot R$($\mathrm{Im}k$ denotes the imaginary part of wavenumber k), where R is the magnetic-field-gradient, typically equal to the torus major radius [1,6]. In the ion-

Bernstein wave heating, this quantity is evaluated as$\sim R/\rho_H$, where ρ_H is the Larmor radius of H. In a typical tokamak experiment, this quantity is estimated as$\sim 10^3$ whereas in this simulation, this is$\sim 10^2$. It is still impossible to simulate the system whose size is as that in an actual experiment because of the limitation of computer time and memory size. From this estimation, it can be predicted that the power absorption is nearly complete even to a pure H plasma, and thus, that the heating efficiency could not strongly depend on the ion concentration and the energy deposition profile into plasma should be even more localized in an actual experimental system.

The particle acceleration by a wave whose frequency ω/Ω_H is nearly equal to 2.5 has been already reported [5.6]. H. Abe, *et al.* proposed a new theory of particle acceleration by a wave whose frequency was $m/2\ \Omega_H$ (m=1,3,5...) through tracing orbits of charged particles. M. Porkolab, on the other hand, proposed a new theory which could explain damping of wave whose frequency was $m/2\ \Omega_H$ (m=1,3,5...) [7]. Although the strict relationship between both approaches has not been established, we believe that both approaches are equivalent each other, and that the difference between them is the method through which the theory is introduced. It is well known that there is a deep relationship between wave-damping and particle acceleration.

It is also reported by J. Hsu that the charged particles are accelerated stochastically by a wave whose frequency is ω/Ω_H=$\sim$2.5 [10]. For this stochastic acceleration, it is required that normalized wave amplitude $\alpha=k_\perp qE/m_H\Omega_H^2$ should be above 1.75 when wave frequency is around $2.5\Omega_H$. In run 1 and 2, the values of normalized wave amplitude observed around the

$5/2\Omega_H$ resonance region are α=0.49 and α=0.42, respectively. We conclude that the ion acceleration observed around the $5/2\Omega_H$ resonance region is not due to the stochastic acceleration proposed by J. Hsu [10], and that this acceleration is due to the cyclotron subharmonic acceleration proposed by H. Abe, *et al.* [6]. In addition, it is desirable for particle confinement that $5/2\Omega_H$ subharmonic heating is so-called the bulk heating.

The process of the $5\Omega_D$ resonance acceleration was already investigated theoretically and computationally, and was reported for the lower-hybrid waves [11]. According to these results, the production of the high energy tail ions becomes prominent as the value of the frequency ω/Ω_i becomes larger. In the results of the velocity distribution function observed in run 1, the production of the high energy tail ions is observed together with the acceleration of the bulk of the velocity distribution.

Finally, we compare the results obtained in the $3\Omega_D$ heating process [1] with those in $5\Omega_D$ heating process. In both processes, the propagation of the ion-Bernstein wave can be described well with linear theory. The wave energy is deposited locally around the resonance region located in the center of the system. This desirable localization is due to the direct energy absorption into both ions D and H. In both processes, it is observed that the bulk of the velocity distribution of H is accelerated due to the cyclotron subharmonic heating. The slight difference is observed in the acceleration of D. In the $5\Omega_D$ heating process, the acceleration of D is remarkable in the ions whose velocity $v^2_{D\perp}/2v^2_{TDO}$ is larger than 10 : the bulk of the velocity distribution($v^2_{D\perp}/2v^2_{TDO} < 10$) is not heated as shown in Fig. 6.8. In the $3\Omega_D$ heating, on the other hand, the

acceleration of D is remarkable in almost the whole range of velocity.

REFERENCES

[1] H.Okada, H.Abe, R.Itatani, and M.Ono: Phys.Fluids 29,489(1986).

[2] M.Ono, K.L.Wong, and G.A.Wurden: Phys.Fluids 26, 268(1983).

[3] M.Ono, G.A.Wurden, and K.L.Wong: Phys.Rev.Lett.52, 37(1984).

[4] J. R. Wilson et al. : Proc. of Sixth Topical Conference on Radio Frequency Plasma Heating, Callaway Gardens, GA. p. 83.(1985)

[5] M. Ono U. S. Cont. to INTOR Workshop, Phase II, Part IIa, INTOR Design Group, IAEA, Vienna. (1985)

[6] H.Abe, H.Okada, R.Itatani, M.Ono, and H. Okuda: Phys. Rev. Lett. 53, 1153(1984).

[7] M.Porkolab: Phys.Rev.Lett.54, 434(1985).

[8] A. Fukuyama F. Nishiyama, K. Itoh, and S.-I. Itoh : Nucl. Fusion 23, 1005 (1983).

[9] S.Ichimaru: Basic Principles of Plasma Physics (Benjamin, New York, 1973), pp.144-145.

[10] J.Hsu: Phys.Fluids 25, 159(1982).

[11] H.Abe, H.Momota, R.Itatani, and A.Fukuyama: Phys.Fluids 23, 2417(1980).

Chapter VII

Electromagnetic Simulation on Ion-Bernstein Wave Heating

7.1 Introduction

As an advantage of the ion-Bernstein wave heating, we can utilize waveguide to launch waves into fusion plasmas, instead of antennas and coils which have complex structures, and thus, might produce impurity ions. In order to investigate the excitation process of the waveguide-launched ion-Bernstein wave, it is required to treat processes with including electromagnetic effects.

It was not easy to apply electromagnetic simulation in a two-and-one-half dimensional system to plasma heating investigations because of restriction due to ability of computer. However, the improvement in ability of computer has released simulations requiring larger memory size and longer CPU time from the limitations. Considering the ability of computer which we could utilize at the present time, we have concluded that 2.5 dimensional full electromagnetic simulation could be performed for investigations in plasma physics. Therefore, we have started to construct an electromagnetic code named PS-CODE in which full set of Maxwell equations and equation of motion are employed and treated self-consistently [1]. In addition, we have included relativistic effects in equation of motion for further applications.

In order to apply PS-CODE to the waveguide—launched ion-Bernstein wave heating, only the problem remained is to construct numerical model for waveguide system. In waveguide system, the essential point is that waves radiated from waveguide have not electrostatic components:waves satisfy the relation $\nabla \cdot \mathbf{E}=0$. Considering this point, we propose a numerical model for waveguide, which might be a most simplified one. In order to confirm the accuracy of the numerical model proposed here, we have applied the numerical model to vacuum, instead of plasmas, we think that it is easier to check the numerical model in a vacuum than in a plasma because we can adopt the theoretical prediction calculated from the dispersion relation of light in a vacuum.

In Sec. 7.2, we discuss a numerical model for waveguide system. In Sec. 7.3, we show simulation results in a vacuum, that is, without plasmas. In Sec. 7.4, we show simulation results of the ion-Bernstein wave excitation adopting the model mentioned in Sec. 7.2. In Sec. 7.5, we conclude with a discussion.

7.2 Simulation model and a numerical model for waveguide system

The simulation code PS—CODE adopted here is a 2.5—dimensional electromagnetic code which includes the relativistic effects. In this code, full set of Maxwell equations

$$\nabla \cdot \mathbf{E} = \frac{\rho}{\varepsilon_0}, \tag{7.1}$$

$$\nabla \cdot \mathbf{B} = 0, \tag{7.2}$$

$$\nabla \times \mathbf{E} = -\frac{\partial \mathbf{B}}{\partial t}, \tag{7.3}$$

$$\nabla \times \mathbf{B} = \mu_0 \mathbf{J} + \frac{1}{c}\frac{\partial \mathbf{E}}{\partial t}, \tag{7.4}$$

and equation of motion for charged particle

$$\frac{d\mathbf{P}}{dt} = q\mathbf{E} + q\mathbf{v} \times \mathbf{B}, \tag{7.5}$$

are solved self-consistently. In Eq. (7.5), P denotes relativistic momentum of charged particle. The numerical methods adopted in PS-CODE will be discussed in detail and published elsewhere [1,2,3].

In this section, we will explain numerical model of waveguide constructed in PS-CODE. In the electrostatic code, electrostatic exciter was given by [4].

$$\rho_{ext}(x,z,t) = \rho_o \delta(x - x_s) sin(k_{//}\, z - \omega t), \tag{7.6}$$

where x_s, k, and ω denote the position of exciter, wavenumber, and frequency of exciter. ρ_o is constant. X and z directions correspond to those which are perpendicular and parallel to the immersed magnetic field. In imitation of electrostatic excitation given by Eq. (7.6), we define electromagnetic wave source as

$$\mathbf{J}_{ext}(x,z,t)=j_0\delta(x-x_s)\sin(k_{//}z-\omega t)\mathbf{j}, \tag{7.7}$$

where $\mathbf{j}$ is a unit vector to the z direction, and other notations are the same as in Eq. (7.6).

However, the electric field produced by the external current given in Eq. (7.7) involves the electrostatic component, *i.e.*, $\nabla\cdot E\neq 0$. It is an essential point that waves radiated from waveguides into plasmas have not electrostatic components. We, therefore, eliminate electrostatic components from Eq. (7.7), and only the rest components are added as J_{ext} term in Eq. (7.4). The method to produce electromagnetic components from Eq. (7.6) is as follows.

We calculate divergence of J_{ext}, and solve Poisson's equation under given boundary conditions:

$$\nabla^2\Psi_q = -\nabla\cdot\mathbf{J}_{ext}. \tag{7.8}$$

We obtain $\mathrm{J^L}$ using the obtained Ψ_q in Eq. (7.8) as

$$\mathbf{J}^L_{ext} = -\nabla\Psi_q \tag{7.9}$$

Removing electrostatic component $\mathbf{J}^L_{ext}$ from $\mathbf{J}_{ext}$, we obtain $\mathbf{J}^T$ which is an electromagnetic component:

$$\mathbf{J}^T_{ext} = \mathbf{J}_{ext} - \mathbf{J}^L_{ext}. \tag{7.10}$$

J^T_{ext} is expressed as follows.

(i) For $0\leqq x<x_s$,

$$J^T_{ext,x} = \frac{P}{\sinh k_{//}\, x_s} \cosh k_{//} x \cos(k_{//} z - \omega t), \tag{7.11}$$

$$J^T_{ext,z} = -\frac{P}{\sinh k_{//}\, x_s} \sinh k_{//}\, x \sin(k_{//}\, z - \omega t). \tag{7.12}$$

(ii) For $x_s \leqq x < L_x$,

$$J^T_{ext,x} = \frac{P}{\sinh k_{//}\,(L_x - x_s)} \cosh k_{//}\,(L_x - x) \cos(k_{//} z - \omega t), \tag{7.13}$$

$$J^T_{ext,z} = -\frac{Pk_{//}}{\sinh k_{//}\,(L_x - x_s)} \sinh k_{//}\,(L_x - x) \sin(k_{//} z - \omega t), \tag{7.14}$$

where P is constant, L_x denotes system length in the x direction, and X_s denotes the position of exciter, respectively. The external current given by Eq. (7.11)-(7.14) is added to the right-hand side of the Maxwell equation :

$$\nabla \times \mathbf{B} = \mu_0 \mathbf{J}_{ext} + \mu_0 \mathbf{J}_{int} + \frac{1}{c}\frac{\partial \mathbf{E}}{\partial t}, \tag{7.15}$$

where $\mathbf{J}_{int}$ denotes current composed of plasma particles.

7.3 Electromagnetic fields radiated from waveguide to a vacuum

As a check of numerical model for waveguide given in Eq. (7.11)—(7.14), we perform a simulation for propagation of light in a vacuum. We observe wavelength in a vacuum, and we can obtain a dispersion relation in the simulation. Then we compare the dispersion relation observed in the simulation with

that of light in a vacuum, *i.e.*, $\omega=ck$, where c is the light velocity. Simulation parameters are shown in Table VII-I. In this run, electromagnetic wave is radiated in a two-dimensional system.

Table VII-I Simulation parameters

System length in the x direction	128
System length in the z direction	512
Light velocity	1.0
Source frequency	0.632
Wavenumber in the z direction	0.01223
Position of source	1.0

Figure 7.1 shows the contour of interferograms between the observed electric field and the source signal. Source current given Eqs. (7.11)–(7.14) is placed just inside the conducting wall in the left-hand side parallel to the z direction. Figure 7.1 (a) and (b) correspond to E_x and E_z, respectively. The measured wavenumbers of electric field perpendicular to the z direction is $k_\perp=9.9$, which agrees well with the calculated value from the dispersion relation of light. Considering the light velocity and the simulated time, we can expect that the wave front reaches at the position $x=79.2$ from the calculation. This expection agrees quite well with the observed results shown in Figs. 7.1 (a) and (b).

7.4 Excitation and propagation of the ion-Bernstein wave

We apply the waveguide given in Eqs. (7.11)−(7.14) to plasmas as an exciter of the ion−Bernstein wave. Two runs called run 1 and 2 are performed. Simulation parameters are shown in Table 7.2. Electromagnetic wave is radiated by a waveguide antenna given in Eqs. (7.11)−(7.14), placed parallel to the Zn direction just beside the left−band side. The frequency of wave source changes as $1.84 \leqq \omega/\Omega_i \leqq 0.99$, which configuration corresponds to the lower−field side excitation in an experiment. The configuration of the magnetic field adopted in run 1 and 2 corresponds to that in the $3\Omega_D$ heating which has been discussed in Chapter V. We have used many particles enough to avoid wave−damping due to particle Coulomb collision [5]. The thermal velocities of both electron and ion are much slower than the light velocity. The essential difference between run 1 and 2 is β-value which is defined by pressure-ratio between plasma and external magnetic field. In run 1, this value is roughly 0.2%; on the other hand, this value is nearly 1% in run 2.

Figure 7.2 shows the contour of interferograms between the observed electric field and the source signal in both run 1 and 2. We show only the observed results of electrostatic potential, because the magnitudes of electromagnetic components are much less than those of electrostatic components. These results show that electrostatic approximation is adequately valid for ion−Bernstein wave. In both runs, the successful excitation of wave is observed. We can see a slight defference between the values of wavenumber observed in run 1 and 2. This

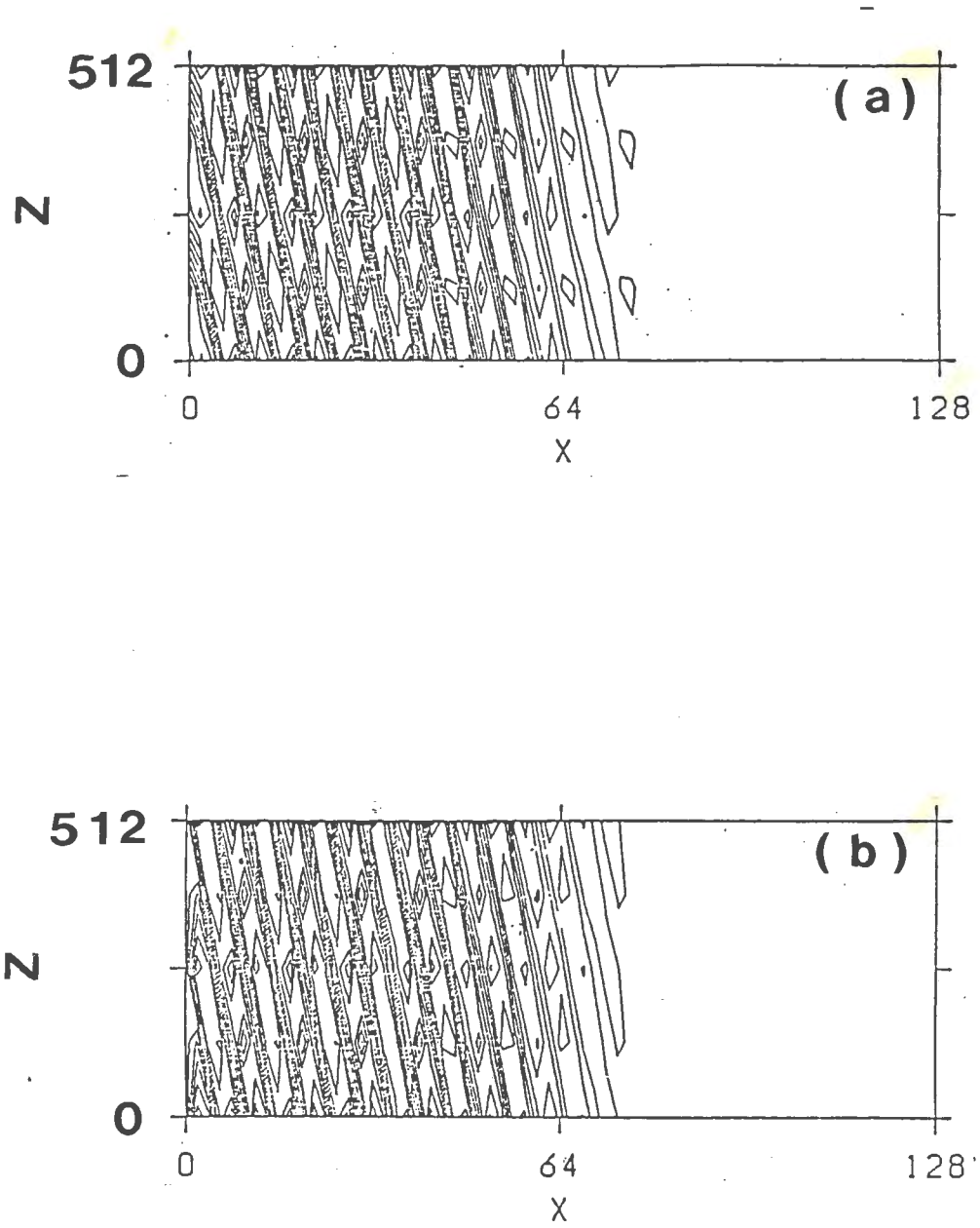

Fig.7.1. Contour of interferograms between the electric field observed and the source signal. The horizontal and vertical lines correspond to the x and z direction, respectively. Distance in the z direction is scaled down by 1/64 compared with that of the x direction. (a)Contour of electric field in the x direction. (b)Contour of electric field in the z direction.

difference is caused by the difference of plasma density as shown in Table VII-II.

In both runs, the values observed agree well with those calculated from linear theory.

Table VII-II Simulation parameters

	run 1	run 2
$(\omega/\Omega_i)_{max.}$	1.84	1.84
$(\omega/\Omega_i)_{min.}$	0.99	0.99
v_{Te}/light-velocity	3.3×10^{-2}	3.3×10^{-2}
T_i	$4T_e$	$4T_e$
v_{ph}/v_{Te}	8.07	8.07
$(k_\perp\rho_i)_{max.}$	2.1	2.1
$(k_\perp\rho_i)_{min.}$	0.8	0.8
$(\omega_{pe}/\Omega_{e,\ max})^2$ min.	0.05	0.25
$(\omega_{pe}/\Omega_{e,\ max})^2$ max.	0.1	0.5
β-valve max.	0.2%	1%

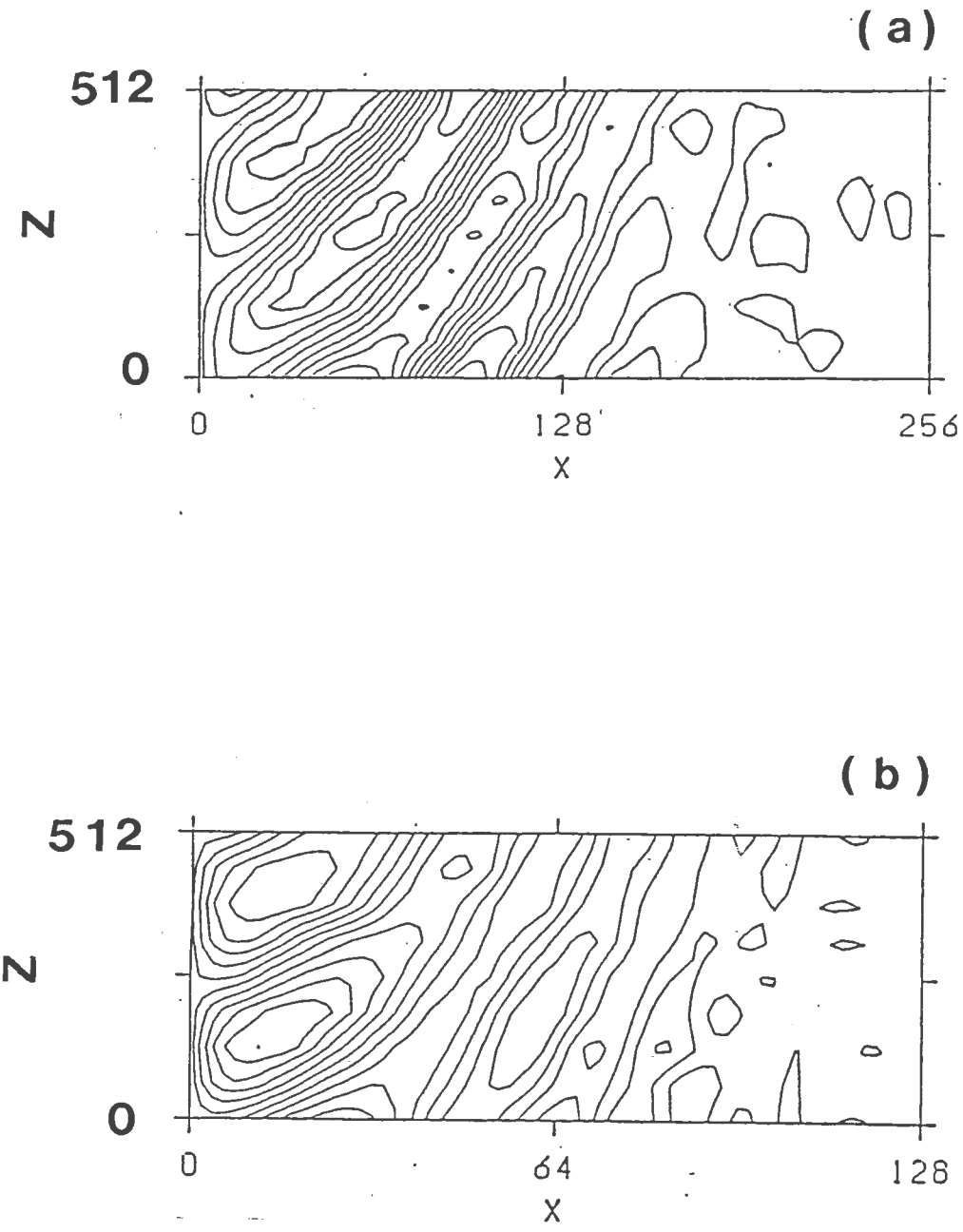

Fig.7.2. Contour of interferograms between the electric field observed and the source signal. The horizontal and vertical, lines correspond to the x and z direction, respectively. Distance in the z direction is scaled down by 1/32 compared with that of the x direction. (a) in run 1 : low β run. (b) in run 2 : high β run.

7.5 Conclusion

In this chapter, we have investigated the excitation and propagation of the waveguide-launched ion-Bernstein wave in a single-component-ion plasma, utilizing electromagnetic particle simulation code PS-CODE. The numerical properties of PS-CODE will be discussed in detail in Ref. 2 and Ref. 3. Here, we will summarize the results obtained briefly.

We have constructed the numerical model for waveguide, which might be a most simplified one. In this numerical model, waves radiated from waveguide satisfy the relation $\nabla \cdot \mathbf{E} = 0$. Adopting this model, we have intended to investigate the excitation and propagation of waveguide-launched ion-Bernstein wave.

The simulation results show the successful excitation and propagation of the waveguide-launched ion-Bernstein wave. Comparing the results obtained in the simulation with those calculated from linear dispersion relation, we show that the propagation process of ion-Bernstein wave can be described well with linear theory. Considering the simulation results presented in this chapter, we find no serious difficulties for eventual implification of waveguide-launched ion-Bernstein wave heating.

REFERENCES

[1] H. Abe, N. Sakairi, S. Nakajima, and R. Itatani : Kakuyugo Kenkyu 53,461 (1985) (in Japanese).

[2] H. Abe, and S. Nakajima: to be published in Phys. Lett. A.

[3] H. Abe, S. Nakajima: J. Phys. Soc. Jpn. 56,(1987).

[4] H. Abe, R. Itatani, and H.. Momota : Phys. Fluids 22, 1533 (1979).

[5] H. Okada, H. Abe, R. Itatani, and M Ono : Phys. Fluids 29,489 (1986).

Chapter VIII

Conclusion

In this paper, we investigated the ion-Bernstein wave heating process in (D-H) plasmas by means of particle simulation. In this chapter, we will review the results obtained here.

In Chapter II, in order to use for analysis of wave excitation and propagation in the following chapters, we introduced the dispersion relation for ion-Bernstein wave, then reviewed the theory of excitation, propagation of the ion-Bernstein wave through mode-transformation.

In chapter III, we introduced the cyclotron subharmonic acceleration through three different methods, *i.e.*, self-consistent simulation, single-particle simulation, and multiple-time-expansion which is an analytical method. According to the results obtained from the above-mentioned methods, we conclude that charged particles are accelerated due to waves whose frequencies are set around $\omega = m/2\,\Omega_H$ (m = 1,3,5...). Through both self-consistent and single-particle simulation, self-consistency does not play an important role in the acceleration process. The analytical method shows that finite-Larmor-radius effects play a dominant role in the process. Cyclotron subharmonic acceleration is an important mechanism to deposit wave energy into ions in ion-Bernstein wave heating, which is discussed in detail in Chapter V and VI.

In chapter IV, we investigated excitation and propagation of the ion-Bernstein wave through mode-transformation process in a single-component-ion plasma. We find that propagation process of the ion-Bernstein wave is described well with linear theory. For the direct excitation of the ion-Bernstein wave, it is required to set the value of ω/Ω_i around antenna position close to the cutoff of the branch.

Both in Chapter V and VI, we showed simulation results for $3\Omega_D$ and $5\Omega_D$ heating in (D-H) plasmas due to the ion-Bernstein wave, respectively. In both processes, we obtained almost the same results. Wave propagations agree well with linear theory. Energy deposition profiles localize around resonance regions placed in the center of the system. Wave energies are absorbed directly into D and H ions through cyclotron-harmonic and cyclotron subharmonic acceleration which is discussed in Chapter III. With regard to energy deposition into H ions, wave energies are absorbed into bulk parts of the velocity distribution functions in both processes. Concerning D ion, tail parts of the distribution are accelerated more strongly in $3\Omega_D$ heating than in $5\Omega_D$ heating.

In Chapter VII, we confirmed the excitation and propagation of the waveguide-launched ion-Bernstein wave through electromagnetic particle simulation. We constructed a numerical model for a waveguide, which radiated only electromagnetic components. Then we performed simulations of the ion-Bernstein wave excitation and propagation. Adopting the particle simulation code constructed here, we confirmed that waveguide-launched ion-Bernstein wave was excited successfully. The propagation process of the ion-Bernstein wave is described well with linear theory,

as well as confirmed in Chapter IV where electrostatic approximation is adopted.

From a point of view of an additional heating method for fusion plasmas, we pointed out the following properties of the ion-Bernstein wave heating:one point is that the ion-Bernstein wave is excited successfully utilizing waveguides, the another point is that bulk parts of the ion velocity distribution function are accelerated due to the ion-Bernstein wave. According to the results obtained in this paper, we conclude that ion-Bernstein wave heating is a promising method as additional heating for fusion plasmas.

Acknowledgements

It is a great pleasure to acknowledge Professor Ryohei Itatani and Dr. Hirotada Abe for their continuous guidance and discussions from the beginning of my research on plasma physics at Department of Electronics, Kyoto University.

I wish to express my most sincere thanks to Dr. Masayuki Ono at Princeton Plasma Physics Laboratory, Princeton University for his stimulating discussions and kind encouragements. I also wish to thank Dr. Hideo Okuda at Princeton Plasma Physics Laboratory, Princeton University for his discussions on particle simulations.

I wish to express sincere thanks to Dr. Ryo Sugihara and Dr.Yuichi Ogawa at Institute of Plasma Physics, Nagoya University for their kind discussions on theoretical analysis of cyclotron subharmonic heating.

I wish to express my sincere thanks to Dr. Hirotada Abe for his permission to use electromagnetic code which has been constructed under his initiative. I also wish to express my sincere thanks to Mr. Sadanojo Nakajima and Mr. Yutaka Kadoya for their cooperations and discussions.

I wish to thank Dr. Hiroshi Matsumoto at the Japan Atomic Energy Research Institute for useful discussions and comments on cyclotron subharmonic heating. I also should like especially to thank Mr. Koichi Kotani, Dr. Koichi Maki, Mr. Kimio Yamada, Dr. Kazuki Tsuchida, Mr. Satoshi Ogura, Mr. Masahiro Toma, Dr. Kazumichi Suzuki, and Dr. Norihiko Ozaki of Energy Research Laboratory, Hitachi Ltd., for their encouragements.

Numerical simulations and calculations have been curried out at Computer Center of Institute of Plasma Physics, Nagoya University and Data Processing Center, Kyoto University.

This work was initiated during Dr. Hirotada Abe's stay in the USA in 1981 under the US-Japan personal exchange program in the field of controlled thermonuclear fusion study. This work was carried out under the Collaborating Research Program at the Institute of Plasma Physics, Nagoya University. This work was partially supported by an MOE grant in aid.